IMPRIMATUR POUR LA THÈSE

Dynamic properties of vortex phases in the mixed state of $YBa_2Cu_3O_7$ superconducting thin films

de M. Michel Calame

UNIVERSITÉ DE NEUCHÂTEL

FACULTÉ DES SCIENCES

La Faculté des sciences de l'Université de
Neuchâtel sur le rapport des membres du jury,

MM. P. Martinoli (directeur de thèse), H. Beck,
J.-M. Triscone (Uni. Genève) et W. Benoit (EPF Lausanne)

autorise l'impression de la présente thèse.

Neuchâtel, le 15 décembre 1998

Le doyen:

F. Stoeckli

A Jeanne-Marie,
à mes parents.

Contents

1 Survey

More than ten years after the unprecedented research effort stimulated by the discovery of high-temperature superconductivity in the $La_{2-x}Ba_xCuO$ compound by Bednorz and Müller [1] in 1986, the interest for this field remains very intense due to the fascinating physical properties exhibited by the high-temperature superconductors (HTS). One of the most remarkable and intriguing aspects of these superconductors, besides their high transition temperature, is perhaps what de Gennes called '... *the beautiful saga of the vortices* ...', a saga raised by the incredible richness of vortex behavior in the mixed state of HTS [2].

Cuprate superconductors

The new class of superconductors, initiated by Bednorz and Müller, is designated as *high-temperature superconductors* which, up to now, amounts to *cuprate* superconductors since all these compounds embody over-, under- or optimally doped CuO_2 planes [3]. Their physical properties differ from the 'conventional' low-temperature superconductors in a number of properties, the most relevant of them being their high transition temperature T_c, short coherence length ξ, large penetration depth λ and layered crystalline structure. We shall discuss the structure and physical properties of these cuprates in Chapter 3 where we will in particular focus on the $Y_1Ba_2Cu_3O_7$ (YBCO) compound. It is however important to point out that these cuprates form a new kind of metal as a consequence of their layered structure. This peculiarity results in a confinement of the electrons to the conducting copper-oxide planes so that these materials exhibit a poor conductivity along the third dimension perpendicular to the layers. The properties of HTS seem to originate from a new type of correlated motion of the electrons whose microscopic origin is still under debate (see e.g. Ref. 3–5). In the quest for an answer to this problem, an important point is the established consensus about the asymmetric nature of the order parameter in these compounds [6].

Vortex matter

High-temperature superconductors exclude an externally applied magnetic field up to a first critical field B_{c1}, above which the magnetic field is able to penetrate in the form of an array of flux lines or vortices, each carrying one flux quantum $\phi_0 = h/2e$. The non-superconducting zone bearing the flux quantum constitutes the core of the vortex and is surrounded, in the plane perpendicular to the field, by circulating supercurrents extending radially over a distance λ, called the magnetic penetration depth. As the externally applied magnetic field reaches the upper critical field B_{c2}, the lattice spacing between the vortices in the superconductor is small enough so that the vortex cores do overlap and superconductivity gives way to a normal metallic behavior. The superconductor is said to be in the mixed state when the externally applied magnetic field lies between B_{c1} and B_{c2}. It turns out that the magnetic field and temperature range over which the superconductor is in the mixed state covers a large part of the $B-T$ phase diagram, thereby encouraging researchers to investigate and understand the behavior of the vortices in the HTS.

One particular feature of vortices in superconductors is that a current flowing through the superconductor gives rise to a Lorentz force on each vortex and tends to bring them into motion. The key point here is that a moving vortex produces dissipation, thus weakening the superconductivity in the material. Wheter the vortices will move or not depends on the situation encountered in the superconductor. The physics of vortices is in fact rather complex and is governed by the competition between different energies:

- The *repulsive interaction* between vortices favors an arrangement of the vortices into a perfect vortex lattice: the vortex crystal;

- The combination of a high transition temperature, strong anisotropy and short coherence length contribute to increase the effect of *thermal fluctuations* in the HTS. In particular, thermal energy will favor a vortex liquid by causing the flux lines to fluctuate and wander around their equilibrium positions;

- Superconducting thin films or crystals are not perfect and contain, to different extents, structural imperfections which lead to *pinning* of the flux lines. Pinning is expected to bring disorder in the arrangement of the flux lines, thus favoring a disordered solid of vortices;

- The layered crystalline structure of cuprates is the cause for the anisotropic behavior of these compounds. In particular, a flux line in such a superconductor can be pictured as a stack of pancake vortices, each pancake laying in a superconducting plane. The *coupling energy* between the pancakes, monitored by the anisotropy and the vortex density, will thus determine the discrete or continuous nature of the flux lines in the superconductor.

These four ingredients, temperature, vortex interaction, pinning and coupling between layers, are responsible for the appearance of a remarkable variety of vortex behaviors, the existence of liquid and solid vortex phases representing one of the most interesting aspects of the problem.

At low temperatures, a well-ordered phase does build-up in clean superconductors: the vortex lattice. As temperature increases, the vortex lattice melts into a vortex liquid via a first order phase transition [7]. This was confirmed experimentally by the observation of a jump in the internal energy of the vortex system deduced from magnetization and calorimetric measurements [8, 9].

Superconducting samples, and in particular thin films, exhibit crystallographic defects meaning that disorder in the vortex arrangement will have to be taken into account. The presence of disorder in the vortex medium leads to reconsidering the existence of a true superconducting phase at low temperatures. However, in contrast to the Kim-Anderson flux-creep model [10], where the vortices are thermally activated over the pinning barriers as soon as the temperature T or the current density j are non-zero, Fisher *et al.* [11] suggest the existence, in a disordered vortex medium, of a true superconducting phase at low temperatures, the vortex-glass phase, separated from a high temperature vortex-liquid phase by a continuous phase transition at a temperature $T = T_g$. The dimensionality of the vortex medium is expected to play a major role since in a 2D vortex system, the model predicts $T_g = 0$ whereas $T_g > 0$ for a 3D vortex medium.

Motivations and outline

The study of vortex matter thus appears as very attractive and promising due to the wide range of physical phenomena likely to be observed. The superconducting properties of HTS are strongly influenced, presumably dominated, by the behavior of the vortices over a wide region of the phase diagram. This strongly contributes to the interest in the study of vortex motion in HTS, in particular because of the major importance of a proper understanding of the dissipation processes in type II superconductors, due to the large potential for technical application of these materials. Moreover, the vortices in superconductors turn out to be a highly accessible model system for the behavior of one-dimensional interacting objects subject to disorder. The prevalent use of the words 'vortex matter' emphasizes that the behavior of vortices is comparable in complexity to conventional atomic matter.

This document is organized as follows. We start in *Chapter 2* with the description of some phenomenological and theoretical aspects of superconductivity . After a brief introduction on the phenomenon of superconductivity, we focus on the flux line lattice in type II superconductors and describe the effects of the temperature and disorder on its properties. The production and characterization of the samples is described in *Chapter 3*, where we first review the basic crystallographic properties of the $Y_1Ba_2Cu_3O_{7-\delta}$ compound. A brief description of the Pulsed Laser Ablation method, used to grow our films, is then given, followed by a discussion of the properties of the layers as determined by X-ray diffraction (XRD) and Atomic Force Microscopy (AFM) analysis. *Chapter 4* is devoted to the description of the measuring technique and the cryostat. Our main interest in this work was to study the properties of the vortex system by means of an *ac* inductive measuring technique which allows to measure the linear response of the vortex system, i.e. the response in the limit of low driving currents. In order to probe the existence of possible phase transitions in the vortex medium, measurements should be carried out for large time and length scales and weak perturbations of the vortex system. This inductive technique appears to be an interesting tool, since it allows contactless measurements of the linear response of the vortex medium at not too-high frequencies. The results are presented in *Chapter 5* where we start with an overview of the behavior of the data and summarize the main features observed. Chapter 5 continues with a section where the problem of the magnetic penetration depth is treated. We then present the analysis of the data in the high temperature regime where we discuss the problem of the thermally activated vortex motion. In the next section, we present a scaling analysis of the data in the search for some evidence of the existence of a true phase transition between a vortex-glass phase and a vortex-liquid phase in our films. We then introduce the concept of 'frozen' vortex liquid to explain our observations in terms of a dynamic crossover rather than a phase transition. Finally, we end this chapter by giving a phenomenological description of the behavior of our data based on the assumption that the vortices can be regarded as a viscoelastic medium. In *Chapter 6*, we summarize and comment our main results and present the general conclusions of this work.

2 Theoretical and phenomenological aspects

This chapter summarizes a few theoretical aspects of the superconductivity phenomenon. After a short historical introduction, the Ginzburg-Landau theory is briefly discussed. The next and main part of the chapter reviews the basic properties of the mixed state in type II superconductors. First the elastic properties of the perfect flux-line lattice and the effect of thermal fluctuations are discussed. The influence of material imperfections resulting in pinning of the flux lines is then presented with an emphasis on the properties of thin films. The importance of thermal fluctuations as well as pinning, disorder and anisotropy lead to a rich variety of vortex phases in high temperature superconductors (HTS) which will lead to sketch out phase diagrams in some particular cases. A final section deals with the dynamic response of the vortex lattice.

2.1 Superconductivity

A first successful description of the superconducting transition was given by Gorter and Casimir in the early 1930's [12]. Their two-fluid model assumed the existence of two types of electrons in the superconductors, the normal electrons behaving approximately like electrons in normal metals and the superelectrons exhibiting special properties, in particular the possibility to carry current without resistance. The fluid of superelectrons (superfluid) is perfectly ordered, has no entropy and can carry no heat. Below the superconducting transition temperature T_c, the superfluid density increases while the normal electron density falls down. Since both the normal and superfluid electrons conduct in parallel, the dc electrical conductivity becomes infinite and the heat conductivity falls to zero at T=0.

During the same period, F. and H. London were the first to write down the two electrodynamic equations describing the fundamental properties of superconductors: perfect conductivity and perfect diamagnetism [13]. An electrical field $\vec{E}$ in the superconductor will cause an acceleration of the superelectrons, as expressed by the first London equation

$$\frac{\partial \vec{j}}{\partial t} = \frac{n_e e^2}{m_e} \vec{E} \tag{2.1}$$

where n_e is the density of electrons, m_e the mass of an electron and $\vec{j}$ the current density. This means that after a short pulse of electric field the system will be left with a supercurrent which will not decay thus allowing perfect conductivity. The second equation shows that a superconductor placed in a magnetic field will screen this magnetic field over a very short distance called the London penetration depth $\lambda_L(T) = (m_e/\mu_0 n_e e^2)^{1/2}$. The equation reads

$$\nabla^2 \vec{B} = \frac{1}{\lambda_L^2}\vec{B} \tag{2.2}$$

In fact the superconductor does not only screen an applied magnetic field but it will expel it if the field is applied above the superconducting transition and then the system cooled down. Meissner and Ochsenfeld were the first to observe this property of perfect diamagnetism in 1933 [14].

The picture developed with the two-fluid model found a microscopic justification when Bardeen, Cooper and Schrieffer developed their BCS theory in 1957 [15]. The theory is based on the idea that, in superconducting metals, a weak attractive force arises between electrons near the Fermi level. The consequence of this attractive force is that the Fermi sea is no longer stable and, below T_c, the fundamental state is a new macroscopic quantum state where part of the electrons near the Fermi energy appear bound in pairs (Cooper pairs). The internal motion of one pair is supposed to have no angular momentum which forces the spins of the electrons to be antiparallel. As an ordinary metal can have electron and hole excitations with a definite momentum $\hbar\vec{k}$, the paired state, like the usual Fermi sea, can have single-particle excitations which are electron-like above the Fermi level or hole-like below it. These single-particle excitations (or quasiparticles) are still fermions but differ from normal electrons or holes. The main difference is the occurence of an energy threshold below which the particle excitations can not be created. If the binding energy of a condensate pair is 2Δ, we will need an equivalent energy to break up a pair. The minimum excitation energy required to create a single-particle excitation is thus Δ. This energy is called the energy gap and is expressed by $\Delta(T)/\Delta(0) \simeq 1.74(1-(T/T_c)^2)^{1/2}$ near T_c with $\Delta(0) = 1.76 k_B T_c$ [7].

We saw that the pairs are all in the same orbital state. Moreover, each pair has the same center of mass motion. This center of mass motion can be described by a center of mass wavefunction $\Psi(\vec{r})$, the superfluid wavefunction, which is the same for each pair. The normalization of this wavefunction is to make $\Psi^*\Psi$ equal to the density of pairs n_s. This interpretation allows to write down the current density[1] in the usual quantum-mechanical form $\vec{j_s} = \frac{ie\hbar}{2m_e}(\Psi^*\nabla\Psi - \Psi\nabla\Psi^*)$, in the absence of magnetic field (see for instance Ref. [5]).

2.1.1 Ginzburg-Landau theory

Before the BCS theory was elaborated, V. L. Ginzburg and L. D. Landau proposed a theory of the superconducting transition [16] based on an earlier theory of Landau (see e.g. [17]) which allows a description of phase transitions in general. This Ginzburg-Landau (GL) theory is phenomenological in the sense that it accounts for some general features

---

[1] The current density is the product of the charge transported by one carrier times the volume density of carriers times the velocity of the charge carriers.

observed in superconductors without invoking a microscopic description. Therefore it remains very general and can be applied to the cuprate superconductors[2] where the question of the microscopic theory remains open.

Phase transition

Landau noticed that many phase transitions involve an ordering process (one of the states is 'more symmetric' than the other) and that an order parameter can be defined, like the magnetization in ferromagnetic systems. It can be shown by thermodynamical arguments [5] that, when a phase transition occurs, one of the free energy functions is the same for both phases. In the particular case of superconductivity, the Gibbs free energy $G(T, B)$ is a good choice since the independent variables are in that case the temperature T and the magnetic field B (and the pressure which we shall not consider here) which are experimentally controlled quantities. Depending on the behavior of the derivatives of the free energy, the transition will be called first- or second-order (or higher) phase transition. If the first-order derivatives of the free energy are different in both phases, then the transition is called first-order. In that case, both phases have distinct internal structure and the phase transition has a non-zero latent heat. If the first-order derivatives are continuous, the phase transition has no latent heat and is called second order or continuous. Physical quantities proportional to higher-order derivatives of the free energy (like the compressibility) may present discontinuities. At the transition temperature T_c, no distinction between the ordered and disordered phases can be made since both phases present the same structure. Ginzburg and Landau used this model to describe the superconducting transition near T_c, choosing a complex order parameter $\Psi(\vec{r}) = |\Psi| e^{i\varphi(\vec{r})}$ normalized in such a way that $\Psi^*\Psi$ equals the density of superelectrons n_s. They assumed that the free energy density could be expanded in powers of n_s and $(T - T_c)$, and limited the expansion to second order terms: $f(n_s, T) = f_n(T) + \alpha(T) n_s + \frac{1}{2}\beta(T) n_s^2$ in the absence of magnetic field, where f_n is the normal-state free energy density. To ensure a minimum of the free energy below T_c, $\beta(T)$ must have a positive constant term. Ignoring higher-order terms, β can be taken as a positive constant and $\alpha \propto (1 - \frac{T}{T_c})$ since it must be zero at T_c. At the equilibrium state, $\partial F/\partial n_s = 0$ and we have $n_s = -\alpha/\beta \propto 1 - t$, where $t = T/T_c$ is the reduced temperature.

Free energy

When they applied Landau's theory to the superconducting phase transition, Ginzburg and Landau realized that the free energy could not only depend on powers of Ψ but also on spatial derivatives of Ψ in non-uniform situations, thus letting not only the amplitude but also the phase of the order parameter play a role in the expression for the free energy. Ginzburg and Landau proposed the following expression for the free energy [5]

---

[2] Abrikosov applied this theory to type II superconductors in the late 1950s [18] and Gor'kov showed in 1959 that the GL theory was a limiting case of the BCS theory [19].

$$F = F_n + \int_V \left[\alpha\Psi^*\Psi + \frac{1}{2}\beta(\Psi^*\Psi)^2 + \frac{\hbar^2}{4m_e}|\vec{\nabla}\Psi - i\frac{2e}{\hbar}\vec{A}\Psi|^2 \right] dV + \frac{1}{2\mu_0}\int B^2 dV \tag{2.3}$$

where F_n is the normal-state free energy and $\vec{B}$ is the local magnetic induction due to the flowing supercurrent in the superconductor. The first integral runs over the volume V of the superconductor whereas the second is over all space. The electric field reads $\vec{E} = -\partial\vec{A}/\partial t + \vec{\nabla}\mu/e$ where $\vec{A}$ is the vector potential in the London gauge and μ is the electrochemical potential[3]. Both physical quantities $\vec{B}$ and $\vec{E}$ are gauge invariant.

Predictions

The most likely value of the order parameter in the superconducting phase can be found by minimizing the GL free energy. By separately minimizing the free energy with respect to small variations of $\Psi(\vec{r})$ and magnetic field $\vec{B}$, one can deduce the Ginzburg-Landau equations. Inside the superconductor, we have

$$\frac{1}{2m}(-i\hbar\vec{\nabla} + 2e\vec{A})^2\Psi + (\alpha + \beta\Psi^*\Psi)\Psi = 0 \tag{2.4}$$

where $m = 2m_e$ is the mass of a Cooper pair. The boundary condition is given by $(-i\hbar\vec{\nabla}_n + 2e\vec{A}_n)\Psi = -i\hbar\Psi/b$, where b is a real constant and the index n denotes the direction perpendicular to the surface. This first Ginzburg-Landau equation is non-linear in Ψ and shows how the order parameter varies in space.
The second Ginzburg-Landau expression is concerned with the supercurrent $\vec{J}_s$ defined by $\vec{J}_s = \vec{\nabla} \wedge \vec{B}/\mu_0$ and reads

$$\vec{J}_s = \frac{ie\hbar}{m}(\Psi^*\vec{\nabla}\Psi - \Psi\vec{\nabla}\Psi^*) - \frac{4e^2}{m}\vec{A}\Psi^*\Psi \tag{2.5}$$

The Ginzburg-Landau equations predict the same electromagnetic behavior as the London equations, but introduce two characteristic length scales. The first is the GL penetration depth λ which is related to the London penetration λ_L depth by

$$\lambda(T) = \frac{\lambda_L(T)}{\sqrt{(2)}}(1 + 0.74\xi_0/l)^{1/2} = \sqrt{\frac{m\beta}{4\mu_0 e^2|\alpha(T)|}} \tag{2.6}$$

where $\xi_0 = \hbar v_F/(\pi\Delta(0))$ is the BCS coherence length (see below) and l is the mean free path of the electrons. The second length scale is a measure of the typical distance over

---

[3] From thermodynamical arguments, it appears that the electrochemical potential μ (the sum of the electrostatic potential and the chemical potential which, at $T = 0$, is the Fermi energy) rather than the electrostatic potential is more suited to describe how the electrons flow in a metal [5]. A current can appear due to a potential difference or due to a gradient in the concentration of the charge carriers.

which the order parameter Ψ varies and is called the coherence length $\xi(T)$. The GL coherence length is related to the BCS coherence length ξ_0 by

$$\xi(T) = 0.74\xi_0(T)(1 + 0.75\xi_0/l)^{-1/2} = \sqrt{\frac{\hbar^2}{2m|\alpha(T)|}} \tag{2.7}$$

The London theory can be obtained from the GL theory in the limit $\xi \rightarrow 0$.

Type I and type II superconductors

In 1957, Abrikosov noticed that the GL equations had periodic solutions for the order parameter $\Psi(\vec{r})$ and the magnetic field $\vec{B}(\vec{r})$ in the superconductor when the ratio $\kappa = \lambda/\xi$ was large [18]. He interpreted this solution as a flux-line lattice, the zeros of Ψ corresponding to the maxima of $\vec{B}$ thus defining the centers of the flux lines. The ratio κ is called the Ginzburg-Landau parameter and characterizes the type of solution one can obtain from the Ginzburg-Landau equations and therefore the behavior of the superconductor. If $\kappa < 1/\sqrt{2}$ the superconductor is called type I whereas for $\kappa > 1/\sqrt{2}$ the superconductor is called type II. Type I superconductors undergo a first order phase transition to the normal state as the field is raised up to the thermodynamic critical field B_c. This transition is accompanied by a an abrupt drop in the magnetization. In type II superconductors, the Meissner state persists up to a first critical field H_{c1} above which the flux starts to penetrate in the superconductor. This is due to a sign change in the energy associated with the interface of a normal zone and a superconducting zone. The wall energy per unit area can be estimated by the expression $\mu_0 H_c(T)^2(\xi(T) - \lambda_L(T))/2$. When $\lambda_L > \xi$, it is energetically favorable for the system to allow for the creation of normal zones in the superconductor. Thus above H_{c1}, we have the so-called mixed state (or Schubnikov phase) where the magnetic flux penetrates in the form of flux lines carrying each one flux quantum $\phi_0 = h/2e$. The magnetization starts to decrease at H_{c1} and becomes zero at the upper critical field H_{c2} where the system turns normal via a continuous phase transition. The upper critical field is reached when the lattice constant a_0 (the inter-vortex distance) is of the order of the coherence length ξ. In terms of λ and ξ, the expressions for the critical fields read

$$B_{c1}(T) = \frac{\phi_0}{4\pi\lambda^2(T)} ln\left(\frac{\lambda(T)}{\xi(T)}\right) \qquad B_c(T) = \frac{\phi_0}{2\sqrt{2}\pi\lambda(T)\xi(T)} \qquad B_{c2}(T) = \frac{\phi_0}{2\pi\xi^2(T)} \tag{2.8}$$

Fluctuations of the order parameter

We have seen that Ginzburg and Landau use an expansion of the free energy in powers of the order parameter. In phase transitions of order higher than one, fluctuations of the amplitude of the order parameter become important near the transition temperature [5] with the consequence that the above approach is no longer valid near T_c. Landau's theory of phase transitions is a mean field theory, which means that the order parameter has to represent an equilibrium response to an average local field. This is not the case any more when the order parameter undergoes strong amplitude fluctuations. A second-order phase transition will therefore show a behavior which departs from mean-field behavior close to T_c. We thus have to be aware of the fact that very close to T_c, Ginzburg-Landau theory should not be applied. The typical length scale for the amplitude fluctuations of the order parameter is given by the size of the Cooper pairs. If the pairs are very large, as in conventional (type I) superconductors, the order parameter appears averaged over a huge volume and the effects of fluctuations remain negligible up to a few μK of T_c. In cuprate superconductors, which are extreme type II superconductors, the pairs are smaller which increases the effect of the fluctuations in these systems. The width $\Delta T_f = |T_f - T_c|$ of the regime where fluctuations become important can be estimated by assuming that T_f is reached when the fluctuations of $|\Psi|$ become of the order of $|\Psi|$ itself (Ginzburg criterion)[4]. The normalized width $\Delta T_f/T_c$ reads

$$\frac{|T_f - T_c|}{T_c} \equiv G_i = \frac{1}{2}\left(\frac{\mu_0 \gamma k_B T_c}{4\pi B_c^2(0)\xi^3(0)}\right)^2 \sim 10^{-2} \text{ for HTS} \tag{2.9}$$

where G_i is the Ginzburg number which amounts basically to the ratio of the thermal energy divided by the condensation energy in a volume $\xi^3(0)$. Using the values $\gamma = 5$, $T_c = 92K$, $\lambda(0) = 1400\text{Å}$ and $\xi(0) = 15\text{Å}$ suited for YBCO, we get $|T_f - T_c| \approx 1.1K$. The quantity γ is the anisotropy of the superconductor defined in the next paragraph.
The order parameter also fluctuates in the presence of moving vortices in the superconductor and we refer the reader to the next section for the subject of vortices.

2.1.2 Anisotropy

In order to apply the Ginzburg-Landau theory to cuprates, we still need to account for the anisotropy of these superconductors. This can be done by introducing effective masses for the electrons moving along the different axis a, b and c of the superconductor. Since the anisotropy in the ab-plane is very small for YBCO (the lattice constants along the a and b axis differ by less than 2 %), we set $m_a = m_b = m_{ab}$. The anisotropy parameter is defined by

$$\gamma^2 = \frac{m_c}{m_{ab}} = \left(\frac{\lambda_c}{\lambda_{ab}}\right)^2 = \left(\frac{\xi_{ab}}{\xi_c}\right)^2 > 1 \tag{2.10}$$

The expressions for the lower and upper critical fields depend on the orientation of the applied magnetic field $\vec{B}_a$ and are given by

---

[4] See for example [7,20] for critical fluctuations and [11,20,21] for the Ginzburg criterion.

$$(\vec{B}_a \text{ along c axis}) \qquad B^c_{c1} = \frac{\phi_0}{4\pi\lambda^2_{ab}} ln(\kappa_{ab}) \qquad B^c_{c2} = \frac{\phi_0}{2\pi\xi^2_{ab}} \tag{2.11}$$

$$(\vec{B}_a \text{ along ab plane}) \qquad B^{ab}_{c1} = \frac{\phi_0}{4\pi\lambda_{ab}\lambda_c} ln(\sqrt{\kappa_{ab}\kappa_c}) \qquad B^{ab}_{c2} = \frac{\phi_0}{2\pi\xi_{ab}\xi_c} \tag{2.12}$$

whereas the thermodynamic critical field is independent of the applied field orientation and is given by

$$B_c = \frac{\phi_0}{2\sqrt{2}\pi\xi_{ab}\lambda_{ab}} = \frac{\phi_0}{2\sqrt{2}\pi\xi_c\lambda_c} \tag{2.13}$$

Continuous versus discrete description: the Lawrence-Doniach model

The anisotropic Ginzburg-Landau theory provides a description in terms of continuous anisotropy which is valid as long as the variation of the order parameter along the c axis is smooth enough. If the anisotropy strongly increases, the discreteness of the structure becomes relevant and the superconductor should be considered as a stack of superconducting layers weakly coupled by Josephson tunneling as proposed by Lawrence and Doniach (LD) [22,23] in 1971. In fact the anisotropic GL and London theories are contained in the LD model as limiting cases when the coherence length along the c axis ξ_c is much larger than the interlayer spacing s [24]. In the discrete approach, the order parameter $\Psi_n(x,y)$ is defined for each layer n and the free energy reads [7,24]

$$\begin{aligned} F = s\sum_n \int_S \Big(\alpha|\Psi_n|^2 + \frac{1}{2}\beta|\Psi_n|^4 - \frac{\hbar^2}{2m_{ab}}|\vec{\nabla}\Psi_n - i\frac{2e}{\hbar}\vec{A}\Psi_n|^2 - \frac{\hbar^2}{2m_c s^2}|\Psi_n - \Psi_{n-1}|^2\Big)dS \\ + \frac{1}{2\mu_0}\int B^2 dV \end{aligned} \tag{2.14}$$

where the sum runs over the layers, the first integral over the surface of each layer and the second integral over all space. The last term in the surface integral depends only on the phase difference $\varphi_n - \varphi_{n-1}$ of the order parameter between two adjacent layers when all $|\Psi_n|$ are equal, which indicates the Josephson nature of the coupling between the layers. The continuous approach remains suited for YBCO because of its relatively weak anisotropy. On the other hand, for $Bi_2Sr_2Ca_1Cu_2O_8$ (BSCCO), for instance, the discrete approach has to be used since its anisotropy, as measured by γ, is ten to forty times larger than YBCO's. To get a feeling of the discreteness or not of a system, one can compare the coherence length $\xi_c(T)$ to the spacing s between superconducting layers. When $\xi_c \lesssim s$ and for a the magnetic field applied parallel to the ab plane, the discrete description should be applied [7,25].

From isotropic to anisotropic description: scaling rule

A useful scaling rule allowing to map the quantities known for the isotropic case to the anisotropic case has been proposed by Blatter *et al.* [7,21,26]. They first introduce the rescaled coordinates, vector potential and magnetic field

$$\begin{array}{lll} x = \tilde{x} & y = \tilde{y} & z = \dfrac{\tilde{z}}{\gamma} \\ A_x = \tilde{A}_x & A_y = \tilde{A}_y & A_z = \gamma \tilde{A}_z \\ B_x = \gamma \tilde{B}_x & B_y = \gamma \tilde{B}_y & B_z = \tilde{B}_z \end{array}$$

where a quantity q in the rescaled isotropic system is denoted by $\tilde{q}$. For an applied magnetic field parallel to the c axis, a quantity Q in the anisotropic case can be deduced from the (known) expression of $\tilde{Q}$ in the isotropic case using the scaling rule

$$Q(H, T, \xi_{ab}, \lambda_{ab}, \gamma) = s_Q \tilde{Q}(H, \gamma T, \xi_{ab}, \lambda_{ab})$$

where the scaling parameter is $s_Q = 1/\gamma$ for a volume, energy, temperature or action and $s_Q = 1$ for a magnetic field parallel to the c axis. This mapping remains valid as long as the continuous anisotropic GL theory can be applied.

2.2 Properties of the mixed state

The properties of the flux lattice have been extensively described in the literature, see for example the reviews by G. Blatter *et al.* [21] and E. H. Brandt [24]. One should also remember the important work by Campbell and Evetts [27] where many aspects of the flux-line lattice properties were already discussed. Since we deal with an anisotropic compound in this work, we shall write the expressions for the anisotropic case when necessary. Furthermore, we will only consider the particular case where the external applied field $\vec{B}_a$ is parallel to the c axis of the superconductor. The geometry we are interested in is depicted in Fig. 2.1.

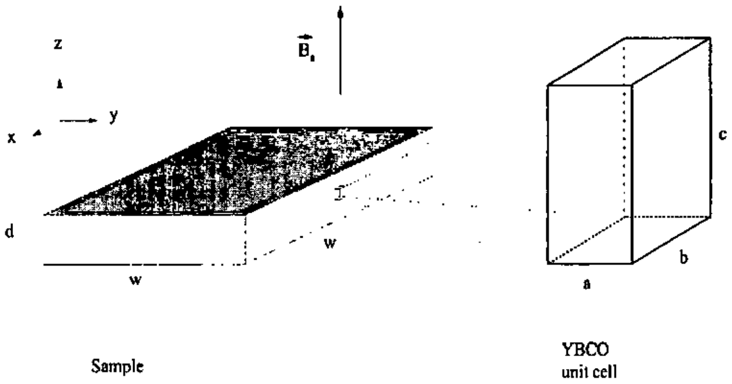

Figure 2.1: *Geometry of the problem.*

2.2.1 Flux lines

A flux line[5] is an elastic object which has a one-dimensional character. The existence of a line tension for the vortex comes from the coherence of the flux line along the z axis and describes the elastic response of the vortex line. The definition of a line tension thus looses sense in the limit of very large anisotropy. For vortices along the z axis (perpendicular to the superconducting plane) and for wavelengths $1/k \gg \lambda$, the line tension, given by the sum of the contributions from the kinetic energy of the supercurrents plus the magnetic field energy [7], reads

$$\epsilon_l = \epsilon_0 ln(\lambda_{ab}/\xi_{ab}) \tag{2.15}$$

$$\text{where} \quad \epsilon_0 = \frac{\phi_0^2}{4\pi\mu_0\lambda_{ab}^2} \quad [J/m] \tag{2.16}$$

The quantity ϵ_0 in the above expression is a basic energy scale (per unit length) which will appear in many expressions involving vortices and their interactions. A more formal definition of a single vortex line consists in describing this object as a topological excitation of the superconductor characterized by a line singularity in the phase of the order parameter [21]. The phase of the order parameter changes by 2π along a closed curve encircling once the vortex line. In the core region extending a length ξ away from the singularity, the order parameter drops to zero. Circular screening currents proportional to the phase gradient arise in a region extending a distance λ away from the singularity. The total flux threading the flux line is the flux quantum ϕ_0.

---

[5] The expressions *vortex* or *vortex line* will be used as well to refer to a *flux line*.

The interaction energy E_{12} between two vortex lines is repulsive. Taking two infinitely long vortices separated by a distance r_{12} in the limit of interest $\kappa = \lambda/\xi \gg 1$, this energy can be calculated by evaluating the effect of the screening currents of the first vortex line at the location of the second vortex line. The expression reads [7,28]

$$E_{12} = \frac{\phi_0^2}{2\pi\mu_0\lambda^2} K_0\left(\frac{r_{12}}{\lambda}\right) \quad [J/m] \tag{2.17}$$

where $K_0(r_{12}/\lambda)$ is a zeroth-order modified Bessel function which behaves like $ln(\lambda/r_{12})$ when $r \ll \lambda$ and decays essentially like $e^{-r_{12}/\lambda}$ at large distances [28].

Flux motion When a current density $\vec{j}$ flows in the superconductor, a vortex line feels a Lorentz force (per unit length) $\vec{f_L} = \phi_0\vec{j} \wedge \vec{n}$ where $\vec{n}$ is a unit length vector directed along the z axis (parallel to the flux lines). The vortices thus move transverse to the current and, assuming a displacement velocity $\vec{v}$, an electric field $\vec{E} = \vec{v} \wedge \vec{B}$ parallel to the current will be induced [10,29], giving rise to dissipation in the superconductor. The dissipation arises from two effects contributing roughly equally [24]. First, the eddy currents surrounding each flux line have to pass trough the normal core which will lead to dissipation. The other source of dissipation is linked to a delay effect for the order parameter to recover at places in the superconductor where a vortex core has passed by [30].

2.2.2 Flux lattice

We come now to the properties of the whole set of the flux lines: the flux lattice. As the magnetic field penetrates the superconductor above H_{c1} in the form of flux lines, an organized flux lattice forms and if the superconductor is perfect (homogeneous, no defects), the result will be a triangular Abrikosov vortex lattice corresponding to a configuration of the vortices where the energy is minimized. The lattice constant is given by $a_\triangle = (2\phi_0/\sqrt{3}B)^{1/2} = (2/\sqrt{3})^{1/2}a_0$ where $a_0 = \sqrt{\phi_0/B}$. In real superconductors, however, the flux lattice is distorted by thermal fluctuations, structural defects and external electromagnetic forces. These constraints, when not too strong, can be regarded as perturbations in which case the flux lattice can be treated as an elastic medium in metastable equilibrium. Assuming that the magnetic field is applied along the z axis, the distorted flux lattice can be parameterized with a two-component displacement field $\vec{u}(\vec{R}_i, z) \equiv \vec{u}_i(z) = \vec{r}_i(z) - \vec{R}_i = (u_{i,x}(z); u_{i,y}(z))$ measuring the displacement of the *ith* vortex from its ideal position $\vec{R}_i = (X_i; Y_i) = (n_i\sqrt(3)a_\triangle/2; (2m_i + n_i)a_\triangle/2)$ where n_i and m_i are integers [21]. The elastic energy $F_{elast}(\vec{u})$ of the distorted state is given by [21,24]

$$F_{elast}(\vec{u}) = \frac{1}{2}\int_{BZ} \frac{d^3k}{(2\pi)^3}[u_\alpha(\vec{k})\Phi_{\alpha\beta}(\vec{k})u_\beta(-\vec{k})] \tag{2.18}$$

with $\Phi_{\alpha\beta}(\vec{k})$ the elastic matrix of the vortex lattice and $\vec{u}(\vec{k})$ the Fourier transform of $\vec{u}_i(z)$. The indices appearing twice in the equation are summed over. The integration runs over the Brillouin zone limited in the plane by $k = |\vec{k}| \leq |\vec{k}_{BZ}| = \sqrt{4\pi}/a_0$ and along the z axis by $k_z \leq 2\pi/\xi$. The elastic matrix is related to the elastic moduli c_{11} for uniaxial compression, c_{44} for tilt and c_{66} for shear deformation by

$$\Phi_{\alpha\beta} = (c_{11}(\vec{k}) - c_{66})k_\alpha k_\beta + \delta_{\alpha\beta}[c_{66}(k_x^2 + k_y^2) + c_{44}(\vec{k})k_z^2)] \tag{2.19}$$

in the local continuum limit of the theory holding as long as $k \ll k_{BZ}$. The elastic energy density in the local limit reads $c_{11}(\vec{\nabla}\vec{u})^2 + c_{66}(\vec{\nabla}_\perp\vec{u})^2 + c_{44}(\partial_z\vec{u})^2$, where $\vec{\nabla}_\perp = (\partial_y; -\partial_x)$. This limit may be used as long as the nearest-neighbor distance a_0 satisfies $a_0 > \lambda$. When a_0 becomes smaller than λ, the vortex-vortex interaction extends beyond the nearest-neighbors and the elastic moduli c_{11} and c_{44} become dispersive (nonlocal limit). In the anisotropic case and for $a_0 < \lambda_{ab}$, we have [21,24]

$$c_{11}(\vec{k}, B) = \frac{B^2}{\mu_0}\frac{1}{1 + \lambda_c^2(k_x^2 + k_y^2) + \lambda_{ab}^2 k_z^2}\left[\frac{1 + \lambda_c^2 k^2}{1 + \lambda_{ab}^2 k^2}\right] \tag{2.20}$$

$$c_{44}(\vec{k}, B) = \frac{B^2}{\mu_0}\frac{1}{1 + \lambda_c^2(k_x^2 + k_y^2) + \lambda_{ab}^2 k_z^2} + c_{44}^{sv}(\vec{k}, B) \tag{2.21}$$

$$c_{66}(B) \approx \frac{B\phi_0}{16\pi\mu_0\lambda_{ab}^2} = \frac{\epsilon_0}{4a_0^2} \quad [N/m^2] \tag{2.22}$$

The second term $c_{44}^{sv}(\vec{k})$ in the expression for the tilt modulus is the isolated-vortex contribution and corresponds to the single vortex line tension as the interaction between vortices vanishes when the magnetic field goes to zero [31]. In this limit, $c_{44} \to c_{44}^{sv}$ and $\epsilon_l = a_0^2 c_{44}^{sv}$. The line tension comprises two terms

$$\epsilon_l(k_z) = \frac{\epsilon_0}{2\gamma^2} ln\left(\frac{\gamma^2 k^2}{1 + k_z^2\lambda_{ab}^2}\right) + \epsilon_0\frac{ln(1 + k_z^2\lambda_{ab}^2)}{2k_z^2\lambda_{ab}^2} \tag{2.23}$$

arising from the Josephson coupling and the electromagnetic coupling, see below. In the case of a straight flux line ($k_z = 0$), the line tension is given by Eq. (2.15). A more complete description can be found in Ref. 21 and Ref. [24].

The above analysis is based on the anisotropic London theory and applies for $B \lesssim 0.2B_{c2}$ and $\lambda_{ab}/\xi_{ab} > 2$. The extension of these expressions to higher fields brings, among others, a correction factor $(1 - B/B_{c2})^{-1/2}$ providing the vanishing of the elastic moduli when $B \to B_{c2}$. The dispersion is observed mainly for the compression and tilt moduli whereas the shear modulus remains independent of $\vec{k}$ as long as $B \lesssim 0.2B_{c2}$. An estimate of the relative importance of the moduli at zero temperature and in the non-dispersive limit yields $c_{11}/c_{66} \approx c_{44}/c_{66} \geq 10^3$ which essentially means that the easiest deformation taking place in a vortex lattice will be shear. A first approximation depicts thus the vortex lattice as essentially incompressible and untiltable.

Displacement of one vortex line in the flux lattice

In a perfect, stable Abrikosov lattice, each vortex experiences a zero net force. If we displace laterally a vortex by a distance δx from its equilibrium position (Fig. 2.2), this vortex will experience a restoring force f_r proportional to the displacement (provided $\delta x/a_0 < 1$). When the magnetic field B verifies $B_{c1} \ll B \ll B_{c2}$, the restoring force per unit length can be written [7, 27]

$$f_r = K\delta x \approx \sqrt{3}\frac{\phi_0 B}{\mu_0 \pi \lambda^2}\delta x = 4\sqrt{3}\frac{\epsilon_0}{a_0^2}\delta x \quad [N/m] \tag{2.24}$$

where K is the restoring force constant. This expression is obtained by taking into account only the nearest neighbors of the displaced vortex.

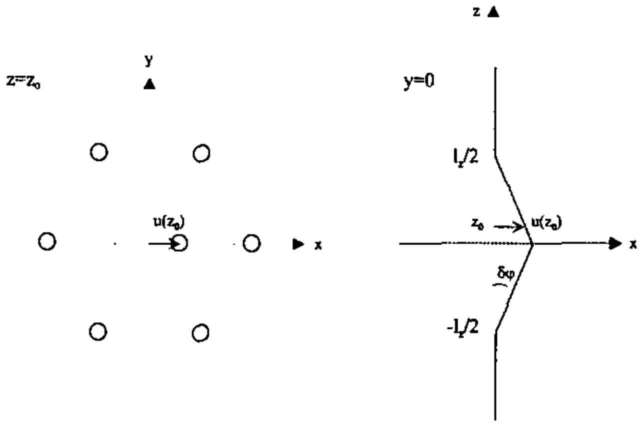

Figure 2.2: *Deformation of a flux line. Left figure shows a top view of the vortex lattice at $z = z_0$. The displaced vortex is at the position ($x = 0; y = 0$). Right figure shows a lateral view corresponding to the plane $y = 0$.*

If the vortex is stiff ('raw spaghetti'), the whole vortex line is displaced. But if the vortex is soft ('cooked spaghetti'), then only a segment of the vortex line may be displaced. The typical length of the displaced segment will thus depend on the elastic properties of the flux line. Let us estimate this length for the geometrical situation depicted in Fig. 2.2. A displacement of the flux line by an amplitude $u_0 = l_z tan(\delta\varphi)/2 \simeq l_z\delta\varphi/2$ at $z = 0$ implies an energy increase δE of the deformed vortex line due to the restoring force exerted by the surrounding vortices and due to the stretching of the line (we assume that the line energy of the vortex does not depend on the angle $\delta\varphi$ which is true for small angles, see for instance [21]). The line energy of the vortex reads $E_l = \epsilon_l l_z$ whereas the lateral displacement increases the vortex length by $\delta l_z = l_z(\delta\varphi)^2/2$. The energy increase δE_l due to the stretching of the line is then given by $\delta E_l = (\partial E_l/\partial l_z)\delta l_z$, yielding $\delta E_l = 2\epsilon_l u_0^2/l_z$. The increase in energy δE_r due to the restoring force is given by the integral of the restoring energy $Ku^2(z)/2$ from $z = 0$ to $z = l_z/2$, where $u(z) = l_z\delta\varphi/2 - z\delta\varphi$. The integral has still to be multiplied by a factor of two accounting for the total vortex length. We obtain $\delta E_r = Kl_z u_0^2/6$. By minimizing the total energy increase $\delta E_l + \delta E_r$ due to the lateral displacement of the vortex with respect to l_z, one can deduce the optimal deformation length l_z^{opt} for the vortex line

$$l_z^{opt} = 2\left(\frac{3\epsilon_l}{K}\right)^{1/2} \tag{2.25}$$

In the anisotropic case and with a GL parameter suited for YBCO ($\lambda_{ab}/\xi_{ab} \approx 100$), we obtain

$$l_z^{opt} \simeq 2.8\frac{a_0}{\gamma} \approx \frac{a_0}{\gamma} \tag{2.26}$$

It is interesting to mention that a non-zero line tension ϵ_l for a vortex means that this vortex can be seen as an elastic string which is not at rest but undergoes some stretching force ϵ_l exerted on it. The 'spring constant' ϵ_l/l of the vortex along the z axis will thus depend on its length l since the line tension is constant. The consequence is that a long vortex ($l > l_z^{opt}$) will be softer than a short one ($l < l_z^{opt}$).

Flux lines versus pancakes

So far, we have assumed that vortices can be described as continuous objects which is true as long as the anisotropy is not too large. In very anisotropic superconductors, the use of the LD model becomes necessary. As sketched in section 2.1.2, this model treats superconductivity within the layers via the GL theory and the current j_J between adjacent layers via the Josephson effect. The structure of a vortex in different geometries has been investigated: isolated thin film [32], stack of uncoupled layers ($j_J = 0$) [33–35] and stack of coupled layers ($j_J > 0$) [33,34]. In fact, in strongly anisotropic superconductors, a vortex directed along the c axis may be regarded as a stack of two-dimensional pancake vortices located in the superconducting planes linked by Josephson strings threading through the insulating layers. These pancake vortices interact with each other in the ab plane (intraplane interaction) and along the c axis (interplane interaction). Two pancakes in the same layer will repel each other whereas the force exerted by a pancake on another pancake in a different layer will be attractive (see for instance [25]). This means that if one pancake vortex is placed in each layer, the zero-temperature configuration is a straight stack of pancakes aligned parallel to the c axis.

The nature of the coupling along the c axis has two origins. First, each layer is electromagnetically coupled to the others since screening currents appearing in the nth layer

in response to a vortex core located in the nth layer will also set up within the neighboring layers[6]. The second coupling arises from a non-zero phase difference of the order parameter between the nth layer and its two adjacent neighbors. A Josephson current j_J, originating from this phase difference, will appear between the adjacent layers.
If the intraplane interaction energy is much larger than the interplane coupling, the pancakes are no longer aligned along the c axis. The crossover to a two dimensional behavior of the vortices is governed by the magnetic field $\vec{B}$, since the interaction energy between pancake vortices in the plane depends on the inverse lattice spacing squared[7] $a_0^{-2} = B/\phi_0$ whereas the interplane coupling is field independent (see Eq. 2.14) [7]. Both energies will be equal at the crossover field B_{dcpl} given by [11,34,36]

$$B_{dcpl} \simeq \frac{\phi_0}{\gamma^2 s^2} \tag{2.27}$$

Above B_{dcpl}, the pancakes are no longer correlated along the c axis and the system is 2D. A numerical estimate for YBCO yields a decoupling field of the order of B_{c2}^c whereas for BSCCO, we get $B_{dcpl} \approx 1T$. It is thus appropriate to use a continuous description for the vortices in YBCO for intermediate field regimes.

2.2.3 Thermal fluctuations

Thermal fluctuations are considerably enhanced in HTS not only due to the high transition temperature but also to the important anisotropy $\gamma^2 = m_c/m_{ab}$ which softens the flux lattice. Combined together, these two effects produce an effective fluctuation temperature $T_{eff} \simeq \gamma T_c$ which may become of the same order of magnitude as the characteristic energy in the superconductor $\epsilon_0 a_0$ [21]. The ratio of these two quantities can be expressed in terms of the Ginzburg number which measures the importance of thermal fluctuations as we saw in Sec. 2.1.1. As a consequence, thermal fluctuations may melt the flux lattice over a rather large temperature interval in the $B - T$ phase diagram.

Amplitude of single flux line fluctuations and entanglement

The mean-squared thermal displacement of a flux line can be estimated within the linear elasticity theory by ascribing an average energy $k_B T/2$ to each elastic mode of the flux lattice [24]. The calculation of $< |\vec{u}_i(z)|^2 >_{th}$, where $< ... >_{th}$ denotes an average over all thermal fluctuations, is the main difficulty in the problem and has been performed by several authors [21, 34, 37–39]. We stress again that anisotropy, as well as non locality $(2\pi/k < \lambda)$, enhance the effect of thermal fluctuations.
In the case of a single flux line, we can write $k_B T \sim c_{44}^{sv} \Lambda_d^2 l$ where $\Lambda_d = (< |\vec{u}_i(z)|^2 >_{th})^{1/2}$ is the root mean square distance traveled perpendicular to the z axis and l, the length of

---

[6] The vector potential $\vec{A}$ in a given layer n depends on the gradient $\nabla\varphi_i$ of the phase of the order parameter in each layer i.

[7] We can use here the same restoring force constant as in Sec. 2.2.2, but taking $l_z = s$.

the vortex line. In the case where l is limited by the thickness d of the superconductor, the expression for Λ_d can be written [40]

$$\Lambda_d^2 = \frac{8\pi^2\mu_0\gamma^2 k_B T\lambda_{ab}^2(T)d}{\phi_0^2 ln(\lambda_{ab}/\xi_{ab})} = \Lambda_0^2\left(\frac{1}{T} - \frac{1}{T_c}\right)^{-1} \tag{2.28}$$

where $\Lambda_0^2 = 8\pi^2\mu_0\gamma^2 k_B\lambda_{ab}^2(0)d/(\phi_0^2 ln[\lambda_{ab}(0)/\xi_{ab}(0)])$. The explicit temperature dependence of $\Lambda_d(T)$ has been calculated using the Ginzburg-Landau expression for $\lambda_{ab}(T)$ whereas the anisotropy has been introduced using the scaling rule described above (Sec. 2.1.2). It thus appears that collisions between adjacent vortex lines will be important whenever $\Lambda_d \lesssim a_0$, which will lead to an entanglement of the vortices. The crossover temperature T_{ent} between an entangled and a disentangled flux-line lattice can be estimated for different fields by setting $\Lambda_d(T_{ent}) = a_0$ which implies

$$\frac{1}{T_{ent}} = \left(\frac{\Lambda_0}{a_0(B)}\right)^2 + \frac{1}{T_c} \tag{2.29}$$

2.2.4 Melting

At the moment, a detailed theory for the three dimensional flux-lattice melting does not exist [41,42]. Estimates of the melting temperature T_m are based on melting criteria and/or computer simulations [43–45]. A useful approach to estimate T_m is the Lindemann criterion which provides reasonable estimates of the solid-liquid transition temperature in various materials, see for instance Ref. 41 and references therein. Lindemann proposed [46] that the melting of a crystalline lattice occurs when the root mean square thermal displacement of its components becomes comparable to a fraction c_L of the lattice constant. This approach assumes wave-vector independent elastic constants for the vortex lattice [40] and is thus valid in the local limit of the elastic theory where $2\pi/k \gg \lambda$. The melting criterion reads

$$< u^2(T_m) > \approx c_L^2 a_0^2 \tag{2.30}$$

with the Lindemann number c_L satisfying $c_L \approx 0.1 - 0.2$ in classical systems (see e.g. Ref. 41 and references therein). Values up to $c_L = 0.4$ have been reported for HTS [38,43]. In the intermediate regime $0.1T < B < 10T$, the Lindemann number was found roughly constant, $c_L \approx 0.2$, from Monte-Carlo simulations [43]. A melting line $B_m(T)$ for a 3D vortex lattice can be derived in the following way. Thermal fluctuations will produce flux line wandering and distortions. Since we have estimated the energy increase δE of a distorted flux line in Sec. 2.2.2, we can estimate the melting temperature of the lattice by equating the energy $\delta E(l_z^{opt})$ to $k_B T$. Assuming that melting occurs when the Lindemann criterion $u^2 = c_L^2 a_0^2$ is fulfilled, we find

$$k_B T_m^{3D} = K\left(\frac{3\epsilon_l}{K}\right)^{1/2} c_L^2 a_0^2 + \left(\frac{\epsilon_l}{(\epsilon_l/K)^{1/2}}\right) c_L^2 a_0^2 = \frac{4}{\sqrt{3}}(K\epsilon_l)^{1/2} c_L^2 a_0^2 \qquad (2.31)$$

From the above expression, one deduces for the anisotropic case

$$B_m(T) = \frac{4}{\sqrt{3}\pi^2\mu_0^2} \frac{\phi_0^5 c_L^4}{\gamma^2 (k_B T)^2 \lambda_{ab}^4(T)} ln(\lambda_{ab}/\xi_{ab}) \qquad (2.32)$$

This expression holds for magnetic fields verifying $B_m < 0.2B_{c2}$, so that the vortex cores do not overlap. The temperature dependence of B_m is governed by the temperature dependence of $\lambda_{ab}(T)$ and follows roughly $B_m(T) \propto (1 - T/T_c)^2$ using the GL expression for $\lambda_{ab}(T)$. In fact, a simple power-law behavior turns out to be insufficient to describe the melting line over a large range of magnetic fields and temperatures. It is more a convenient way to describe the melting line rather than a real physical fact. Expressions which go beyond this simple power-law dependence were calculated and can be found in Ref. 21, 38 and 47.

With reference to our experiment, the above expression may be written in terms of an inverse inductance by assuming, in analogy to the $B = 0$ case, $L^{-1}(T, B) = (\mu_0\lambda_{ab}^2(T, B)/d)^{-1}$. At $T = T_m$, we obtain

$$\frac{1}{L(T_m, B)} = \frac{3^{1/4}\pi}{4} \frac{\gamma k_B T_m}{\phi_0^2 c_L^2} \frac{d}{a_0(B)} \Big(ln(\lambda_{ab}/\xi_{ab}) \Big)^{-1/2} \qquad (2.33)$$

This expression allows a direct comparison with the data. It should be noted, however, that differences emerge in the numerical prefactor (up to a factor of 5) between the expressions proposed in the literature [11, 38, 39, 48].

Since the above expressions are qualitative due to the phenomenological nature of the melting criterion, we understand that the prefactors are not of major importance here. Furthermore, the value of c_L is not precisely known, thus adding to the uncertainty of the numerical estimates that can be obtained from these expressions.

2D melting

In a two dimensional vortex lattice, at $T > 0$, pairs of edge dislocations are spontaneously nucleated [21, 24]. Such edge dislocations interact logarithmically with each other leading to the existence of a Berenziski-Kosterlitz-Thouless-type transition [49] in the system. As the temperature increases, the system undergoes a dislocation-mediated (BKT-like) melting at a temperature [50, 51]

$$T_m^{2D} = \frac{d a_\Delta^2 c_{66}}{4\pi k_B} = \frac{d\phi_0^2}{32\sqrt{3}\pi^2\mu_0 k_B \lambda_{ab}^2} \qquad (2.34)$$

for a film of thickness d. The thickness of the sample should be replaced by the interlayer spacing s for a very anisotropic superconductor. To be accurate, one should multiply the melting temperature by a factor $A \lesssim 1$ accounting for the renormalization of the shear modulus c_{66} due to the presence of bound dislocation pairs in the vortex lattice, see Ref. 21 for instance). Notice that $T_m^{3D} = T_m^{2D}$ when $d \approx a_0/\gamma$ for $c_L = 0.1$ [24] which corresponds to the criterion giving the crossover field above which the flux lines decouple into pancakes (see Sec. 2.2.2).

2.2.5 Thin films

For a very thin superconductor where $d \lesssim \lambda$, the screening of the flux quantum carried by the vortex cannot be achieved any more over the distance λ because of the reduced thickness of the sample. The screening currents will thus circulate over a larger distance λ_{eff} given by $\lambda_{eff} = 2\lambda_{ab}/d$ for our geometry, with the consequence that vortices will interact logarithmically up to distances reaching λ_{eff} instead of λ_{ab}, see e.g. Ref. 32 and Ref. 52. In the limit of very thin films, when $d \to 0$, the interaction between pancakes will remain logarithmic up to arbitrarily large distances [32].

2.3 Pin mechanisms and disorder

The pinning of flux lines emerges basically from local variations of the order parameter (core interaction) and of the circulating supercurrent (magnetic interaction) linked to the presence of defects in the structure of the superconductor. The energy of a flux line passing through a defect will be affected and a resulting attractive force will tend to pull the flux line back to the defect position, an energetically favorable position. The defects deviate from the surrounding material by having different density or electron-phonon coupling resulting in a local variation of the value of T_c. Defects may also induce variations in the electron mean free path by increasing the electron scattering, which will affect the value of $\kappa = \lambda/\xi$ [53]. Perturbations of the supercurrent result from large inclusions, boundary conditions or thickness variations of the superconductor. Such perturbations have a long range interaction and are mainly relevant close to H_{c1} [52, 53]. According to Ref. 54, the pinning energy in this case is expected to be typically κ times smaller than the pinning energy resulting from smaller defects of typical size ξ, apart from the pinning due to thickness variations of the superconductor which we will discuss below. We thus expect that pinning in YBCO films, where $\kappa \approx 100$, will be mainly due to defects with a typical size of the order of the coherence length and to thickness variations of the layer. It should be noted that a periodic and rigid flux-line lattice will not be pinned by any random collection of pinning centers since the rigidity of the lattice will prevent it from accommodating to the underlying array of pinning centers. Pinning in that case might only occur in the case of a commensurate distribution of the flux lines and the pinning centers. The vortex lattice is however not perfectly rigid and the paths of individual flux lines will deviate from their equilibrium position in the periodic Abrikosov lattice to lower their energy by passing through favorable pinning sites. This distortion of the flux-line lattice will occur when the increase in elastic energy of the flux lattice due to its deformation is weaker than the energy gain provided by pinning.

In the following, we discuss the main type of defects which we expect to play a role for the pinning of the vortices in our films.

2.3.1 Point defects

We treat here the case of point defects which represent an uncorrelated pinning source in the film. Departure from stoichiometry and interstitials will locally affect the superconducting order parameter because of the very short coherence length in HTS. Oxygen vacancies are known to occur in YBCO and represent the typical candidate for a point defect acting as a weak pinning center and distributed close to randomly in the material. Since in the HTS the order parameter between the superconducting CuO_2 layers is strongly suppressed [55], pinning will be essentially due to oxygen vacancies in the CuO_2 layers.

A quantitative estimate of the pinning force due to an insulating point defect can be made following the work of Thuneberg *et al.* [56] by assuming that pinning by oxygen vacancies is due to an enhancement of electron scattering. The pinning potential is assumed to follow a negative Gaussian profile and, for an isolated vortex, the restoring force $f(r)$ can be written as [53,56,57]

$$f_p(r) \simeq 2.3 f_{pmax} \frac{r}{r_0} e^{-r^2/r_0^2} \tag{2.35}$$

where r is the distance from the defect in the ab plane, $r_0 = 0.81\xi(T)$ and f_{pmax} is the maximum pinning force given by

$$f_{pmax} \approx \frac{10.2}{(1+T/T_c)^4} \frac{B_c^2(T)}{\mu_0 \xi(T)} \frac{\pi D^2}{4} 1.35\xi(0) \quad [N]$$

Here, D is the typical size for the diameter of an oxygen vacancy and these expressions are valid as long as $D \ll r_0$. It is interesting to notice that we have $f(r) \lesssim 0.01 f_p$ for $r/r_0 > 2.5$, meaning that the pinning will not be effective at distances r exceeding $2\xi(T)$. An estimate for YBCO using $D \simeq 2.6$Å (see Sec. 3.1.1) yields a maximum pinning force $f_{pmax} \approx 5 \cdot 10^{-13} N$ at zero temperature. This value decreases by a factor of about 50 when the temperature is 10% below $T_c \simeq 90K$.

The density n_O of oxygen vacancies per unit area is not exactly known in our films. As an approximation, we use the value $n_O \approx 3.5 \cdot 10^{17} m^{-2}$ found for BSCCO single crystals [58]. This corresponds to about 1 vacancy for 77 oxygen atoms, since the density of oxygen atoms for both CuO_2 layers[8] in the YBCO compound is about $2.7 \cdot 10^{19} m^{-2}$. Taking a core surface of about $\pi\xi_{ab}^2$, we obtain an approximate value of two oxygen vacancies per vortex core in YBCO.

---

[8] We assimilate here the two CuO_2 layers to a single 'thick' superconducting layer for simplicity.

Collective pinning

As described above, pointlike defects like oxygen vacancies will pin the flux lines in a superconductor. However, the effect of one single point-defect will not be very strong and the local displacement of a flux line due to such a defect will certainly be much smaller than a_0 [53] meaning that, at a first glance, we do not expect the vortex lattice to be strongly distorted. However, the presence of a large density of point pinning centers may result in a somewhat different conclusion depending on the elastic constants of the vortex lattice. The problem of the summation of the pinning forces was addressed by Campbell and Evetts [27] but the concept of collective pinning was first introduced by Larkin and Ovchinnikov [59] in 1979. They based their approach on the assumption that the superconductor's volume can be subdivided into correlation volumes within which the distortion of the flux-line lattice is not too large, whereas larger distortions, of the order of the lattice constant a_0, appear between such domains. Larkin and Ovchinnikov introduced two characteristic length scales to describe this effect. The correlation length, or collective pinning length, L_c measures the 'coherence' of a flux line along the field direction. A flux-line segment of length smaller than L_c may be considered as almost straight whereas a flux-line segment of length larger than L_c will exhibit a pinning induced deviation from the straight line at least of the order of the lattice constant. The transverse collective pinning length R_c measures the distance up to which the positional long-range order of the vortex lattice is preserved. Weak disorder thus induces a gradual breakdown of the order in the flux-line lattice.

The two collective pinning lengths, L_c and R_c, can be estimated by minimizing the net energy change δE of the vortex lattice, where δE is the sum of a positive contribution due to the elastic distortion energy and a negative contribution resulting from the energy gained by accommodating to the point defects. We first consider the point defects and define the pinning strength $W = n_v < f^2 >$ where $n_v = n_O/d$ is the number of defects per unit volume with d, the thickness of the superconductor, and $< f^2 > \approx f_{pmax}^2/2$ is the mean square force acting on a flux line due to a point defect [54]. Furthermore, while adding the pinning forces due to each defect, we have to remember that the pinning centers are distributed randomly which results in a total pinning force increasing with the square root $\sqrt{N_v} = \sqrt{n_v V_c}$ of the total number of pinning centers. The total (macroscopic) pinning force F_c can be written

$$F_c \approx \frac{f_{pmax}}{\sqrt{2}} n_v^{1/2} V_c^{1/2} \quad [N] \tag{2.36}$$

where f_{pmax} is the maximum (microscopic) pinning force.

The expression for the net energy change per unit volume can now be written

$$\delta E = \frac{1}{2} c_{66} \left(\frac{\xi_{ab}}{R_c} \right)^2 + \frac{1}{2} c_{44} \left(\frac{\xi_{ab}}{L_c} \right)^2 - \frac{f_{pmax}}{\sqrt{2}} \frac{n_v^{1/2}}{L_c^{1/2}} \left(\frac{\xi_{ab}}{R_c} \right) \tag{2.37}$$

where we consider a displacement of the correlation volume V_c over a distance $u = \xi_{ab}$ because the range of the microscopic pinning force is typically ξ_{ab}. In the nonlocal continuum approximation, the above expression turns out to be somewhat uneasy to handle [21] and we restrict the discussion here to the local (non-dispersive) limit. By minimizing Eq. (2.37) with respect to R_c and L_c, we can deduce the expressions for the correlation lengths

$$L_c = \frac{4c_{44}c_{66}\xi_{ab}^2}{n_v f_{pmax}^2} \qquad R_c = \frac{2\sqrt{2}c_{44}^{1/2}c_{66}^{3/2}\xi_{ab}^2}{n_v f_{pmax}^2} \tag{2.38}$$

From these expressions, we can observe that the correlation volume $V_c = R_c^2 L_c$ will decrease as the elastic moduli decrease (softer vortex lattice) or as the density of pinning centers increases.

In a very thin film or for a strongly layered superconductor, the correlation length along the c axis is limited by the thickness d of the sample or the inter-layer distance s. In this limit, the vortex appears as a rigid object and the contribution from the tilt modulus can be dropped. For the total force in an area $(R_c^{2D})^2$ we find

$$F_c^{2D} \approx \frac{f_{pmax}}{\sqrt{2}} n_v^{1/2} d^{1/2} R_c^{2D} \quad [N] \tag{2.39}$$

The expression for the net energy change per unit area can be written

$$\delta E = \frac{1}{2} c_{66} d \left(\frac{a_0}{R_c^{2D}}\right)^2 - \frac{f_{pmax}}{\sqrt{2}} n_v^{1/2} d^{1/2} \left(\frac{a_0}{R_c^{2D}}\right) \tag{2.40}$$

where we assumed that the correlation area is defined in the 2D case by setting $u = a_0$ instead of $u = \xi_{ab}$ [7]. Minimizing Eq. (2.40) with respect to R_c^{2D} allows to deduce the in-plane collective pinning length for a very thin film

$$R_c^{2D} = \frac{\sqrt{2}c_{66}}{n_v^{1/2} f_{pmax}} a_0 d^{1/2} \tag{2.41}$$

As stressed by Tinkham [7], the above expressions account only for elastic deformations of the vortex lattice whereas, in real vortex systems, plastic deformations of the lattice (dislocations) are expected to appear and will strongly influence the positional order in the lattice. In conclusion, the above discussion provides a useful description of the effect of a large number of randomly distributed point defects, but the expressions given above should be regarded as qualitative.

2.3.2 Extended defects

We will see in Chapter 3 that numerous screw dislocations and terraces appear in superconducting YBCO thin films grown by laser ablation, giving rise to thickness variations of the film. Valleys in the thickness profile of the layer will act as pinning regions for the vortices allowing them to lower their energy. The maximum pinning force per unit length due to thickness modulation can be estimated by [57]

$$f_p \approx 2\pi\epsilon_l \frac{\delta d}{d}\frac{1}{l_s} \quad [N/\mathrm{m}] \tag{2.42}$$

where $\delta d/d$ is the relative thickness variation, l_s the average distance between two valleys and ϵ_l, the line energy of a vortex.

Besides the thickness modulation effect, screw dislocations will give rise to another pinning effect since their cores can be considered as a nonconducting cylinder of typical diameter $\xi_{ab}(0)$. For a single flux line directed along the nonconducting core of the screw dislocation, the pinning force per unit length can be estimated by [57]

$$f_{sd} \approx 1.35\frac{B_c^2(T)}{\mu_0}\xi_{ab}(0) \quad [N/m] \tag{2.43}$$

using the same formalism as for point defects. For YBCO and at $T = 0$, we obtain typically $f_{sd} \approx 1.73 \cdot 10^{-3} N/m$.

Planar defects like twin planes may also appear in YBCO films. However, twins form low-angle grain boundaries (see e.g. [60]) and are not expected to affect noticeably the superconductivity in the layer [57].

We shall notice that, in contrast to the previous section where point defects are an uncorrelated source of pinning for the vortices, the defects described in this section represent a *correlated* pinning source which implies the existence of a ('statistical') matching field B_m at which the number of extended defects will be equal to the number of vortices. When the flux line density exceeds the density of these extended defects, the motion of the excess flux lines is expected to be determined by the shear properties of the flux lattice.

2.3.3 Dislocations in the vortex lattice

Up to now, we have mainly considered elastic deformations of the flux-line lattice due to thermal fluctuations or disorder. Plastic deformations however also appear and strongly influence the behavior of the vortex lattice. The importance of dislocations in the flux-line lattice for the layered superconductors was spotted by Feigelman *et al.* [34] and, almost simultaneously, by Vinokur *et al.* [36]. Both papers describe the thermally activated nucleation and motion of edge dislocation pairs in a 2D vortex lattice. Each pair of dislocations carries a flux proportional to the spatial extension of the pair R_g [34]. Consequently, the motion of dislocation pairs in the vortex structure results in a motion of vortices and leads to dissipation in the superconductor. In fact, the motion of a dislocation pair is equivalent to the motion of a vortex row constrained between two edge dislocations of opposite sign. The characteristic energy barrier associated with the creation of such plastic deformations in the vortex lattice can be estimated by [21,34,36]

$$\begin{aligned} U_{pl}^{2D} &\approx \frac{\epsilon_0 s}{4\pi} ln\left(\frac{a_0}{\xi}\right) \\ &= \frac{\phi_0^2}{16\pi^2\mu_0}\frac{s}{\lambda_{ab}^2(T)} ln\left(\frac{a_0}{\xi}\right) \end{aligned} \tag{2.44}$$

for small dislocation pairs of extension $\sim a_0$, which produce the dominant contribution [36]. The quantity s is the interlayer spacing. Such dislocation pairs can be seen as vacancies or interstitials in the vortex lattice. It should be noticed that the above expression holds for pancake vortices. For a very thin film of thickness $s \lesssim d \lesssim min(l_z; L_c)$, the flux lines appear to be very rigid and we expect a quasi-2D vortex lattice. In some sense, the vortices appear as *thick pancakes* of thickness d and the interlayer spacing in Eq. (2.44) above must be replaced by the thickness of the film.

In a 3D vortex lattice, the situation is somewhat different because the creation of an object equivalent to the dislocation pair in 2D (a dislocation loop) requires an infinite energy in the thermodynamic limit [21], unless $R_g = 0$, due to the fact that dislocation loops cannot carry flux in the vortex system. This situation arises because of the absence of magnetic monopoles and due to the one-dimensional character of the flux lines [21,27]. A calculation of the energy barriers associated with plastic deformations of a 3D vortex lattice can be performed by considering that the relevant excitations involve, as for the 2D case, deformations of the flux lattice on a length scale a_0 [61] and by assuming deformations of the vortex lattice in the form of double-kinks. The energy cost for nucleating such a defect in the vortex lattice can be estimated in the same way we estimated the energy increase of a displaced flux line in Sec. 2.2.2. We consider the same geometry as in Fig. 2.2 but we assume a lateral displacement $u = a_0$ independent of z. The total energy increase δE_{dk} is given, again, by the sum of the increase in energy due to the stretching of the vortex line δE_l and the increase in energy due to the restoring force δE_r. In the anisotropic case, we obtain the expression

$$\delta E_{dk} = \epsilon_0 a_0 \left[\frac{2}{\gamma} ln\left(\frac{\lambda_{ab}}{\xi_{ab}}\right) + \frac{19.4}{\gamma^2}\right] \tag{2.45}$$

for a double-kink of length l_z^{opt}. We have to be careful with this calculation since the displacement u reaches a_0 in which case the expression for the restoring force might not be appropriate any more. Nevertheless, we obtain in this way a reasonable estimate for the energy cost of such a deformation in the vortex lattice. This energy barrier was first estimated by Geshkenbein *et al.* [61] who found $U_{pl} \approx \epsilon_0 a_0/\gamma$. The energy increase δE_{dk} can be used as an approximation for the plastic barriers in the vortex medium and we shall assume

$$U_{pl}^{3D} \approx 2\frac{\varepsilon_0 a_0}{\gamma} ln\left(\frac{\lambda_{ab}}{\xi_{ab}}\right) \propto B^{-1/2}\left(1-\frac{T}{T_c}\right) \tag{2.46}$$

Since U_{pl}^{3D} represents the energy necessary to displace a vortex line segment on a scale a_0, it corresponds in fact to a reconnection barrier in the picture where the relative motion of the vortices takes place via cutting and reconnection of the flux lines.

2.4 Vortex phases

After reviewing the influence of thermal fluctuations and pinning on the flux-line lattice, we look more closely in this section at the different vortex phases that can build up in the mixed state of a HTS. Fig. 2.3 shows on the left the mean-field phase diagram for a type II superconductor. A sketch of a phenomenological phase diagram suited for YBCO is also shown in the right part of the figure. Due to the presence of disorder, the vortex lattice is expected to turn into a truly superconducting phase ($\rho(j \rightarrow 0) \rightarrow 0$) named vortex glass as proposed by Fisher and coworkers [11]. We shall discuss the specific properties of this phase in the next paragraph. At low magnetic fields (low vortex density) or high temperatures, the vortex medium appears as a vortex liquid[9]. Both phases, glass and liquid are separated by a melting line $T_g(B)$ as shown in the figure. The vortex liquid phase can be separated into a pinned vortex liquid regime and an unpinned vortex liquid regime. In the former case, the barriers impeding vortex motion still play a role and the resistivity will be of the form $\rho(j \rightarrow 0) \approx \rho_0 e^{-(U/k_BT)}$ whereas in the latter case, a free flux-flow regime takes place ($\rho(j \rightarrow 0) \approx \rho_{ff}$). Finally, the upper critical field line is shown which marks the onset of enhanced diamagnetism in the superconductor. It is however not expected to be a sharp phase transition.

2.4.1 Vortex glass and flux creep

Pinning, and in particular random point pinning, leads to the destruction of long-range *positional* order in the vortex lattice. Fisher *et al.* [11] suggested that such a vortex state where the vortices are fixed in a random pattern is a new thermodynamic vortex phase. The condition for this phase to be a true superconducting state being the existence of a long-range order in the *phase* of the order parameter which is associated with the fact that vortices stay immobile. This is equivalent to saying that the barriers impeding vortex motion have to become arbitrarily large.

Let us briefly discuss the vortex dynamics in this regime. The classical picture for the motion of vortices in a pinning potential is based on the competition between the Lorentz force and the pinning force as described by Anderson and Kim in their flux creep theory [62]. Due to thermal activation, vortices (or vortex bundles) can jump independently over

---

[9] The presence of weak disorder in the vortex system will force a vortex solid to turn into a glass whereas a vortex liquid will remain a liquid [21].

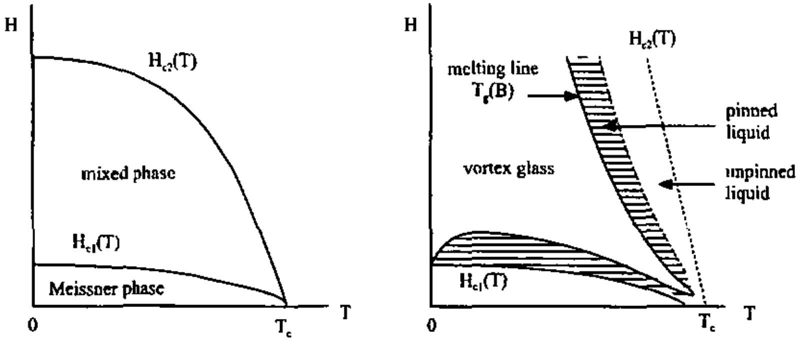

Figure 2.3: *Left: Mean-field phase diagram for a HTS. The normal state is separated from the mixed state by the upper critical-field line $H_{c2}(T)$. The lower critical-field line $H_{c1}(T)$ separates the mixed state and the Meissner phase. Right: Schematic phase diagram for a HTS with moderate anisotropy (YBCO) [2,21].*

the potential barriers U. The presence of an applied current leads to vortex motion, causing a resistivity $\rho \propto e^{-U/k_BT}$. For a large enough applied current, the effective activation barrier goes to zero and a current dependence of the form $U(j) = U_0(1 - j/j_c)$ was assumed [21], with j_c the critical current density. In the single vortex limit (low magnetic fields), the Lorentz force experienced by the vortex is $j\phi_0 L_c$ while the pinning force is given by U_0/ξ. We use here the pinning length scale L_c predicted by the collective pinning model and the fact that the range of the pinning force is typically ξ for point pinning. The critical current is reached when both forces are balanced, yielding $j_c \approx U_0/(\phi_0 L_c \xi)$. A reasonable estimate for j_c can be made by assuming that the pinning energy U_0 must be of the order of the elastic energy increase due to the streching of the vortex line (see Sec. 2.2.2), meaning that we can write $U_0 \approx 2\epsilon_l \xi^2/L_c$. The critical current density in the single vortex limit then reads $j_c \approx 2\epsilon_l \xi/(\phi_0 L_c^2)$.

The current dependence proposed above for $U(j)$ is satisfying as long as individual pinning of the vortex lines is considered but is no longer valid in the collective pinning picture and in the limit of low currents. It can be shown that the energy barrier in the collective creep picture at low currents (see [61] and references therein) is of the form[10]

---

[10] The argument implies the calculation of the optimum distance traveled by a vortex segment between two metastable states, see Ref. [21]. This calculation is based on the condition that the energy gain due to the Lorentz force must balance the distortion and pinning energies of the vortex. It appears that for currents $j \lesssim j_c$, the condition is fulfilled for displacements of the order of ξ. As the current density decreases, the Lorentz force decreases and two favorable metastable states appear to be separated by larger distances. This means that, at low current densities, vortex motion implies the displacement of larger vortex segments over longer distances. As a consequence, probing the vortex medium at low current densities results in exploring the superconductor over large distances.

$$U(j) \simeq U_0 \left(\frac{j_c}{j}\right)^{\mu} \tag{2.47}$$

where $\mu \leq 1$. In the single vortex pinning regime, $\mu = 1/7$ [21]. From this expression, one immediately sees that the resistivity $\rho \propto exp[-U_0/(k_B T) \cdot (j_c/j)^{\mu}]$ in the limit $j \rightarrow 0$ becomes exponentially small at low temperatures in contrast to the conventional creep theory where $U(j \rightarrow 0) = U_0$. The vortex state in the picture of collective pinning thus exhibits a regime with zero linear resistance at low temperatures which Fisher and coworkers [11] identified as a new true thermodynamic phase named vortex glass. It is interesting to notice that the screening current circulating in the superconductor still follows a logarithmic time decay as in Andersons's original work. In the limit of small currents $j \ll j_c$, we have [21]

$$j(t) \approx j_c \left[\frac{k_B T}{U_0} ln\left(\frac{t}{t_0}\right)\right]^{-\frac{1}{\mu}} \tag{2.48}$$

where t_0 is a characteristic time scale in the problem, see for instance the discussion in Ref. [21], p.1350.

The dimensionality of the vortex system is here of some importance, since the phase transition to a vortex-glass state for a 2D vortex medium is expected to occur only at $T = 0$ [11] rather than at a non-zero transition temperature $T_g > 0$. In fact, the presence of weak pinning can lead to a vortex-glass phase in a 2D vortex medium as long as *elastic* deformations of the lattice are involved [34, 63, 64]. The presence of dislocations, and even small dislocation pairs of extension a_0 being equivalent to a point defect in the flux lattice, will naturally lead to a thermally activated flux flow regime since the motion of such dislocations in the 2D flux lattice results in flux transport. In 3D, the problem is somewhat different since the vortex-glass state appears stable with respect to such dislocations [34]. Introducing additional vortices into one plane would require an infinite energy in a 3D vortex medium [21,34]. This corresponds to the fact that dislocation loops in the flux lattice have to lie within the gliding planes of the edge dislocations composing the loop and thus do not add or remove flux from the system. This was pointed out by Campbell and Evetts [27] and justified by geometrical considerations. This particular point marks the main difference between a 2D and a 3D vortex medium in the present context and justifies why a true thermodynamic vortex-glass phase can exist in 3D below a non-zero transition temperature T_g and only at $T = 0$ in 2D. The basic reasons for this situation to appear are first, that vortices are one-dimensional objects and second, that a flux line cannot end in the superconducting material since magnetic monopoles are not physical objects.

2.4.2 Vortex liquid and thermally-activated flux flow

Close above the glass melting line $T_g(B)$, the vortex liquid is still very viscous and exhibits a thermally activated resistivity $\rho \propto e^{-U/k_BT}$ where the energy barrier U is associated with the thermally activated plastic motion of the vortex structure and does not depend on the current density [61, 65, 66]. This TAFF (thermally-activated flux flow) regime is in fact a limiting case of the Kim-Anderson flux creep theory [62] in the limit of small driving forces (small currents) and for current-independent energy barriers. As the temperature increases, the effective barriers for vortex motion decrease and pinning is no longer relevant. A flux-flow (FF) regime takes place where the resistivity can be written $\rho \equiv \rho_{ff} \simeq \rho_n B/B_{c2}$ [67]. We shall discuss the dynamics of the vortex liquid in more details in the next section.

2.4.3 Transition from a vortex glass to a vortex liquid: definitions and predictions of the vortex glass theory

Fisher *et al.* [11] assume a continuous phase transition of the vortex system at T_g and describe it by means of scaling arguments. The static and dynamic features of the transition can be described by a vortex-glass correlation length ξ_{vg} and a relaxation time τ_{vg} which both diverge as the temperature of the transition is approached. The expressions read

$$\xi_{vg} = \xi_{vg0}|1 - T/T_g|^{-\nu} \tag{2.49}$$

$$\tau_{vg} = \xi_{vg}^{z} \tag{2.50}$$

where the two exponents ν and z are referred to as the static exponent and the dynamic exponent, respectively.

The complex ac linear conductivity $\sigma(\omega) = [d(R + i\omega L)]^{-1}$ describing the response of the system in the vicinity of the critical regime at low frequencies can be written [11, 68]

$$\sigma(\omega) = \sigma_0 \left(\frac{\xi_{vg}}{\xi_{vg0}}\right)^{z+2-D} S_{\pm}(\omega\tau_{vg}) \tag{2.51}$$

where D is the dimension and $S_{\pm}(\omega\tau_{vg})$ is a universal function defined above (+) and below (-) T_g.

The phase of the conductivity ϕ_σ defined by $\sigma = |\sigma|e^{i\phi_\sigma}$ is given by [11]

$$\phi_\sigma(T_g) = \frac{\pi}{2}\frac{z-1}{z} \tag{2.52}$$

at T_g.

2.5 Vortex dynamics

We turn now to the problem of characterizing the electromagnetic response of a HTS in the mixed state for the geometry depicted in Fig. 2.1. The response of the superconductor will depend on the dynamical behavior of the vortex medium. We first need the quasi-stationary[11] Maxwell's equations, valid inside and outside the superconductor

$$\vec{\nabla} \wedge \vec{E} = -\frac{\partial \vec{B}}{\partial t} \tag{2.53}$$

$$\vec{\nabla} \wedge \vec{B} = \mu_0 \vec{j} \tag{2.54}$$

The knowledge of the relation between the electrical field and the current density is our main interest here. In the particular case where the barriers U inhibiting vortex motion in the superconductor are negligible, the vortices are free to move (unpinned vortex liquid) and Ohm's law[12] reads

$$\vec{E} = \rho_{ff} \vec{j} \tag{2.55}$$

where $\rho_{ff} \simeq \rho_n B/B_{c2}$ is the flux-flow resistivity [67] and ρ_n is the normal-state resistivity. The viscosity η of the vortex medium is given by $\eta = B^2/\rho_{ff}$ [67].

More generally, the resistivity ρ will depend on the frequency, the temperature, the magnetic field and the current density.

2.5.1 Linear response: thermally-activated flux flow

For a vortex system *above* the melting temperature, the activation barriers remain finite in the small current-density limit. The vortices form a vortex liquid or, better, a pinned vortex liquid. In such a thermally activated regime, the velocity of the vortices can be written in the form $\vec{v} = \vec{v}_0 e^{-U/k_B T}$ [21] and it is related to the electrical field by $\vec{E} = \vec{v} \wedge \vec{B}$. As a result, the vortex liquid develops a diffusive dynamics where the resistivity is

$$\rho \propto \rho_{ff} e^{-U/k_B T} \tag{2.56}$$

This regime was described by Kes *et al.* [69] and is referred to as the TAFF (thermally assisted flux flow) regime. The electrodynamics of a superconductor in this regime is equivalent to the electrodynamics of a normal metal with an exponentially small resistivity [70].

---

[11] The wavelength of the electromagnetic field $2\pi c/\omega$ must be large compared to the sample dimensions, which is easily verified in our case. Our highest frequency is 100kHz: $c/\omega \gtrsim 500m \gg 10^{-2}m$.

[12] We shall remember that in the HTS, we have $\xi << l << \lambda$, where l is the electron mean free path. The HTS are thus in the local limit where Ohm's law holds, see for instance Ref. 5, p.180.

Using Maxwell's equations, we can derive a linear diffusion equation of motion for the magnetic field [69,70]

$$\partial_t \vec{B} = \frac{\rho}{\mu_0} \Delta \vec{B} \tag{2.57}$$

with the diffusion constant $D = \rho/\mu_0$. We are interested in the particular case where the total external applied magnetic field $\vec{B}$ is the sum of a large static magnetic field plus a small ripple of angular frequency $\omega = 2\pi f$, i.e.: $\vec{B} = \vec{B}_0 + \mu_0 \vec{h}_{ac}$ with $\mu_0 h_{ac}/B_0 \ll 1$. Assuming a time dependence $\propto e^{i\omega t}$ for $\vec{h}_{ac}$, the diffusion equation becomes

$$\vec{h}_{ac} = \frac{\rho}{\mu_0 i\omega} \Delta \vec{h}_{ac} \tag{2.58}$$

This equation defines an ac penetration depth λ_{ac} for the magnetic field

$$\lambda_{ac}^2 = \frac{\rho}{\mu_0 i\omega} \tag{2.59}$$

which is related to the skin depth $\delta = [\rho/(\mu_0\omega)]^{1/2}$ [71] by $\lambda_{ac}^2 = -i\delta^2$.
For a thin superconducting film, we can write the sheet impedance of the film $Z_s = \rho/d$

$$Z_s(\omega, T, B) = \frac{i\omega\mu_0\lambda_{ac}^2(\omega, T, B)}{d} \tag{2.60}$$

The calculation of the complex penetration depth λ_{ac} results in calculating the flux velocity by solving the equation of motion for the vortices in the superconductor. A general equation describing the vortex motion should account for the vortex inertia effects, the viscosity of the medium, the existence of pinning in the sample, the elastic restoring force due to the other vortices, the driving force and finally the thermal fluctuations. Such an equation, however, has not been solved yet for any vortex displacement $\vec{u}$. We thus have to perform a few approximations in order to find a solution for the vortex velocity in the superconductor. In particular, the vortex inertia term may be dropped away as long as the frequency of the driving current is well below the gap frequency ω_g, see e.g. [72,73]. Since $\omega_g \approx 10^{13} Hz$ in the cuprates, this contribution will not be relevant for us.

2.5.2 Equation of motion for the Brownian model

In the particular case where vortices are independent from each other and execute an overdamped brownian motion in a sinusoidal pinning potential, the one-dimensional equation of motion for one *single* vortex reads [74,75]

$$\eta \dot{x} + \partial_x U(x) = F_D(t) + F_T(t) \tag{2.61}$$

The first term is the viscous drag as defined in the Bardeen-Stephen theory [67] where $\eta = B\phi_0/(2\pi\xi_{nb}^2\rho_n)$. The second term represents the pinning of the vortices by the sinusoidal potential $U(x) = U_0(1 - cos(2\pi x/l_p))$ where l_p is the characteristic distance between two pinning centers. The driving force $F_D(t) = j_x(t)\phi_0$ due to the presence of a current $j_x(t)$ in the superconductor is the third term and the effect of thermal fluctuations is accounted for by the fourth term which is an uncorrelated stochastic thermal force satisfying $\langle F_T(t)F_T(0)\rangle_t = 2\eta k_B T\delta(t)$ where $\langle ...\rangle_t$ indicates averaging over time.
In the overdamped limit, the *ac* vortex mobility μ_v can be derived from Eq. (2.61) above and the sheet impedance $Z_s = \phi_0 B\mu_v$ reads [74,76]

$$R_s = R_{ff}\frac{I_0^{-2}(U_0/k_BT) + (\omega\tau)^2}{1 + (\omega\tau)^2} \tag{2.62}$$

$$L_s = R_{ff}\tau\frac{1 - I_0^{-2}(U_0/k_BT)}{1 + (\omega\tau)^2} \tag{2.63}$$

where I_n is a modified Bessel function of order n and τ a characteristic time for the relaxation of the vortices given by

$$\tau = \frac{\eta l_p^2}{4\pi^2 U_0}\frac{I_0^{-2}(U_0/k_BT) - 1}{I_0(U_0/k_BT)I_1(U_0/k_BT)} \tag{2.64}$$

In the limit where the pinning barrier U_0 is much larger than k_BT, the sheet resistance is proportional to e^{-2U_0/k_BT}, as expected for a pinned vortex liquid. When the barrier is much smaller than k_BT, the vortices can diffuse more easily and a flux flow regime appears (unpinned liquid). It is interesting to notice that, in the limit of low frequencies ($\omega\tau \ll 1$) and for low temperatures where the contribution from the Bessel function I_0 becomes exponentially small, the sheet resistance exhibits an ω^2 frequency dependence whereas the inductance is frequency independent [74].

3 Production and characterisation of the samples

The first section of this chapter is devoted to the general properties of the cuprate superconductors with an emphasis on the $Y_1Ba_2Cu_3O_{7-\delta}$ compound. In the second part of the chapter, we describe the deposition technique used to grow our layers. In the third part, we summarize the characteristics of the laser ablated films obtained by X-ray diffraction (XRD) and Atomic Force Microscopy (AFM).

3.1 The $Y_1Ba_2Cu_3O_{7-\delta}$ compound

Superconductivity in the $Y_1Ba_2Cu_3O_{7-\delta}$ compound [77] was spotted at the very beginning of the incredible outburst of passion generated by the discovery of superconductivity in the lanthanum based cuprate ($La_{2-x}Ba_xCuO_4$) by Bednorz and Müller in 1986 [1]. These two compounds were joined by other cuprates based on bismuth, thallium and mercury to form the family of the perovskite-type superconducting cuprates. All these compounds are characterized by a layered structure, a carrier density typically ten times lower than in copper and a very short coherence length ξ. Their crystallographic structures are typically tetragonal or orthorhombic and contain one, two or three CuO_2 planes perpendicular to the c axis which contain the charge carriers responsible for the electronic properties of the material. The fact that these charge carriers are localized in the CuO_2 planes explains the anisotropic properties of these compounds in both the normal and the superconducting state. Their relatively low carrier density increases the electromagnetic penetration depth λ. The very short coherence length found in the cuprates has basically two consequences. First, fluctuations of the order parameter will strongly affect the superconducting properties of these cuprates as discussed in section 2.1.1 of Chapter 2. Secondly, defects like oxygen vacancies, screw dislocations (SD) and grain boundaries will act as local normal regions perturbating the superconductivity more strongly than in conventional superconductors where the long-range coherence length helps smoothing the effects of crystalline disorder. We should finally notice that cuprate superconductors are very sensitive to carrier doping and often require non-stoichiometric compositions to ensure the superconducting phase to build up. The highest T_c value tends thus to correlate with an optimal doping, i.e. optimal density of charge carriers. Fig. 3.1 (left) shows the phase diagram of YBCO as a function of doping. The value of T_c appears also correlated with the number of copper-oxygen planes in the unit cell and is maximum for three CuO_2 planes in the bismuthates ($Bi_2Sr_2Ca_nCu_{n+1}O_{6+2n}$, $n = 0, 1$ or 2) and thallates ($Tl_2Ba_2Ca_nCu_{n+1}O_{6+2n}$).

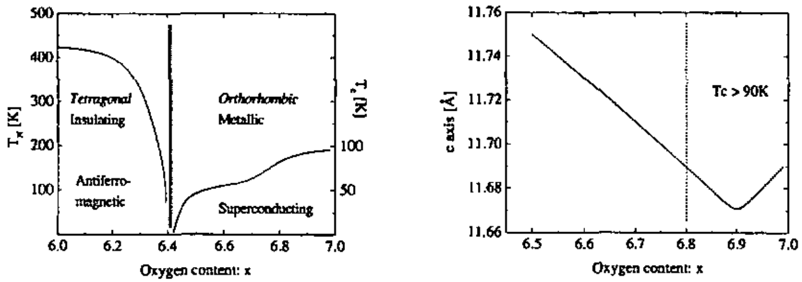

Figure 3.1: *Left: Sketch of the doping phase diagram for* $YBa_2Cu_3O_x$ *[78]. Right: c-axis parameter as a function of the oxygen content [79].*

3.1.1 Crystalline structure and general properties

The $Y_1Ba_2Cu_3O_x$ compound exhibits a tetragonal structure below an oxygen doping of $x = 6.4$ which transforms to orthorhombic as the oxygen doping is raised. In the former case, the oxygen atoms are randomly distributed in the basal plane of the structure whereas in the latter superconducting phase, the oxygen atoms order themselves to form $Cu-O$ chains directed along the b axis (see Fig. 3.2). This structural transformation distorts the unit cell by stretching the b axis relative to the a axis thus forming a rectangular basal plane. The CuO_2 planes straddling the Y plane are sandwiched between two planes containing Ba and O. A slight puckering of the CuO_2 planes appears as shown in Fig. 3.2. Finally, the basal and top planes consist of partially filled $-Cu-O-Cu-O-$ chains directed along the b axis. The chains are totally filled up when $x = 7$. The oxygen is thus the cause for the tetragonal to orthorhombic structural transition in the YBCO and the crystalline lattice parameters depend on the oxygen doping as shown in Fig. 3.1 (right). The optimum doping is reached at about $\delta = 0.1$ or $x = 6.9$ where we have $a = 3.818$, $b = 3.884$ and $c = 11.683$, see e.g. [80]. The structure of the Pr-substituted compound, $PrBa_2Cu_3O_7$ (PBCO), is very similar to that of YBCO. We notice that superconductivity occurs at typically $90K$ in many rare-earth (R) substituted $RBa_2Cu_3O_7$ compounds where R can be for instance Nd, Sm, Eu, Er or Dy [81]. It seems that superconductivity may appear in PBCO at about $80K$ under certain circumstances as observed by Z. Zou *et al.* [82]. However, this compound behaves as an insulator in our experimental conditions. We finally mention the existence of two other yttrium-based superconducting compounds, $YBa_2Cu_4O_8$ and $Y_2Ba_4Cu_7O_{15}$ which have a T_c between $80K$ and $90K$.

The yttrium and barium atoms appear to be basically completely ionized in their respective locations [28] with their remaining electrons bound in localized states thus having a negligible role in the electron dynamics. The electrical conduction properties depend

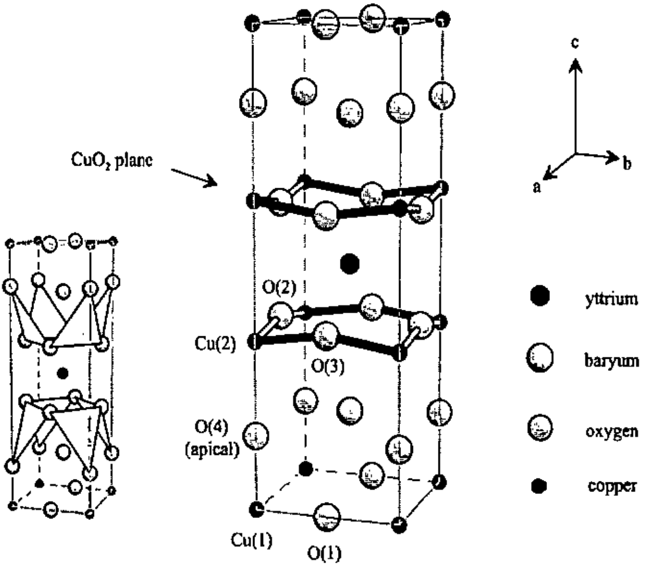

Figure 3.2: *Crystalline structure of the $Y_1Ba_2Cu_3O_7$ unit cell. The planes in the left smaller unit cell indicate the pyramidal coordination of the copper in the CuO_2 plane [28].*

principally on the electronic states of the Cu and O atoms within the planes and the chains. The hole carrier density is about $n \simeq 6 \cdot 10^{21} carriers/cm^3$ [83] which corresponds roughly to one carrier (one hole) per unit cell volume. Since oxygen doping of $YBa_2Cu_3O_6$ adds principally O atoms in the CuO chains whereas the oxygen content of the CuO_2 layers does not change usually, it appears that the chains have an essential effect on the electronic properties of the conducting CuO_2 planes. The chains can actually be seen as a charge (hole) reservoir for the CuO_2 planes. When the doping corresponds to one hole per unit cell, the compound is an antiferromagnetic insulator as depicted in Fig. 3.1. As the doping is raised, the antiferromagnetism disappears to be replaced by a superconducting state and the optimum T_c is reached when the mean number of holes per unit cell is about 1.15 [4]. This value of about one hole per unit cell can be deduced by roughly looking at the charge balance of the unit cell in the case $x = 7$ for instance. Assuming a 2+ oxidation state for the copper (see Table 3.1), the top CuO plane containing two chains is charge balanced as is the Barium plane BaO which contains one oxygen. The main charge unbalance comes thus from the block formed by the two CuO_2 planes and the insulating Y plane. This block counts the extra hole we are looking for since the yttrium is in the 3+ oxidation state. This reasoning is thus somewhat oversimplified since the valences of the copper atoms in the planes (Cu(2)) and in the chains (Cu(1)) depend on the doping as well as on the distances between the Cu(2) atoms and the O(2), O(3) and

O(4) oxygen atoms [84]. It is finally worthwhile mentioning that the curve describing the valence of the Cu(2) cations as a function of x [84] has roughly the same shape as T_c versus x meaning that it might be more appropriate to consider the effective hole number per unit cell rather than the oxygen content to understand the behavior of T_c in the particular case of YBCO.

Element	Y	Pr	Ba	Cu	O
Oxidation state	3+	3+	2+	2+	2-
Ionic radius [Å]	0.94	~ 1.04	1.34	0.72	1.32

Table 3.1: *Usual oxidation states and approximate ionic radii for the elements involved in the YBCO and PBCO compounds [28, 85].*

The presence of chains in the YBCO unit cell leads to a conductivity in the b direction about twice as large as the conductivity in the a direction for a twin-free YBCO single crystal. This effect will however not be relevant in our case since we cannot exclude the presence of twins in thin films. The relevant anisotropy will be for us the anisotropy $\gamma^2 = m_c/m_{ab}$ between the in-plane properties of YBCO and its properties along the c axis. The quantities m_{ab} and m_c are the effective masses of the carriers in the ab plane and along the c axis respectively. Slightly above T_c, we have $\rho_c/\rho_{ab} \approx 100$ [28]. Table 3.2 summarizes some of the relevant quantities for the YBCO compound.

Transition temperature	Anisotropy	Penetration depth	Coherence length	Critical field
$T_c \simeq 93K$	$5 \lesssim \gamma \lesssim 7$	$\lambda_{ab} \simeq 1400Å$	$\xi_{ab} \simeq 16Å$	$B_c(0) \simeq 1.04T$
		$\lambda_c \simeq 8400Å$	$\xi_c \simeq 3Å$	$B_{c1}(0) \simeq 38mT$
				$B_{c2}(0) \simeq 130T$

Table 3.2: *Parameters for bulk YBCO [21, 28].*

The resistivity along the ab plane ρ_{ab} exhibits a linear temperature dependence above T_c as would do a normal metal like copper where the temperature dependent part of ρ is due to the scattering of the charge carriers by the phonons[1]. The problem here is that in a normal metal, the carrier density does not vary with temperature whereas in the cuprates the carrier density varies not only with doping but also with temperature. At optimum doping, the carrier concentration depends linearly on the temperature which implies an unusual scattering rate proportional to T^2 [5].

---

[1] The resistivity of a metal can be approximated by $\rho = \rho_0 + \rho_{ph}(T)$ where ρ_0 is the temperature independent contribution from the impurities and other imperfections in the crystal structure and ρ_{ph} is the contribution from the phonons [28]. The temperature dependence of ρ_{ph} comes basically from the temperature dependence of the scattering rate of the electrons by the phonons. At high temperatures ($T \gg \Theta_D$), ρ is proportional to T whereas at low temperatures ($T \ll \Theta_D$), we have $\rho \propto T^5$ where Θ_D is the Debye temperature.

At the time, the understanding of the electronic properties of cuprates is still under debate and starts with the fundamental unsettled question of the exact mechanism which leads to the pairing of the electrons in the cuprates (see for instance [4,5] for reviews).

3.1.2 Thin films

Superconducting very thin films are usually sandwiched between layers of $PrBa_2Cu_3O_{7-\delta}$ or $Pr_xY_{1-x}Ba_2Cu_3O_{7-\delta}$ thus forming trilayers as will be described in the next section. The top and bottom PBCO layers act most probably as hole dopants for the YBCO layer [86]. The value of T_c in the films gradually decreases with decreasing thickness, most likely due to the enhanced effect of phase fluctuations of the superconducting order parameter in the layer.

Lower critical field and demagnetization factor We know that the Meissner state persists until the external applied field reaches the lower critical field B_{c1}. This is true for an infinite cylinder in a parallel magnetic field. For a less favorable geometry, one has to account for the geometry of the sample via the demagnetization factor N. For very flat samples, the lower critical field will be strongly reduced and the effective lower critical field B'_{c1} can be expressed by the equation $B'_{c1} = (1 - N)B_{c1}$. For a thin circular film of radius w and thickness d, the demagnetization factor for a field applied perpendicular to its surface is given by $1 - N \approx \pi/4 \cdot d/w$ (see e.g. Ref. 28, p342). If we use this expression to obtain a rough estimate of $1 - N$ for our thicker films ($w = 1cm$ and $d \approx 1000$Å), we get $1 - N \approx 8 \cdot 10^{-6}$. This gives a lower critical field $B'_{c1} \approx 3 \cdot 10^{-7}T$ instead of $B_{c1} \approx 38mT$ for bulk YBCO (see Table 3.2 above). This means that the earth magnetic field ($\approx 5 \cdot 10^{-5}T$) is strong enough to bring the sample into the mixed state. An estimate of the demagnetization factor for a square thin film based on the expression used by Fiory *et al.* [87] yields an even smaller value: $1 - N \approx 8 \cdot 10^{-10}$.

3.2 Pulsed laser deposition of $Y_1Ba_2Cu_3O_{7-\delta}$ thin films

We used a conventional laser ablation technique to grow our YBCO layers [88]. The method consists in sending a short laser pulse on a target of $YBa_2Cu_3O_x$. The energy of the pulse is absorbed by the target surface which first melts locally and is then evaporated in the form of a highly-forward directed stoichiometric plasma plume. The evaporated material is collected on a substrate heated at the appropriate temperature. Since no discharges are involved in this technique, the deposition process can be carried out in an oxygen environment which is required for our ceramics. This technique allows a good film-to-film reproducibility, an accurate stoichiometry transfer from the target to the substrate and single-phase c-axis oriented films can be relatively easily produced. The good physical properties (sharp and high transition temperatures) shown by the samples render this technique well suited for our needs. It is however clear that the choice of the substrate, the deposition temperature, the ablation energy and other similar parameters will have to be carefully adjusted before an optimal film quality can be reached.

Terraces and screw dislocations [89, 90] appearing in the films are a consequence of the growth mechanism of these pulsed-laser ablated films. As the thickness of the layer increases, its surface roughness will increase as well. The formation of precipitates [91,92] appearing at the surface of the layer is another particularity of this technique. Those precipitates may exhibit various forms (droplets, needles) and composition (CuO, Y_2O_3, ...). They may condense during the expansion of the plasma plume or may be directly grabbed away from the target during the impact of the laser pulse.

3.2.1 Description of the system

The light source that we use is a KrF Excimer laser supplying pulses with a maximum energy of about $650mJ$ and typical duration smaller than $25ns$ at a wavelength of $248nm$. The purity of the gas mixture is improved by a liquid nitrogen cold trap. The laser beam is first diaphragmed in order to select a beam area where the light amplitude is homogeneously distributed. The light is then focused by a $300mm$ lens through an anti-reflection coated window onto the target in the vacuum chamber. Twelve different targets are mounted on a rotating drum which allows to grow alloys or multilayers involving various compounds. The targets are pressed ceramic disks which are glued with silverpaste onto rotating copper holders. A periodical polishing of the surface of the targets will avoid the formation of holes which alter the shape of the plasma plume.

Substrate and buffer layer Among the different substrates [93, 94] currently used for the growth of YBCO films (see Table 3.3), we have chosen monocrystalline (100) oriented $SrTiO_3$ (STO) substrates. These substrates are well lattice-matched to the YBCO ceramic thus favouring epitaxial growth. The other advantage relies on the values of the linear thermal expansion coefficient α_{th} of both STO and YBCO which are close to each other. This last parameter is important to avoid thermally induced strain or microcracks in the layer that may arise due to the large temperature gradients undergone by the sample: above $1000K$ during the deposition down to $4.2K$ during the measurements. The STO substrates have a large dielectric constant (see for example [95]) which may cause some trouble for radio-frequency applications at low temperatures due to ac dielectric losses. The dimensions of the substrates are $10mm$ x $10mm$ x $0.5mm$ and their crystallographic misorientation is expected to be smaller than 0.5°. The parallelness of the surfaces is better than 2% and the surface roughness is of the order of $1nm$ as observed by AFM (see Ref. [96] and Fig. 3.13 on page 52).
The mismatch between the unit cell of YBCO and the STO substrate is expected to cause an expansion of the YBCO unit cell along the a and b axis while it will be slightly compressed along the c axis. These effects are expected to change the value of the transition temperature. However, in the case of YBCO, an expansion of the unit cell along the a axis results in a decrease of T_c whereas an expansion along the b axis will produce an increase of T_c with $dT_c/dp_a \sim -2.0K/GPa$ and $dT_c/dp_b \sim +1.9K/GPa$ [97]. The two variations

Material	$YBa_2Cu_3O_7$ (orthorhombic)	$PrBa_2Cu_3O_7$ (orthorhombic)	$SrTiO_3$ (cubic)	MgO (cubic)	$LaAlO_3$ (cubic)	Si (diamond)
crystalline parameters [Å]	$a = 3.82$ $b = 3.89$ $c = 11.68$	$a = 3.90$ $b = 3.92$ $c = 11.71$	$a = 3.91$	$a = 4.21$	$a = 3.78$	$a = 5.43$
mismatch [%]		1.4	1.4	9.2	1.9	
α_{th} $[10^{-5} \cdot K^{-1}]$	0.85-1.3		0.94-1.0	0.85-1.1	1.0	0.38
ϵ_r	3.7		300	9.6	16	12

Table 3.3: *Properties of the grown compounds and of common substrates at* $300K$. *We give the crystalline parameters, the misfit to* $(a+b)/2$ *of YBCO, the linear thermal expansion coefficient* α_{th} *and the dielectric constant* ϵ_r *(1kHz). From Refs. 85, 94.*

will thus roughly compensate. Along the c axis, we have $dT_c/dp_c \sim 0.3K/GPa$ and the effect is much weaker. Furthermore, the elastic strain in the layer will be accommodated by the formation of misfit (screw and edge) dislocations above a critical thickness of typically 100Å to 200Å [92, 98]. For thin films however, the effect of the mismatch between the substrate and the film may still affect the value of T_c. We thus grow a buffer layer of (PBCO) prior to the YBCO deposition which has proven to be very useful for ultra-thin film growth [86, 99, 100]. Finally, we usually cover the YBCO film with a PBCO layer typically 8 unit cells (u.c.) thick, which has the function to prevent oxygen diffusion out of the film. This was done systematically for the films with thicknesses below 100Å.

The case of silicium among the substrates is particular since the growth of YBCO layers on Si substrates appears very attractive for industrial applications but encounters various problems. The thermal expansion coefficient of Si is three to four times smaller than the one of YBCO leading to strong thermally induced strain in the layer. Another problem arises from the interdiffusion of Si in the YBCO layer. A buffer layer appears necessary and good results were obtained with yttrium stabilized zirconate (YSZ, ~ 9% of Y) ablated from $(Y_2O_3)_{0.09}(ZrO_2)_{0.91}$ polycrystalline targets [101].

Substrate mounting The sample holder is a stainless steel plate clamped between two copper blocks which are connected to a water cooled electrical feedthrough. The sample is mounted at the center of the plate and fixed by two thin stainless steel sheets screwed to the sample holder. A thermocouple is placed below the sample and is kept in position by an stainless steel plate which is screwed together with the sheets holding the sample. Between the sample holder and the substrate, we insert a thin Ag sheet which will ensure a good thermal contact between the substrate and the sample holder and improve the homogeneity of the substrate temperature. The distance between the substrate and the surface of the target is typically $45mm$. The position of the sample holder is carefully adjusted in order to be well centered in the plume which is crucial to avoid thickness gradients in the film.

Deposition and growth mechanism Once the substrate is cleaned and mounted on the sample holder, we evacuate the deposition chamber down to about $10^{-5}mbar$ and clean the targets after having masked the substrate. The substrate is then heated to the deposition temperature close to $760°C$ and kept at this level during typically one hour to properly outgas the chamber and the substrate. This also allows to evaporate a thin Ag layer on the background of the substrate which favours the thermal contact between the sample holder and the substrate. After that, we admit molecular oxygen in the chamber up to a pressure of about $0.2mbar$. When the temperature is correctly stabilized, we start to fire the laser on the desired targets at typically two pulses per second. During the deposition process, the energy of the laser beam is limited to about $100mJ/pulse$ in the vacuum chamber as measured with a pyroelectric detector. The size of the spot on the target extends to about $10mm^2$ which results in a typical laser fluence of $1J/(pulse \cdot cm^2)$. The temperature homogeneity of the sample is controlled during the deposition process with an optical pyrometer.

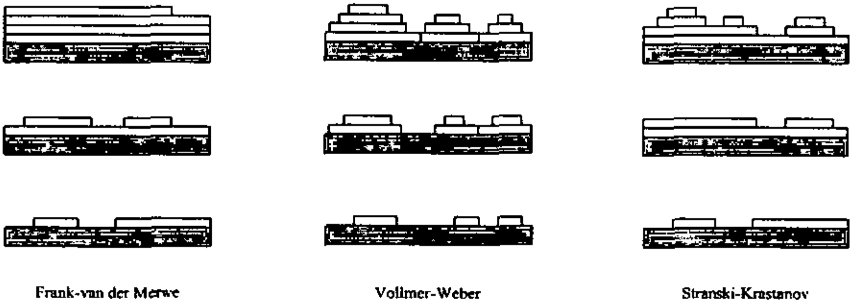

Figure 3.3: *Sketch of the basic epitactic growth forms. Left: layer-by-layer growth; center: island growth; and right: layer-by-layer growth followed by islands nucleation and growth.*

The superconducting properties of the films will be very sensitive to the microstructure resulting from the growth mechanism due to their very short coherence length. The type and amount of defects as well as the surface roughness play here a crucial role. The different forms of epitactic growth depend on the strain energy in the layer and the bonding between the depositing species (called adatoms) and the substrate. Fig. 3.3 illustrates the epitactic growth modes which are basically [98, 102]: layer-by-layer growth (Frank-van der Merwe), island growth (Vollmer-Weber) and initial layer growth followed by island nucleation (Stranski-Krastanov). Layer-by-layer growth means that the major part of one growth layer is completed before the next layer is nucleated (2D growth). This will only occur if the interaction between the film atoms and the substrate atoms is very strong. If the misfit between the substrate and the layer is non-zero, the layer-by-layer growth will take place up to a limited thickness determined by the build-up of strain in

the layer. Dislocations will then appear and an island growth mode will take place. When the interaction between the substrate atoms and the layer atoms is not very strong, the species arriving at the surface of the substrate will form small clusters which will then grow laterally and vertically (3D growth).
Depositing films with thicknesses less than 100Å is clearly somewhat tricky due to surface roughness and film connectivity problems. We thus expect percolation effects to appear in these films and we will see in Chapter 5 that we may quantify these effects from the value of the penetration depth extracted from the inductive measurements of the layers.

Sintering After the deposition is completed, the temperature is decreased to $500K$ in about ten minutes while the oxygen pressure is raised to $1bar$. The sample is then sintered at $500K$ during fifteen minutes before the temperature is finally decreased to room temperature in twenty-five minutes. This step of the deposition process is crucial since, during this time, the film undergoes the structural phase transition bringing it from the insulating tetragonal structure to the superconducting orthorhombic structure (see Fig. 3.4, left). This phase transition is driven by the oxygen which diffuses in the film and forces its structure to become orthorhombic above $x = 6.5$. The oxygen diffusion takes place mainly along the defects of the film and the presence of twins or dislocations in the layer will greatly reduce the time necessary for the oxygen to diffuse through the entire sample thickness. Since the oxygen diffuses more rapidly in the ab plane than along the c axis (Fig. 3.4, right), the presence of terrasses will help to decrease the sintering time of our layers. We summarize the main deposition parameters of some selected films in Table 3.4.

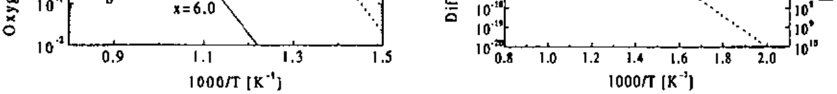

Figure 3.4: *Left: Oxygen partial pressure versus growth temperature for $YBa_2Cu_3O_x$ and tetragonal-orthorhombic transition line at $x \sim 6.5$, see [103, 104] for a more detailed phase diagram. Right: Oxygen diffusion constant as a function of sintering temperature for in-plane (D_{ab}) and out-of-plane (D_c) diffusion [105, 106]. The time $t = d^2/D$ necessary to oxidize a $d = 1000Å$ thick film is shown on the right axis of the plot.*

Sample	S618	**S607**	S612	**S610**	S604	S606	**S269**	S609	S615	**S472**
r	1.35	1.35	1.35	1.35	1.35	1.35	~ 2.0	1.35	1.35	1.1
d	15	24	24	47	47	93	~ 400	980	980	1100
n	~ 1	2	2	4	4	8	~ 34	84	84	94
b	140	210	210	470	470	470	-	-	-	-
t	93	93	93	93	93	93	-	-	-	-
d_t	250	330	330	610	610	660	~ 400	980	980	1100

Table 3.4: *In this table we give the deposition rate r [Å/pulse], the thickness d [Å] of the YBCO layer, the number n of YBCO unit cells, the thickness b [Å] of the PBCO buffer layer, the thickness t [Å] of the PBCO top layer and the total thickness d_t [Å] of the film for ten selected films. The name of the films which were systematically measured are bold face.*

3.3 Characterisation of the films

In this section, we summarize the informations that we could gather on our films from X-ray diffraction, atomic force microscopy and resistivity measurements.

3.3.1 X-ray analysis

After having grown a film, we directly probe its cristalline structure by means of X-ray diffraction (Philips PW3020 diffractometer in the Bragg-Brentano configuration), see Fig. 3.5. The X-ray copper tube is operated at a tension of 30kV for a heating current of the filament of $20mA$. The X-ray beam is not monochromatic and comprises basically the three copper lines: $k\alpha_1, k\alpha_2$ and $k\beta$ with respectively $\lambda_{k\alpha_1} = 1.5405$Å, $\lambda_{k\alpha_2} = 1.5443$Å and $\lambda_{k\beta} = 1.3922$Å. A Ni filter mounted at the tube shield exit allows to attenuate the contribution from the β-line. We will thus use the mean value $\lambda_x = (2\lambda_{k\alpha_1} + \lambda_{k\alpha_2})/3$ for the wavelength of the X-rays since the intensity of the $k\alpha_1$ contribution is about twice the intensity of the $k\alpha_2$ contribution. It is however clear that, in order to know precisely the value of a diffraction peak, it would be necessary to deconvolute the peak into the two contributions of the $k\alpha_1$ and $k\alpha_2$ lines using for example the Rachinger algorithm [107]. Another point which we should keep in mind is that the geometrical properties of the diffractometer will introduce aberrations into the pure diffraction profile rendering it asymmetrical and causing a broadening of the peaks and a displacement of their centers [107]. This basically means that working with experimental peak profiles whithout unfolding the pure line profile will not allow accurate determinations of the interlayer spacing d_l or of the effective thickness d_{eff} of a layer [107] but will still allow a comparison of these quantities obtained from different films by the same procedure.

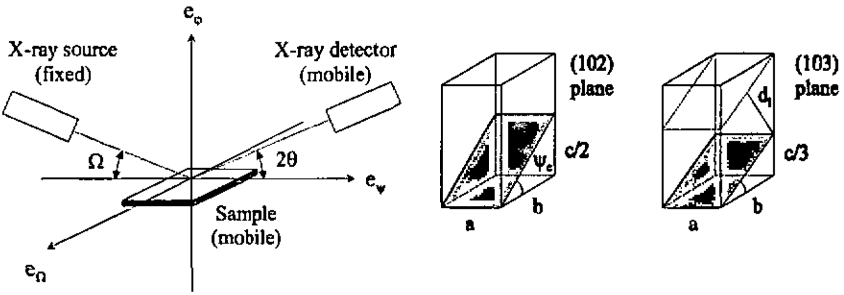

Figure 3.5: *Left: Geometry of the X-ray diffractometer. Right: (102) and (103) planes in the YBCO unit cell.*

Scans

A typical $\theta - 2\theta$ scan is shown in Fig. 3.6 where the different peaks are identified. The peak position yields the distance d_l between two adjacent diffracting planes by using the Bragg relation

$$2d_l sin(\theta) = n\lambda_x \tag{3.1}$$

for each value of 2θ. However, the peaks are affected by the aberrations mentioned above and a better way to obtain the value of d_l consists in plotting the value of d_l deduced for each diffraction peak as a function of a power of a trigonometric function of theta (typically $tan(\theta)$) since the main aberrations can be expressed in terms of a power of $tan(\theta)$ [107]. The plot should be linear and the value of d_l is given by the ordinate intercept of the curve where $tan(\theta) = 0$. From the behavior of the bare substrate diffraction peaks, it appears that a $tan(\theta)^{-2}$ dependence is suited for our diffractometer whereas behaviors following $tan(\theta)^{-1} \cdot cos(\theta)$ are possible in other cases. We obtain a lattice parameter of 3.9054Å for the substrate in good agreement with the expected value of 3.905Å. We used only the higher order peaks to deduce the value of d_l ignoring the (003),(006) and (009) diffraction peaks from the films scans since their shape might be slighltly affected by the substrate (100), (200) and (300) diffraction peaks. In our case, $d_l = c$ and we obtain an estimate of the c-axis parameter of our layers. We notice in Table 3.5 that we obtain c-axis values greater than the bulk value of 11.68Å which is peculiar since we would rather expect a value smaller than the bulk value as stated in Sec. 3.2.1. Such 'large' values were previously observed in our institute and have also been reported in Ref. 108 where $d_l \gtrsim 11.70$Å was found for YBCO thin films. It is still unclear at this point whether these observations do really tell something about some peculiar behavior of the YBCO unit cell in the layers or whether this effect is just an artifact without physical meaning. However, we have to be aware that, for the thin layers, this value of d_l represents essentially the value of the c axis for the PBCO compound due to the presence of the PBCO buffer layer. Since both c-axis values are slightly different for the two compounds, the value of d_t remains somewhat qualitative.

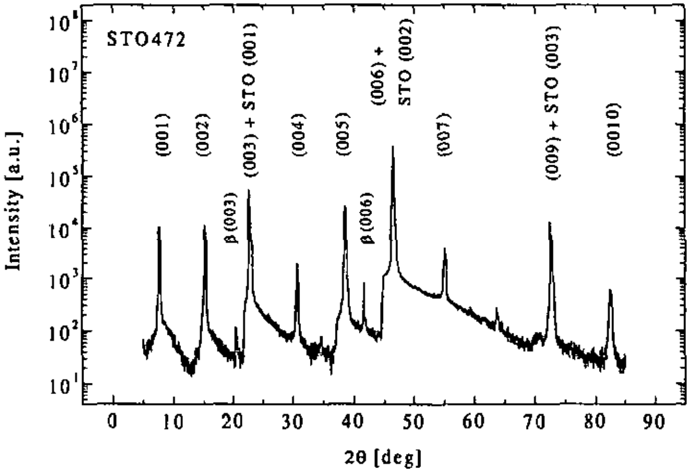

Figure 3.6: *θ-2θ scan of sample STO472.*

The pole figures (off-axis scans) probe the texture of the layers. They allow to check the c-axis epitaxy and reveal the presence of phases with different orientations (a axis or c axis). We have chosen two family of reticular planes, (102) and (103), for which the Bragg condition is fullfiled for $2\theta = 27.88°$ and $2\theta = 32.81°$ respectively. The peaks in the pole figures around the axis defined by the (103) plane have a greater intensity which is useful for samples with very low thicknesses. These scans provide four peaks (see Fig. 3.7) when the sample is correctly c-axis oriented at approximately the same ψ values for each peak since our experimental resolution does not allow to differentiate between the peaks due to the $(10l)$ and $(01l)$ planes (the values for ψ_c are 56.33° (102), 56.81° (012) and 45.02° (103) and 45.54° (013), see Fig. 3.5, right). We can obtain a rough estimate of the mean value for the in plane lattice parameter of the film $a_m = (a+b)/2$ using the expression $tan(\psi_c) = (c/x)/a_m$ for a pole figure of axis $(10l)$.

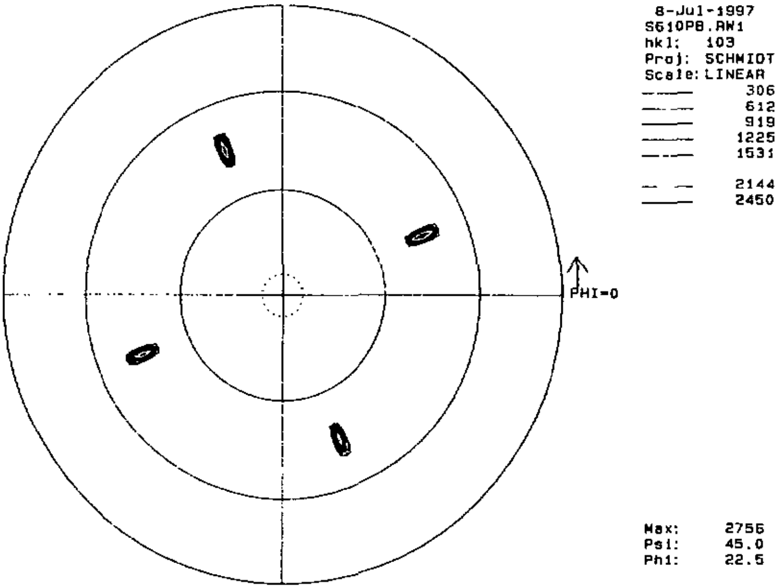

Figure 3.7: *Pole figure of sample STO610 around the axis perpendicular to the* (103) *plane.*

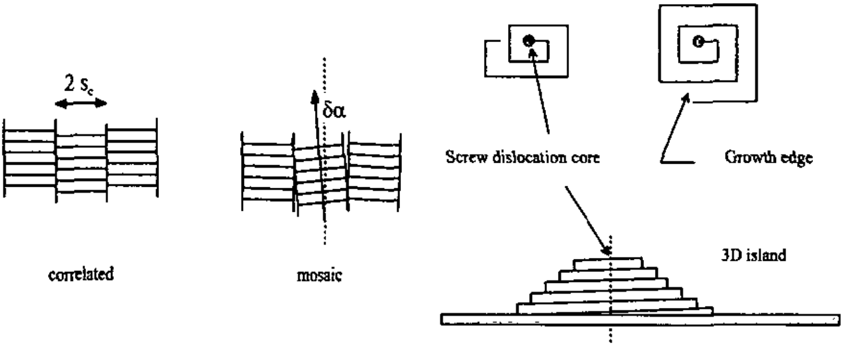

Figure 3.8: *Left: Illustration of the disorder correlation in a layer. Right: Sketch of 3D growth spirals or pyramids exhibiting a single screw dislocation in their center.*

The presence of stacking faults, limiting the lateral coherence of the layer, will decrease the intensity of the peaks in the pole figure. The nature of these faults, or more generally, the nature of the crystal disorder in the layer, can be better probed by rocking curves (Ω scans). For this type of scan, the 2θ angle value is fixed while the Ω angle is varied in the range $[\theta - \alpha; \theta + \alpha]$ where α is typically 1°. It is interesting to examine the shape of the diffraction peak for such scans.

If the diffracting planes extend up to a typical distance s_c (see Fig. 3.8), then the rocking curve is expected to present a Lorentzian profile [108]. A nice example of such a profile is shown in Fig. 3.9 (left) where we plot a rocking curve measured for the (005) YBCO reflection of sample STO606. When the disorder in the layer is due to a random mosaic structure (granular disorder) as shown in Fig. 3.8, the statistical distribution for the (small) angles $\delta\alpha$ is uncorrelated in space (typically $\propto e^{(-\delta\alpha/\alpha_0)^2}$) and the peak is expected to follow a Gaussian profile [109,110]. What we observe most commonly is an intermediate profile as illustrated by the (005) YBCO peak of sample STO607 (Fig. 3.9, right). A pure Gaussian profile would indicate a strongly disordered film whose pole figure is poorly contrasted (low intensity and broadened peaks). To be fully reliable, however, this type of analysis should rather be performed on corrected scans accounting for the modified shape of the peaks due to the presence of aberrations.

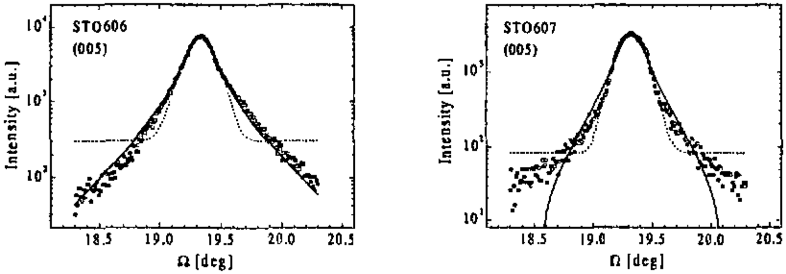

Figure 3.9: *Lorentzian (solid line) and Gaussian (dotted line) fits to rocking curves for two samples. Left: STO606, 8 u.c. Right: STO607, 2 u.c.*

Deposition rate

The calibration of the deposition rate for the two compounds we deposited was deduced from the satellite peaks showing up for multilayers grown by alternating the two materials. The period of the multilayer Λ is deduced from Bragg's law and reads

$$\Lambda = \frac{(m-n) \cdot \lambda_x}{2(sin(\theta_m) - sin(\theta_n))} \tag{3.2}$$

where m and n denote the diffraction order of the satellite peaks (Fig. 3.10). By growing at least two multilayers with different sequences, we can deduce the deposition rate for each compound. For the last series of samples we grew (#600 and larger), we had rates of 1.35Å/pulse for YBCO and 1.55Å/pulse for PBCO.

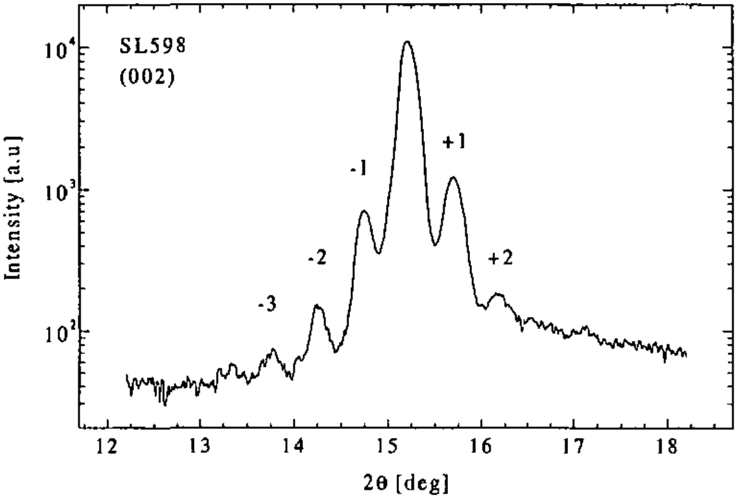

Figure 3.10: *Satellite peaks observed around the (002) YBCO reflection for the multilayer SL598 (9 x (48Å PBCO + 84Å YBCO)) + 48Å PBCO).*

3.3.2 Atomic force microscope characterization

The study of our layers by means of Atomic Force Microscopy (AFM or SPM) performed at the University of Bern (electrochemistry group, Prof. H. Siegenthaler), with the help of Dr. A. Daridon, gave us an insight into the microstructure of our layers.

Since the lattice match of YBCO to STO is relatively good (strong substrate-adatoms interaction), screw dislocations are expected to appear only after several unit cells, once the strain in the film has build up enough. Screw dislocations may however appear more rapidly if the miscut between the layer and the substrate is non-zero. Moreover, additional screw dislocations as well as stacking faults will be generated upon islands coalescence or meeting of two separate growth fronts having a vertical offset or inclined surfaces. On the other hand, the density of screw dislocations will decrease as the growth temperature of the film is raised since the microstructure will relax towards a thermodynamically more favorable flat surface. A decrease by a factor of three in the density of screw dislocations has been reported between substrate growth temperatures of 750°C and 780°C [102,111]. Fig. 3.12 shows AFM scans on samples STO574 and STO575, about 1300Å thick, revealing a very rough structure where terraces, holes and precipitates appear. By varying the deposition parameters, we could decrease slightly the surface roughness[2] of the thick samples as well as the density of spirals as shown by the scans of sample STO615 (Fig. 3.13). The surface roughness reaches here about 160Å although sample STO615 is still about 1000Å thick whereas we had roughnesses of 500Å and 600Å for samples STO574 and STO575. The surface roughness of the scanned films is shown in Fig. 3.11 (left). These values are obtained from the $10\mu m x 10\mu m$ images which are the largest scans we performed. The roughness of the substrate as received from the manufacturer was about $1nm$. We noticed that the number of outgrowths in STO574 was smaller by a factor of about four as compared to STO575, which may be attributed to the shorter distance between the sample and the target for STO574. This last point would favor the picture that precipitates form in the plume during the time of flight from the target to the substrate and are not only directly grabbed away from the target. It is however important to notice that the oxygen partial pressure will play some role in this process. In particular, oxides will form more easily if the oxygen partial pressure is too high, see for instance [113].

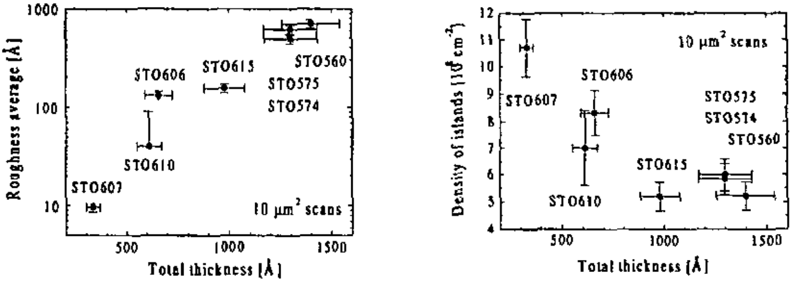

Figure 3.11: *Left: Roughness of the surface obtained from $10\mu m x 10\mu m$ scans. The value for sample STO610 is spoilt by an increased uncertainty due to the presence of a huge precipitate in the scan area. Right: Density of growth islands .*

From these images, it appears that for thick (typically 1000Å or more) films deposited directly on the STO substrate, we have a strongly marked screw dislocation mediated island growth mechanism. The screw dislocations lead to the formation of spiral islands

---

[2] We refer here to the roughness average S_a defined as $S_a = \frac{1}{m \cdot n} \sum_{k=0}^{m-1} \sum_{k=0}^{n-1} |z(x_k, y_k)|$ where n and m are the number of pixels in each direction of the scan, see J. F. Jorgensen [112] and references therein.

or pyramids in the sample. An example of such a spiral with a screw dislocation in its center observed in sample STO575 is shown in Fig. 3.14. The density of growth spirals due to screw dislocations in our thick films as observed in the $10\mu m x 10\mu m$ images reaches typically $5 \cdot 10^8 cm^{-2}$ in agreement with previous works [102,111]. As the thickness decreases, we can observe in Fig. 3.11 (right) a slight increase in the density of islands which is reasonable since the very thin films represent the early stage of the film growth and the initial coalescence of the islands. The density of islands was taken as the number of local maxima in the whole area of the scan. For the thinner films grown on PBCO buffer layers, growth islands are still present but the spirals have almost completely disappeared and the surface is much smoother (Fig. 3.14, right). The presence of the buffer layer allows to delay the apparition of dislocations in the layer. The scan of sample STO607 shows a growth island where the a and b crystalline directions appear nicely, although indistinguishable.

An estimate of the typical length scale of the surface modulation (roughness) may be an indication of the characteristic pinning length scale l_p in our films. If we simply attribute a surface πr_i^2 to each island and deduce the value for r_i from the density of islands in our films, we obtain typically $0.17\mu m \lesssim r_i \lesssim 0.25\mu m$.

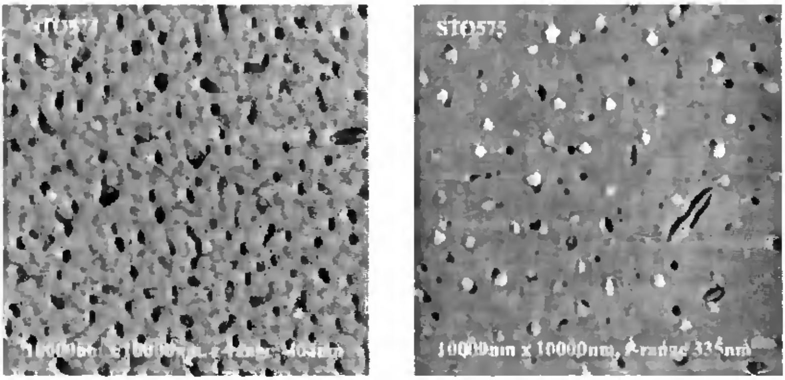

Figure 3.12: *Left: STO574. Right: STO575*

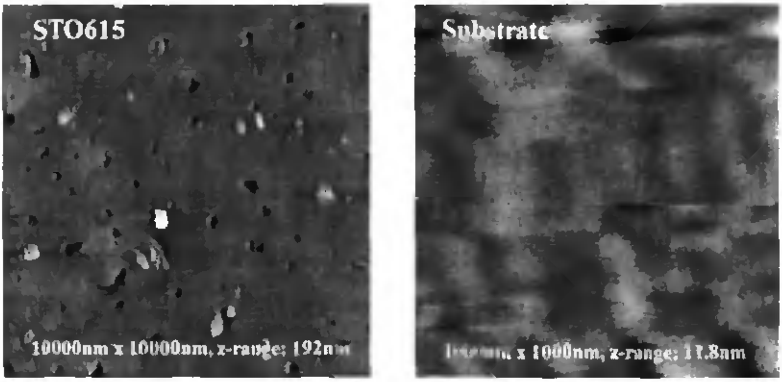

Figure 3.13: *Left: STO615. Right: STO substrate.*

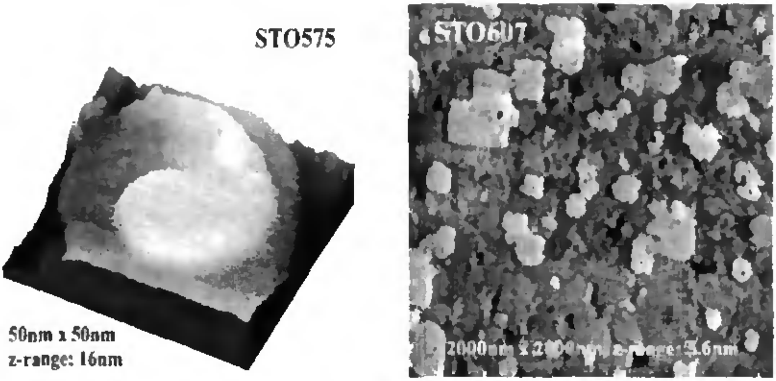

Figure 3.14: *Left: detail of a growth spiral in STO575. Right: STO607.*

3.3.3 Resistive measurements

To avoid a possible damaging to the surface of the sample, the measurements of the resistivity were carried after having completed the measurements with the inductive system. Unfortunately, sample STO472 broke during the last thermal cycle and could thus not be measured resistively. Nevertheless, the measurement of sample STO615 provides a typical curve for thick samples where $d \sim 1000$Å. The resistivity at $100K$ of sample STO269 was $330\mu\Omega cm$ as measured by a standard four probe technique where the resistivity is given by

$$\rho = \frac{\pi d}{ln(2)} \frac{R_{AB,CD} + R_{BC,DA}}{2} f_{corr} \left(\frac{R_{AB,CD}}{R_{BC,DA}} \right) \tag{3.3}$$

The correction factor f_{corr} [114] depends on the ratio of the measured resistances and the geometry is sketched in Fig. 3.15 (left). The resistive measurements on samples STO607, STO610 and STO615 were performed using the geometry shown in Fig. 3.15 (right). The contacts were made with indium wires ($0.3mm$ diameter) pressed on the sample and the current was $I = 0.1mA$. For this geometry, the resistivity reads

$$\rho = \frac{U}{I} \frac{dw}{l} \tag{3.4}$$

where l is the distance between the voltage probes and d the thickness of the sample. The length of the voltage probes corresponds to the width w of the sample.
In the figure inserted on the right, we describe how the values T_{c0}, T_N and T_{cu} are deduced from the resistivity curve. T_{c0} is the intercept of the highest slope line along the transition with the axis $y = 0$. T_N is roughly the onset temperature where the resistivity curve deviates from the linear behavior above the transition. And finally, T_{cu} is the temperature at which both linear fits cross. The width of the transition ΔT is taken as the difference $T_{cu} - T_{c0}$. We obtain T_{c0} values in agreement with the values reported in the literature, see for instance Refs. 115,116.

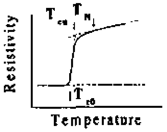

Figure 3.15: *Geometries used for the resistive measurements.*

For an optimal oxygen doping, we expect a linear temperature dependence of the resistivity in the normal state for the YBCO compound up to $300K$. For an underdoped (overdoped) sample, the resistivity curve will depart from the linear behavior and bend upwards (downwards), see for example [117]. In Fig. 3.16 (right), we can observe a slight upwards curvature for the resistivity curve of sample STO615 revealing a weak underdoping of the sample which may depress the transition temperature. Despite the PBCO top layer, the resistivity of samples STO607 and STO610 goes to zero (Fig. 3.16, left). We thus assume that the curves are still representative of the properties of the YBCO layer and extract T_{c0} and ρ_n as described above. A summary of the numerical values for the quantities defined here can be found in Table 3.5 on page 56.

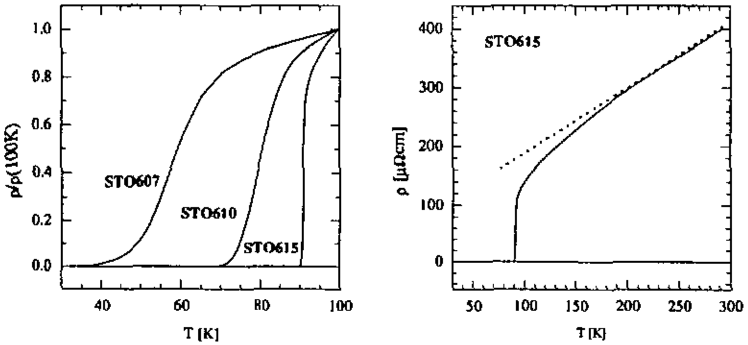

Figure 3.16: *Normalized resistivity of STO607, STO610 and STO615 (left) as a function of temperature. The straight dotted line in STO615 plot (right) emphasizes the bending of the curve which reveals a slight underdoping in oxygen.*

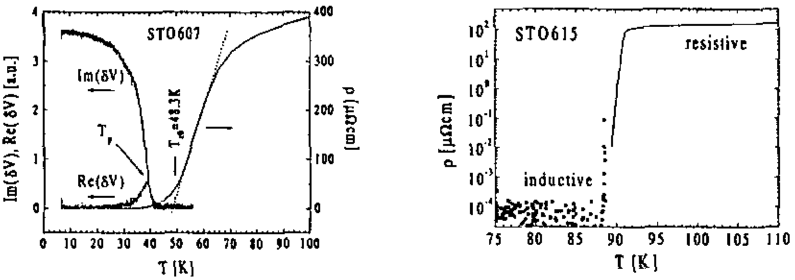

Figure 3.17: *Left: Inductive (1kHz) and resistive transitions for sample STO607. The temperature of the peak in $Re(\delta V)$ is referred to as T_p. Right: comparison of the resistivity as measured with the inductive and the resistive method for sample STO615.*

3.3.4 Inductive measurements and comparison to resistivity curves

A good way to determine the existence of coarse-grained domains in a sample is to perform an inductive measurement of its superconducting transition. A sample containing large domains weakly connected will usually exhibit shoulders in its inductive transition since the domains become superconducting at different temperatures. The inductive technique has proven to be very sensitive to such problems [118] and constitutes thus our final test to decide whether a sample will be systematically measured or not. The inductive curves $Im(\delta V)$ and $Re(\delta V)$ for sample STO607 are shown in Fig. 3.17, as well as the resistive measurement. We also show the resistivity of sample STO615 as obtained from the inductive and the resistive methods. We observe a temperature shift of about $0.5K$ which is included in the tolerance of the temperature sensors used. The inductive transitions are clean and confirm the reliability of these films. We may suspect weak percolation effects in the 2 u.c. film due to the slight break appearing in the imaginary part of the signal δV at $T \simeq 28K$. We will see in Sec. 5.2.1 that percolation effects increase as the thickness of the sample decreases.

Finally, we report in Fig. 3.18 the values for the temperature T_p of the peak in $Re(\delta V)$ as a function of the thickness for some samples.

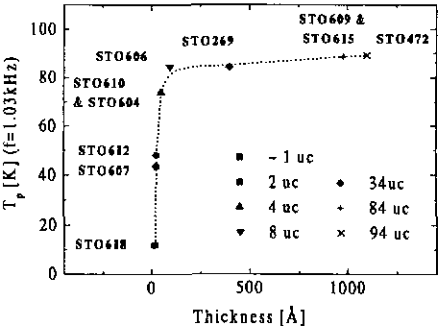

Figure 3.18: *Thickness dependence of T_p at $f = 1.03kHz$ for the samples of Table 3.4 on page 44. The dotted line is a guide to the eye.*

3.4 Summary

Table 3.5 summarizes the main physical parameters of the films we measured systematically. Sample STO615 is added to complete the lacunar informations for sample STO472. We report the approximate values for the height c of the unit cell. The values for samples STO607 and STO610 are due to both the YBCO and the PBCO contributions because of the presence of the PBCO buffer layer. The values for the transition temperature T_{c0}, the transition width ΔT, the normal state resistivity ρ_N and the resistivity ρ_{100K} are obtained from the resistive measurements. We finally indicate the temperature of the peak in $Re(\delta V)$ at $f = 1.03kHz$ obtained from the inductive measurements in the absence of magnetic field as well as its width at half maximum ΔT_p.

Name	# u.c.	c [Å]	a_m [Å]	T_{c0} $[K]$	ΔT $[K]$	T_p $[K]$	ΔT_p $[K]$	ρ_N $[\mu\Omega cm]$	$\rho(100K)$ $[\mu\Omega cm]$
STO472	94	11.69	3.99	$\simeq 91^a$	-	89.04	0.2	-	-
STO615	84	11.69	3.92	90.4	1.1	88.5	< 0.1	150	140
STO269	~ 26	11.67	3.88	89.1	~ 1.2	84.2	0.4	-	330
STO610	4	11.68	3.88	73.7	11.9	69.4	1.7	265	280
STO607	2	11.68	3.88	48.3	18.8	38.5	4.5	350	390

Table 3.5: *Summary of the main parameters measured for selected samples (see text).* [a] *The value for this sample is an estimate based on the value for sample STO615.*

4 Cryostat and measuring technique

In this chapter, we describe the experimental setup which was developed to perform the measurements presented in this work. The cryostat comprises a commercial ^4He dewar which can contain up to 30 liters of liquid helium allowing an autonomy of about 60 hours in its current configuration. The main insert dips directly in the ^4He bath and holds a stainless steel pot where a superconducting coil is wounded as illustrated in Fig. 4.1. We will first discuss the problems of temperature control and magnetic field. The measuring method is then presented in Sec. 4.2 and further details concerning the cryostat and the measurement system can be found in appendix A.

4.1 Cryostat

The main insert of the cryostat has evolved from its original design during this work. After measuring the first film (STO269) with the original setup [119–121], we reduced the mass of the sample holder and improved the contact with the cold source. The thermal inertia of the system could thus be lowered to measure sample STO472. A final modification made it possible to extend the temperature ramps down to $4.2K$ which was necessary to measure the thinner samples STO610 [122] and STO607. During a measurement, the pot is evacuated down to $10^{-5}mb$ and works as an inner vacuum chamber. A thin-wall stainless steel tube connected to the ^4He bath through an impedance separates the vacuum chamber from the sample chamber. The thermal homogeneity in the sample chamber is ensured by the presence of ^4He gas admitted through the impedance. The temperature of the gas admitted in the sample chamber is measured by a diode thermometer and can be adjusted if necessary .

The sample is placed on a sapphire cylinder bearing a heater and comprising a carbon-glass resistor (CGR) which remains reliable in the presence of a magnetic field. The sapphire cylinder is pressed against the Stycast matrix embodying the coils system through two nickel-brass screws. We mounted another temperature sensor (PT-100 series) along the Stycast for control purposes. The whole system is connected to the top-load tube by a sapphire rod .

For measurements starting above $35K$, the exchange gas is kept at ambiant pressure. To start the measurements at lower temperatures, we decrease the pressure in the sample chamber which sets up a ^4He gas flow around the sample holder. A decrease of the

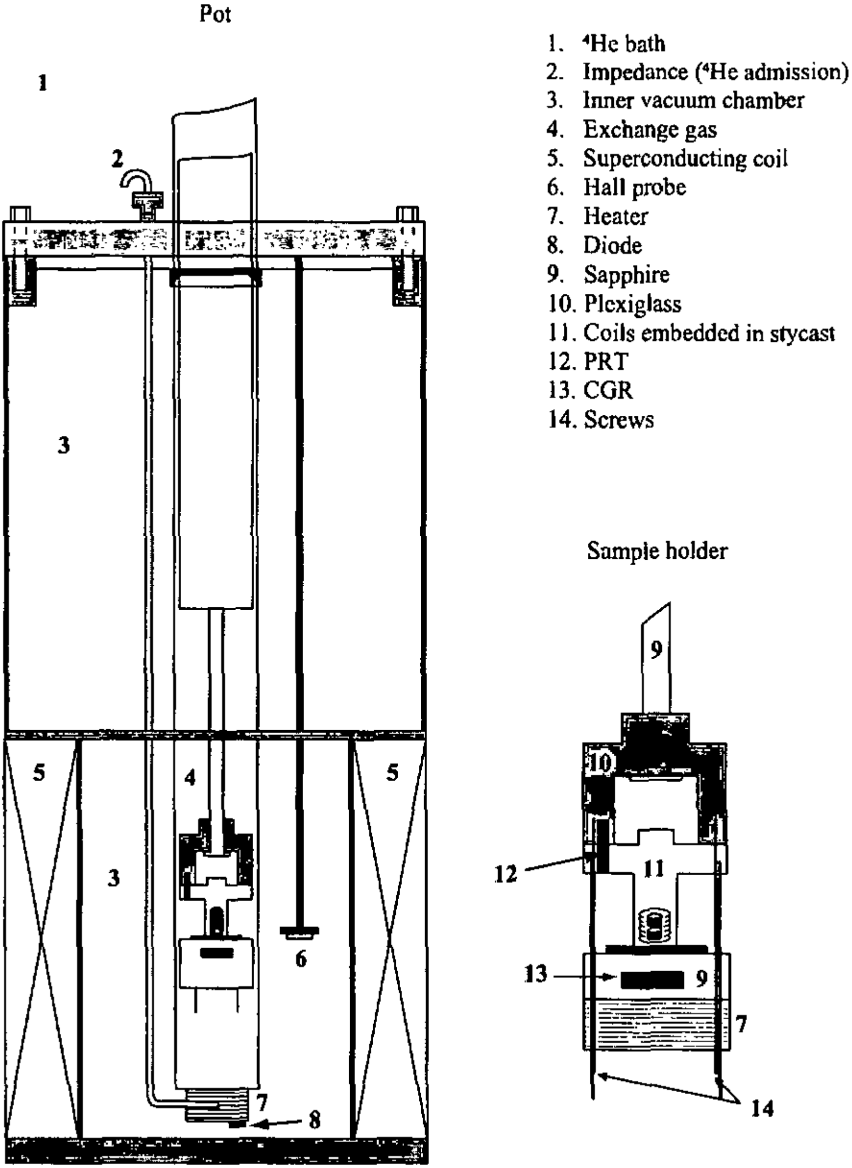

Figure 4.1: *The pot bearing the superconducting coil and the sample holder.*

pressure by about $100mbar$ is enough to allow measurements down to $6K$. Some care was taken to ensure an overall temperature reproducibility of better than $50\mathrm{m}K$ between $6K$ and $80K$ for the measurements of the thinner films.

4.1.1 Magnetic field

A description of the superconducting coil can be found in appendix A. It is however important to note here that the magnetic field produced by the coil in the persistent mode decays as a function of time according to $B(t) = B_0 \cdot e^{-t/\tau_B}$ where τ_B is a characteristic time. This is due to a small contact resistance in the circuit in which the persistent current flows. A decay of the magnetic field shifts the superconducting transition of the sample to higher temperatures and this effect becomes very noticeable after a few hours already. To limit this effect, we readjust the value of the magnetic field at least once a day and perform a temperature correction for each measured curve. For sample STO472, the temperature correction was based on the observation of the temperature shift of the superconducting transition as the magnetic field decayed with time. Assuming that the temperature follows the same type of law as the magnetic field does, we can determine the decay constant of the field as a fitting parameter in a plot of the logarithm of the superconducting transition as a function of time. The calibration constant which links a magnetic field shift to a temperature shift of the transition can then be obtained again as a fitting parameter. The mounting of a Hall sensor in the stainless steel pot allowed us to enhance the reliability of these corrections for samples STO610 [122] and STO607. The calibration can now be done for each magnetic field chosen and for each sample individually. The superconducting transition of the sample is measured for a given magnetic field and measured again for the same field decreased by two percent. This yields us the calibration constant linking the magnetic field shift to a temperature shift. The decay constant of the field is deduced from the Hall voltages measured at the beginning and at the end of each curve.

4.2 Measuring technique

The superconducting transition of the sample is measured by means of an inductive technique [123] which was first applied to superconducting thin films by Fiory and Hebard [87, 124]. This technique is the cousin of the ac susceptibility technique used commonly for bulk samples. The system is composed of a drive coil enclosing an astatically wound detection coil. The drive coil carries an ac current creating an electromagnetic field $\vec{h}_{ac}(t)$ at the surface of the sample. As a consequence, a screening current rises in the sample (below T_c) inducing a voltage drop δV at the terminals of the detection coil. The basic principle of the measurement relies on the fact that the mutual inductance of the drive and detection coils is modified by the presence of the sample. If the detection coil is well balanced, the signal vanishes when the sample is absent. The amplitude of the signal δV is maximum when the conductivity of the sample is maximum which happens at low temperatures. We are thus sensitive to the screening properties of the sample. The physical quantity that we extract from these measurements is the complex sheet (or surface)

conductivity of the sample. The study of bulk samples with this method is delicate since the signal depends essentially on the surface properties of the material. For thin films however, the screening current circulates in the whole thickness of the sample and if the film is thin enough, we can assume a uniform current distribution through the sample.
This measuring technique presents a few advantages. First, no contacts are necessary, allowing to keep the surface of the sample in its primitive state and avoid problems due to thermal voltages. An other advantage is the good sensitivity achieved using a lock-in detection technique. We can measure inductances down to about $10pH$, corresponding to an impedance of about $60n\Omega$ at a frequency of $1kHz$. Thanks to this sensitivity, we can use very low excitation currents and thus explore the linear regime where the response of the system is directly proportional to the excitation level.

We apply a dc external magnetic field $\vec{H}$ in order to have vortices in the sample, the total field being then $\vec{H} + \vec{h}_{ac}(t)$. The presence of the *ac* field $\vec{h}_{ac}(t)$ at the surface of the sample disturbs the arrangement of the flux lines and leads to a redistribution of the local magnetic induction and current density in the sample. The local variation of the induction $\delta\vec{B}$ is given by $\delta\vec{B} = \vec{\nabla} \wedge \delta\vec{A}$ where $\delta\vec{A} = \vec{u} \wedge \vec{B}$ according to [125]. The quantity $\vec{u}$ represents here the vortex displacement field. Using vector operations, the expression for $\delta\vec{B}$ can be written

$$\delta\vec{B} = -\vec{B}\vec{\nabla} \cdot \vec{u} + (\vec{B} \cdot \vec{\nabla})\vec{u} - (\vec{u} \cdot \vec{\nabla})\vec{B}$$

where $((\vec{B} \cdot \vec{\nabla})\vec{u})_i = \sum_j B_j \frac{\partial}{\partial x_j} u_i$. The first two terms are related to the elastic compression and tilt properties of the flux lattice respectively [126] and the third term becomes negligible in the limit $\delta B \lesssim \mu_0 h_{ac} \ll B$ [127]. Adding vortices to the lattice (by means of $\vec{h}_{ac}$) will thus, a priori, lead only to compression or tilt deformations of the vortex lattice but no shear. The presence of defects in the film however, will lead to a pinning of the flux lines (see Sec. 2.3). And in that case, shear deformations of the vortex arrangement may also appear. In fact, due to the relative strength of the elastic moduli, we expect that shear deformations of the vortex lattice will be much more easily driven than compression deformations or even tilt deformations in our particular case, see Sec. 5.1.3.
The elastic properties of the vortex lattice will thus play an important role in determining the response of the film in the mixed state. This basically means that the measured voltage δV caused by the local flux change carries information about the dynamic properties of the vortex lattice which is our main interest here.

4.2.1 Geometry

In Fig. 4.2, we show a sketch of the coil assembly whose geometrical parameters can be found in Table 4.1. The ac magnetic field produced by the drive coil can be estimated at the center of the coil, close to the surface of the sample. Using the parameters of

Table 4.1 and for a driving current of $7\mu A$, we obtain $\mu_0 h_{ac} \approx 2.0 \cdot 10^{-8} T$ ($0.2mG$) which is a relatively small value (see e.g. [128–130] for comparison) garanteeing a linear response.

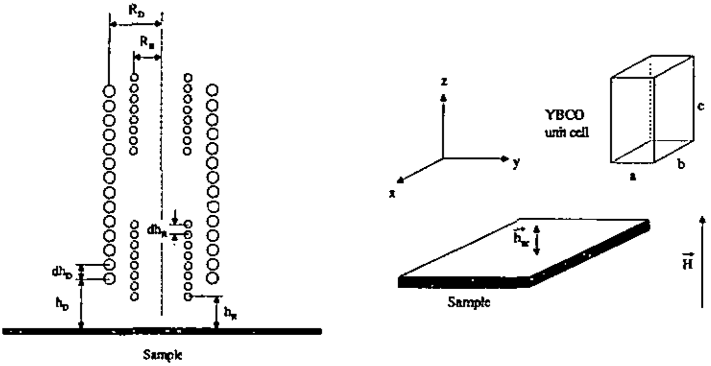

Figure 4.2: *Left: Sketch of the coils. Right: Geometry of the experiment.*

	Drive coil	Receive coil
Radius	$R_D = 2mm$	$R_R = 1.2mm$
Distance between turns	$\delta h_D = 0.2mm$	$\delta h_R = 25\mu m$
Number of turns	$N_D = 22$	$N_R = 28$
Distance first turn/sample	$h_D = 0.3mm$	$h_R = 0.1 h_D$
Estimated inductance	$1.2\mu H$	$2.5\mu H$

Table 4.1: *Parameters of the coils. At room temperature, the resistances of the coils measured at the top of the insert are 7Ω for the drive coil and 34Ω for the receive coil. The inductances of the coils are given by $L = \mu_0 \pi R_\alpha^2 / l_\alpha N_\alpha k_\alpha$ where $l_\alpha = N_\alpha \delta h_\alpha$ and k_α depends on the ratio $2R_\alpha / l_\alpha$, $k_D \simeq 0.7, k_R \simeq 0.4$, see for example [131]. We assume a magnetic permeability of $\mu = 1$ for the Stycast.*

4.2.2 Electrodynamics of the system

When a time-varying electromagnetic field is present at the surface of a metal, the skin effect theory is usually employed to describe the behavior of the metal. The electromagnetic field will decay below the surface as $e^{-z/\delta}$ where δ is the complex skin depth and depends on the resistivity ρ of the metal and the angular frequency ω of the oscillating electromagnetic field. The expression for δ is given by

$$\delta = \sqrt{\frac{\rho}{i\omega\mu_0}}$$

The metal thus exhibits a characteristic surface impedance Z_s defined by the ratio E/H of the electric and magnetic fields at the surface of the sample: $Z_s = \rho/\delta = i\omega\mu_0\delta$. When the sample is a thin film, the skin depth is replaced with the thickness d of the sample provided d is much larger than δ and much smaller than the width and the length of the sample. The sheet impedance may then be written

$$Z_s \equiv R_s + i\omega L_s = \frac{\rho}{d} = \frac{Re(\rho) + iIm(\rho)}{d} \tag{4.1}$$

Our system measures a conductivity $\sigma = 1/\rho$ rather than a resistivity. In fact, the voltage that we collect is complex and the out-of-phase component $Im(\delta V)$ is a measure of the screening efficiency (thus the superfluidity) of the sample whereas the in-phase component $Re(\delta V)$ measures the dissipation in the sample. While $Im(\delta V)$ decreases monotonically when the sample is heated up from the superconducting state to the normal state, $Re(\delta V)$ rises from zero, then exhibits a maximum at a temperature T_p and then returns to a small value $\propto d/\rho_n$ at high temperature (see Eq. (4.12) below).

Calculation of the induced voltage

In order to work out the relationship between the measured voltage δV and the sheet impedance Z_s [123], we first need to calculate the sheet current density $\vec{K}_s = \vec{j}d$ induced in the sample by the drive coil. From this result, we will then calculate the induced voltage δV appearing at the terminals of the detection coil. Due to our geometry, the use of cylindrical coordinates $\vec{r} = (r, \varphi, z)$ is a natural choice. The surface of the sample defines the plane $z = 0$ and the $\hat{z}$ axis coincides with the symmetry axis of the coils. We assume a $e^{i\omega t}$ time dependence for the fields and the driving current.
The *first important approximation* is to treat the sample as a two-dimensional object in the xy plane. This is adequate if the sheet current density $\vec{K}_s$ is constant along the z axis over the whole thickness d of the film, a condition which essentially translates to $j_z = 0$. This approach is valid for YBCO films with thicknesses verifying $d \ll \lambda$ [87]. As stressed by S. J. Turneaure *et al.* [132], the finite size of the sample does not affect significantly the mutual inductance of the system and one can assume an infinite size for the sample to perform the calculations as long as the sample is typically twice as large as the drive coil diameter. Mesurements of Nb films with different sizes an geometries confirm this statement [133]. The *second approximation* consists in assuming that the current density is isotropic in the xy plane.

The electrical field $\vec{E}$ in the sample is related to the sheet impedance by

$$\vec{E}(r, z=0) = Z_s \vec{K}_s(r, z=0) = -i\omega \vec{A}(r, z=0) \tag{4.2}$$

where $\vec{A}$ is the vector potential. Using Maxwell's equations where we neglect the displacement current in Ampère's law

$$\begin{aligned} \vec{\nabla}\vec{B} &= 0 \qquad & \vec{\nabla} \wedge \vec{H} &= \vec{j} \\ \vec{\nabla}\vec{D} &= 0 \qquad & \vec{\nabla} \wedge \vec{E} &= -\frac{\partial \vec{B}}{\partial t} \end{aligned}$$

we can express the relationship between the vector potential and the sheet current density. This expression is valid above and in the sample and reads, in the Coulomb gauge $\vec{\nabla}\vec{A} = 0$,

$$-\nabla^2 \vec{A}(r, z) = \mu_0 \vec{K}_s(r)\delta(z) + \mu_0 \vec{j}_D(r, z) \tag{4.3}$$

The current density is separated in two terms accounting respectively for the response of the film $\vec{K}_s$ and the direct contribution $\vec{j}_D(r, z)$ from the drive coil. To perform the integration of Eq. (4.3), we rewrite it in Fourier space using cylindrical coordinates $\vec{q} = (q_t, \theta, q_z)$:

$$(q_t^2 + q_z^2)\widehat{\vec{A}}(\vec{q}) = -\frac{i\mu_0\omega}{Z_s}\widehat{\vec{A}}(q_t, z=0) + \mu_0 \widehat{\vec{j}}_D(\vec{q}) \tag{4.4}$$

The Fourier transform of the vector potential can be written [32, 124]

$$\widehat{\vec{A}}(q_t, z=0) = \frac{1}{2\pi}\int \widehat{\vec{A}}(\vec{q})dq_z$$

and $\widehat{\vec{A}}(\vec{q})$ is given by Eq. (4.4). This integral can be solved with the residue method [32] and yields

$$\widehat{\vec{K}}_s(q_t) = -\frac{\widehat{\vec{j}}_D(q_t, -iq_t)}{1 - iq_t \frac{2}{\mu_0}\frac{Z_s}{\omega}}$$

The current density distribution $\vec{j}_D(r, z)$ generated by the drive coil can be written

$$\vec{j}_D(r, z) = I_D \delta(r - R_D)\hat{\varphi} \sum_{n=0}^{N_D - 1} \delta(z - h_D - n\delta h_D)$$

with $\hat{\varphi} = (-sin(\varphi), cos(\varphi), 0)$. In Fourier space, the expression reads

$$\widehat{\vec{j}}_D(\vec{q}) = -2\pi i I_D R_D J_1(q_t R_D) e^{-iq_z h_D} \frac{1 - e^{-iN_D q_z \delta h_D}}{1 - e^{-iq_z \delta h_D}}$$

The expression for the sheet current density transformed back in the real space is thus given by the integral

$$\vec{K}_s(r) = I_D R_D \int_0^\infty dq_t \frac{q_t e^{-q_t h_D}}{1 - iq_t \frac{2}{\mu_0} \frac{Z_s}{\omega}} J_1(q_t R_D) J_1(q_t r) \frac{1 - e^{-N_D q_t \delta h_D}}{1 - e^{-q_t \delta h_D}} \tag{4.5}$$

We can now calculate the voltage δV induced at the terminals of the receive coil by the current in the sample. We neglect here any contribution which would arise from a bad compensation of the receive coil. Using Ampère's law, we write the electric field $\delta\widehat{\vec{E}}$ in Fourier space as

$$-\frac{q_t^2 + q_z^2}{i\omega} \delta\widehat{\vec{E}}(\vec{q}) = \mu_0 \widehat{\vec{K}}_s(q_t)$$

The voltage is obtained by the path integral of the electric field along each turn of the receive coil. In real space, we find

$$\delta V(Z_s) = i\omega I_D \pi \mu_o \int_0^\infty dq_t \frac{F_R(q_t) F_D(q_t)}{1 + q_t \frac{2}{\mu_0} \frac{Z_s}{i\omega}} \tag{4.6}$$

where the functions $F_\alpha(q_t)$ depend only on the geometry of the coils:

$$F_\alpha(q_t) = R_\alpha J_1(q_t R_\alpha) e^{-q_t h_\alpha} \frac{1 - e^{-N_\alpha q_t \delta h_\alpha}}{1 - e^{-q_t \delta h_\alpha}} \tag{4.7}$$

Eq. (4.6) establishes the relationship between the measured voltage δV and the sheet impedance of the film in a non-trivial way involving the geometry of the system. The real and imaginary parts of the voltage depend both on the real and imaginary parts of the sheet impedance. To obtain an exact value for Z_s, we have to calibrate the system and use a numerical inversion procedure which is briefly described in Sec. 4.2.3.

A non-exact but easier method to extract the sheet impedance derives from the peaked shape of the geometrical function $M(x) = F_R(x) F_D(x)$. We approximate $M(x)$ by a δ-function centered at $x = x_m$ which yields

$$\frac{R_s}{\omega} = -\frac{\mu_0 h}{2x_m} \frac{V_{ss} Re(\delta V)}{|\delta V|^2} \tag{4.8}$$

$$L_s = \frac{\mu_0 h}{2x_m} \left(\frac{V_{ss} Im(\delta V)}{|\delta V|^2} - 1 \right) \tag{4.9}$$

where V_{ss} is defined below. Due to this particular shape of the geometrical function, we equivalently say that the system selects mainly wave vectors verifying $1/q_t = (h_D + h_R)/x_m \simeq 1.4mm$ for our system.

In the *low temperature limit*, the sheet impedance of the sample is essentially inductive: $Z_s = i\omega L_s$ and thus $Re(\delta V) = 0$. In this strong screening limit, the mutual inductance change depends only on the geometry of the system and we have

$$Im(\delta V)(T \to 0) = V_{ss} = i\omega I_D \pi \mu_0 \int_0^\infty dq_t F_R(q_t) F_D(q_t) \tag{4.10}$$

which is true if $2q_t L_s/\mu_0 \ll 1$. The characteristic inductance $M_c = \mu_0/(2q_t) \simeq 0.9nH$ is an important parameter here. The ratio L_s/M_c , depending on the properties of the sample and the coils, will settle whether the system actually reaches the strong screening limit. Using Eq. (4.9), we can write the relationship between the imaginary part of the signal and V_{ss} as

$$Im(\delta V) = \frac{V_{ss}}{1 + L_s/M_c} \tag{4.11}$$

Identifying L_s to $L_k = \mu_0 \lambda^2/d$ and using the appropriate values for λ and d, we find $Im(\delta V) \simeq 0.9992\ V_{ss}$ for the thickest film (STO472) and $Im(\delta V) \simeq 0.85 V_{ss}$ for the thinner film (STO607). We thus understand that a thin film will not induce a signal reaching the geometrical value, whereas a thick films will, in the limit of our experimental resolution. This justifies why we deduce the value for V_{ss} from the thick films measurements. This calibration makes it possible to adjust the parameters of the coils for the calculation of V_{ss} with Eq. (4.10), the most uncertain parameter being the distance from the receive coil to the sample. For our system, we find $M_{ss} = V_{ss}/(\omega I_D) \simeq 286nH$.

When the sample is in the *normal state*, the sheet impedance is essentially resistive with $Z_s = R_s$ and $Im(\delta V) = 0$ if the detection coil is perfectly balanced. The relation between the real part of the signal and V_{ss} derived from Eq. (4.8) reads

$$Re(\delta V) = V_{ss} M_c \frac{\omega}{R_s} \tag{4.12}$$

At small enough frequencies and for large enough normal state resistances, $Re(\delta V)$ will be negligible. If we use the values from Table 3.5 on page 56 for the normal state resistivity, we get $Re(\delta V) \simeq 4.1 \cdot 10^{-5} V_{ss}$ (STO472) and $Re(\delta V) \simeq 3.9 \cdot 10^{-7} V_{ss}$ (STO607) for the less favorable frequency $(\omega/2\pi = 100kHz)$.

In practice, the balancing of the receive coil is not perfect which adds a constant contribution to the imaginary part of the signal. This contribution is substracted from the signal before the numerical inversion is performed. When necessary, we also perform a phase correction of the signal which allows to adjust the level of $Re(\delta V)$ at low and high temperatures.

The relative uncertainty $\Delta L_s/L_s$ on the inductance is smallest when L_s is equal to the characteristic inductance M_c (Fig. 4.3) whereas the relative uncertainty for the resistance increases linearly with R_s. From Eqs. (4.11) and (4.12), we can write

$$\frac{\Delta L_s}{L_s} = \frac{(1+L/M_c)^2}{L/M_c}\frac{\Delta Im(\delta V)}{V_{ss}}$$
$$\frac{\Delta(R_s/\omega)}{R_s/\omega} = \frac{R/\omega}{M_c}\frac{\Delta Re(\delta V)}{V_{ss}}$$

where $\Delta Im(\delta V) \simeq \Delta Re(\delta V) \lesssim 1\% V_{ss}$ at $f = 1kHz$ and $B = 1.0T$.

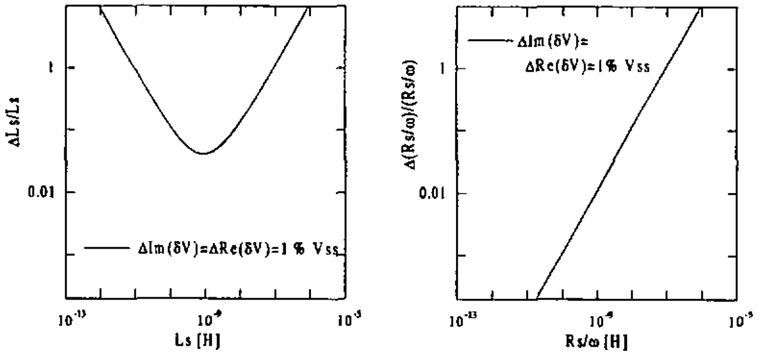

Figure 4.3: *Relative uncertainties $\Delta L_s/L_s$ and $\Delta(R_s/\omega)/(R_s/\omega)$ as a function of L_s and R_s/ω, respectively, for $\Delta Im(\delta V) = \Delta Re(\delta V) = 1\%$.*

4.2.3 Numerical inversion

To extract the real and imaginary components R_s and L_s of the sheet impedance of the film from the measured response expressed by Eq. (4.6), we first define the complex dimensionless variables [87,123]

$$m = |m|e^{i\theta_m} \equiv (\delta V/V_{ss})^*$$
$$u = |u|e^{i\theta_u} \equiv m/|m|^2 - 1$$
$$l = |l|e^{i\theta_l} \equiv (2Z_s/(i\mu_0 h\omega))^*$$

which allow to get rid of most of the geometrical parameters. Next, we build two tables containing the values for $|u|$ and θ_u as a function of $|l|$ and θ_l, covering the range of interest for u. Since $|l|$ is a smooth monotonous function of $|u|$, we can exchange the role of these two quantities by interpolation. This yields a table for $|l|$ (T1) and a table for θ_u (T2) as a function of $|u|$ and θ_l. Knowing the data ($|u|$ and θ_u), we can extract a value for θ_l from table T2. The value for $|l|$ is then easily derived from table T1.

4.2.4 Sheet impedance

To properly characterize the electrical response of the sample to an external electromagnetic excitation, we should take into account the contributions from the superfluid (cooper pairs), the normal electrons and the moving vortices [134]. The contribution from the normal electrons is assumed to be proportionnal to the time derivative of the contribution from the superelectrons [134, 135] with the proportionality factor $\omega L_k/R_N$ where $L_k = \mu_0\lambda^2/d$ and $R_N = \rho_N/d$. As long as $\omega \ll R_N/L_k$, the contribution from the normal electrons can be ignored which is the case for our measurements since $R_N/L_k \approx 10^{13}Hz$ for our samples. In the absence of magnetic field, the sheet impedance reads

$$Z_s = i\omega L_k$$

As the magnetic field is raised, vortices will enter in the sample and their motion will give rise to a resistive and an inductive component. We thus write the sheet impedance as

$$Z_s = R_s + i\omega L_s$$

At that point, the sheet impedance ought to be written as the sum of a contribution from the superfluid background $i\omega L_k$ plus a contribution from the vortices Z_v yielding $Z_s = Z_v + i\omega L_k$ [134]. However, the contribution from the moving vortices will be generally dominant in the expression for the sheet impedance, unless the applied magnetic field is very low.

We shall mention that writing the sheet impedance $Z_s = R_s + i\omega L_s$ consists to consider the equivalent circuit of the sample as a resistance R_s in series with an inductance L_s. Models usually make predictions for the conductance rather than the impedance of the system studied. Since conductances have to be added, the sheet impedance should be written in its parallel-equivalent real and imaginary parts: $Z_s^{-1} = R_p^{-1} + (i\omega L_p)^{-1}$ where R_p^{-1} and $(i\omega L_p)^{-1}$ represent the real and imaginary parts of the sheet conductance $G_s = 1/Z_s$.

Simple algebra allows to write R_p and L_p as a function of the measured quantities R_s and L_s. We have thus to decide whether we talk in terms of conductance or impedance when comparing the data to the predictions of a model and use the correct quantities. For instance, in the spirit of a two-fluid model where the superconductor is described as a dissipative channel in parallel with an inductive channel, it is natural to adopt a description in terms of conductances rather than impedances. It is worth mentionning that the quantity L_p^{-1} is in fact a measure of the macroscopic superconducting phase coherence in the sample. What is important to realize is that the differences between the serial and parallel quantities (R_s and R_p or L_s and L_p) appear at low temperatures for the resistance and at high temperatures for the inductance. Let us consider the case of the resistance to understand this. In the serial case, the resistance R_s has to vanish when the temperature tends to zero since the response of the sample is essentially inductive at low temperatures. In the parallel case, the resistance R_p has to become very large in order to let the inductive channel become the most favorable path. This explains why the resistances R_s and R_p will become very different from each other at low temperatures.

4.2.5 Electronics

The internal oscillator of the lock-in (EG&G 5210) is used to set up the current in the drive coil. A $1k\Omega$ metal film resistor limits the current to typically $7\mu A$. The signal induced at the detection coil terminals is directly fed into the lock-in for frequencies above $10kHz$. For lower frequencies, we use a low impedance transformer (PAR 1901) to amplify the signal 100 times before detecting it with the lock-in. The amplification factor remains stable although the resistance of the detection coil (source resistance seen by the transformer) varies slightly with temperature from 1Ω up to 6Ω between $4.2K$ and $90K$. The resistance of the drive coil does not increase significantly in the same temperature interval (1.5Ω to 2.5Ω). We measured the background noise in a typical detection circuit using a spectrum analyzer (HP3562) and found it to be of the order of $20nV/\sqrt{Hz}$ between $100Hz$ and $100kHz$. For a typical time constant of $1s$ and a $12dB/oct$ filter roll-off, we have an equivalent noise bandwith of $0.125Hz$ (see for instance Ref. 136). We thus expect a noise of a few nV ($\approx 7nV$) on the signal whereas we intend to measure signals of about $10nV$ at $1kHz$. It appears quite clearly that a lock-in detection technique is necessary to perform these measurements.

The imaginary and real part of the signal are read by a computer via an AD converter whereas the temperature of the CGR sensor is read via a GPIB bus. The temperature controller (DRC 91CA) monitors the sensors mounted on the sample holder and ensures the heating of the sample with a PID control loop. More details can be found in [119–122]. The measurements of sample STO610 at high frequencies ($f > 30kHz$) let appear an undesirabe background signal above the transition temperature. Such signals are known to appear usually when eddy currents circulate either in the sample when its normal state resistance is weak (which is not the case here since $R_N = \rho_N/d \gtrsim 10\Omega$ for all the samples, see Sec. 3.4) or in metallic elements close to the sample as, for instance, the metallic can in which the CGR thermometer is enclosed. A parasitical tension may thus be induced at the terminals of the detection coil. This signal appears only at high temperatures when the film reaches the normal state and does not affect significantly the data when the sample is superconducting.

5 Results and discussion

In the first section of this chapter, we summarize and comment the general behavior of the raw and inverted data. On the basis of the observations done and by estimating a few forces relevant for the vortex dynamics, we give a first qualitative description of the behavior of the vortex medium in our films. In the next sections, we present and discuss more specific analyses of the data and start with the extraction of the penetration depth from the measurements performed in the absence of magnetic field. Since we are dealing with very thin films, we address, in the same section, the question of the existence of a BKT phase transition in our layers. The behavior of the data in the high temperature regime is reviewed in the next section where we focus our attention on the activation energy and its dependence on the magnetic field. A crossover is observed which we interpret as a thickness and magnetic field driven crossover from a 3D behavior of the vortices (soft vortices) to a 2D behavior (stiff vortices). We then investigate whether the vortex medium in our films undergoes a true thermodynamic phase transition from a vortex-liquid phase to a vortex-glass phase by means of a scaling analysis of our data. The sketch of a $B-T$ phase diagram for the vortex system is then proposed as a mean to present a partial synthesis of our observations and to point out some problems of interpretation. A way to clarify the situation is suggested in the next section and consists in explaining the behavior of our data in terms of a crossover from a pinned vortex liquid to a collectively pinned, frozen vortex liquid. Finally, we present an alernative phenomenological description of the vortex dynamics in terms of a crossover from a plastic response of the vortex medium at high temperatures (liquid-like state) to an elastic response (solid-like state) at low temperatures. The description consists in considering the vortices as a viscoelastic medium which will behave as a liquid or as a solid depending on the time scale at which the system is investigated.

5.1 General trends

We first comment the curves for $Im(\delta V)$ and $Re(\delta V)$ for the different films measured as a function of temperature, for different magnetic fields and thicknesses. We then present the inversed quantities, the resistance and the inductance, as a function of temperature and frequency.

5.1.1 Measured voltage

The typical behavior of $Im(\delta V)$ and $Re(\delta V)$ as a function of temperature is illustrated in Fig. 5.1 where we plot the curves obtained for sample STO472 at various frequencies (left, $B = 2.0T$) and fields (right, $f = 1kHz$). The first point is that the transition is shifted towards higher temperatures as the frequency $\omega = 2\pi f$ increases. We interpret this behavior by arguing that the system, at the time scale (ω^{-1}) of the experiment, becomes less sensitive to the long time-scale fluctuations of the order parameter as the probing frequency increases. The consequence is that the superconducting state persists up to higher temperatures.

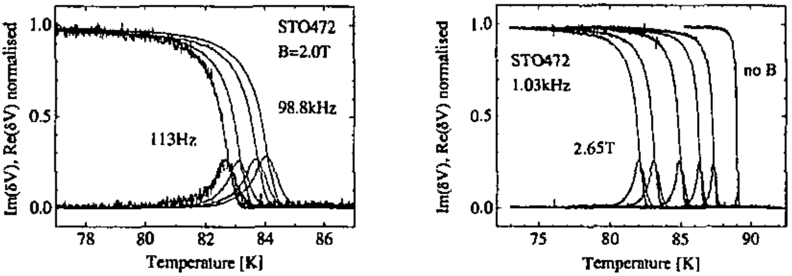

Figure 5.1: *Temperature dependence of $Im(\delta V)$ and $Re(\delta V)$ (sample STO472) for different frequencies at $B = 2.0T$ (left) and for different magnetic fields at $f = 1.03kHz$. The frequencies in the left plot are $\omega/2\pi = 113Hz$, $1.03kHz$, $15.5kHz$ and $98.8kHz$ from left to right. The magnetic fields in the right plot are $B = 2.65T$, $2.0T$, $1.0T$, $0.5T$, $0.25T$ and $0T$, from left to right.*

When we increase the magnetic field, superconductivity in the film is weakened by the presence of vortices, which translates into a decreased transition temperature and an enlarged $Re(\delta V)$ peak. We shall keep in mind that the earth magnetic field ($\sim 50\mu T$) is strong enough to bring the sample into the mixed state as mentioned in Sec. 3.1.2. This basically means that our films are always in the mixed state and that there is qualitatively no difference between measurements performed with or without a dc background field, apart from the density of vortices in the sample. The notation 'no B' in the graphs means that the measurement was done in the presence of the background magnetic field only.

As the thickness of the film is decreased, the superconducting transition temperature decreases and the width of the transition increases. Fig. 5.2 shows the imaginary and real parts of δV for four films as a function of temperature at $1kHz$ in the absence of magnetic field (left) and for $B = 1.0T$ (right).

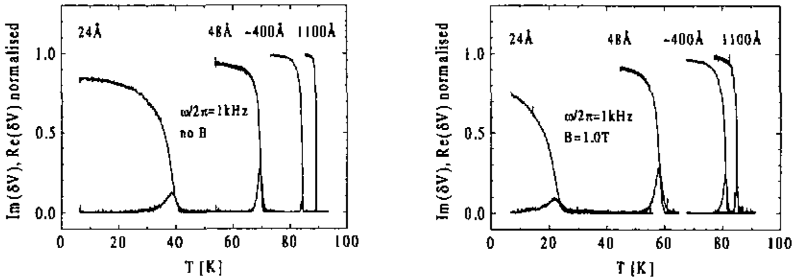

Figure 5.2: *Temperature dependence of $Im(\delta V)$ and $Re(\delta V)$ for samples STO607 (24Å), STO610 (48Å), STO269 (~ 400Å) and STO472 (1100Å) at 1kHz in the absence of applied field (left) and for $B = 1.0T$ (right).*

5.1.2 Inverted data: resistance and inductance

After measuring the voltage δV, we use the procedure described in Sec. 4.2.3 to extract the sheet impedance

$$Z_s = R_s + i\omega L_s = (R_p^{-1} + (i\omega L_p)^{-1})^{-1} = G_s^{-1}$$

of the film. The behavior of R_s and L_p^{-1} as a function of the inverse temperature for different frequencies is shown in Fig. 5.3 and Fig. 5.4 for samples STO472 and STO610. The data are shown up and down to the temperatures where the noise starts to increase strongly. We plot L_p^{-1} rather than L_s^{-1} since L_p^{-1} is the quantity which represents better the superconducting properties of the sample measured. Indeed, L_p^{-1} is related to the imaginary part of the conductance $G_s = Z_s^{-1}$ through $L_p^{-1} = \omega Im(G(\omega))$.

The scattering of the data increases significantly as the real and imaginary curves approach zero or when $Im(\delta V)$ is close to the geometrical saturation value at low temperatures, see Sec. 4.2.2. Since the real part of the signal is closely related to the resistance of the film (Eq. (4.8)), the temperature zone where the resistance is well defined extends roughly to the width of the $Re(\delta V)$ peak. The same argument holds for the inductance, related to the imaginary part of the signal (Eq. (4.9)), where the useful temperature domain is determined by the width of the transition in $Im(\delta V)$. We shall however stress that the useful temperature domain for the inductance extends to much lower temperatures for very thin films since these films do not screen the ac drive field as well as the thick films do, with the consequence that $Im(\delta V)$ will not reach the geometrical saturation value.

Starting at low temperatures where the behavior of both the resistance and the inductance is weakly temperature-dependent, we enter a regime where the resistance increases very rapidly whereas the inverse inductance decreases also rapidly, signaling that superconductivity is being supressed in the sample. Plotting the resistance as a function of the inverse temperature (Arrhenius plot of the resistance) reveals that, at high temperatures, the resistance is proportional to e^{-U_R/k_BT} where U_R is an activation energy which does not depend on the frequency but varies with the magnetic field. The inverse inductance as a function of the inverse temperature shows the same type of thermally activated behavior at high temperatures, following e^{U_L/k_BT} where the activation energy U_L is also frequency independent.

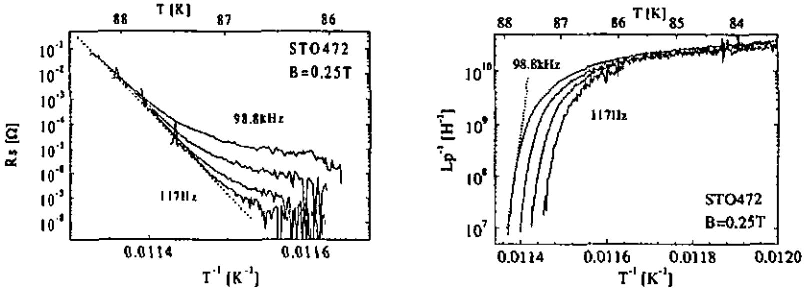

Figure 5.3: *Temperature dependence of R_s (left) and L_p^{-1} (right) for sample STO472 at $B = 0.25T$. The frequencies are $117Hz$, $1.03kHz$, $10.7kHz$ and $98.8kHz$.*

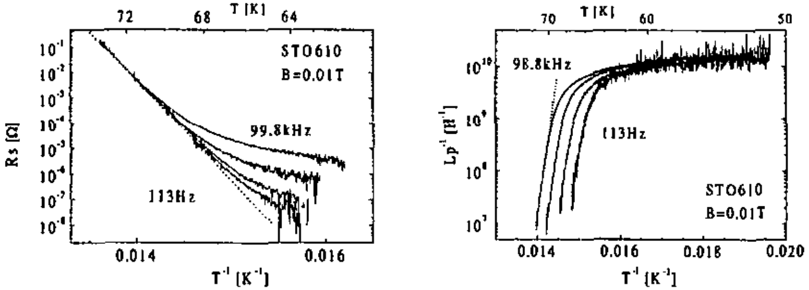

Figure 5.4: *Temperature dependence of R_s (left) and L_p^{-1} (right) for sample STO610 at $B = 0.01T$. The frequencies are $113Hz$, $1.05kHz$, $10.3kHz$ and $99.8kHz$.*

Fig. 5.5 shows the effect of the magnetic field on the resistance R_s and the inverse parallel inductance L_p^{-1} for sample STO472 at a frequency of $1kHz$. Both the resistance and the inductance can be measured over a wider temperature range when the field increases and we observe a decrease of the slope in the high temperature regime meaning a decrease in the activation energy. We also notice that the temperature T_p of the peak in $Re(\delta V)$ is located roughly at the end of the thermally activated regime as shown for the curve at $1.0T$. The same plots are shown in Fig. 5.6 for sample STO607. Notice the much wider temperature regime over which the data can be plotted.

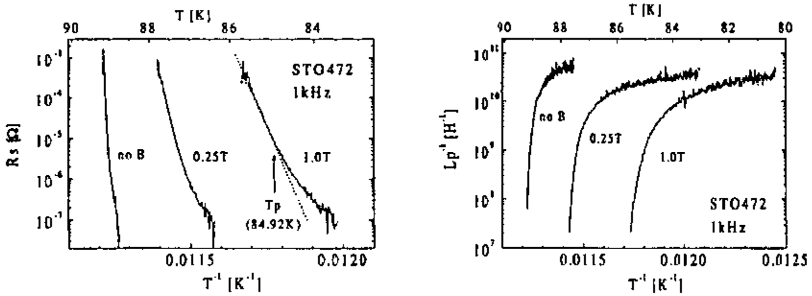

Figure 5.5: *Temperature dependence of R_s (left) and L_p^{-1} (right) for sample STO472 at 1kHz for three values of the magnetic field.*

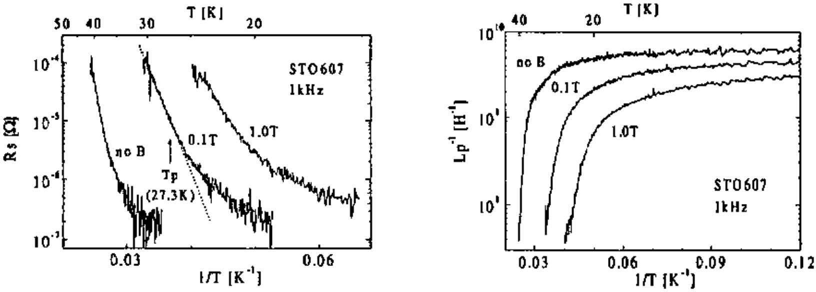

Figure 5.6: *Temperature dependence of R_s (left) and L_p^{-1} (right) for sample STO607 at 1kHz for three values of the magnetic field.*

We finally show the behavior of the resistance R_s and the inductance L_s as a function of frequency $f = \omega/(2\pi)$ at different temperatures (isotherms) in Fig. 5.7 and Fig. 5.8 for samples STO472 and STO610. We plot here L_s rather than L_p for 'mathematical convenience', since $L_s(\omega)$ follows roughly a power-law behavior over the entire temperature range considered while $L_p(\omega)$ does not. Remember that L_s and L_p merge at low temperatures while R_s and R_p merge at high temperatures (see Sec. 4.2.4).

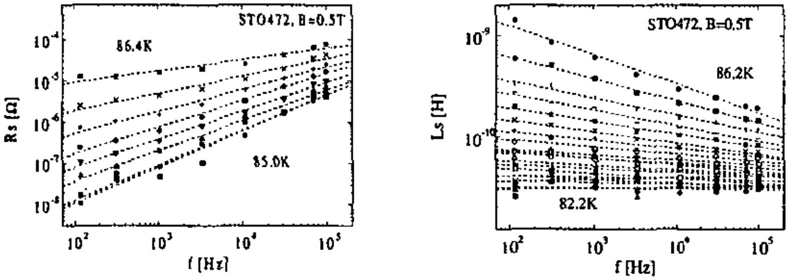

Figure 5.7: *Frequency dependence of the resistance (left) and the inductance (right) at various temperatures for sample STO472. The dotted lines are linear fits to the data. The temperature step between two isotherms is* $0.2K$.

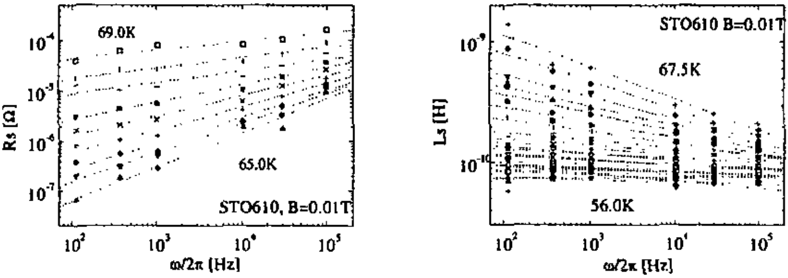

Figure 5.8: *Frequency dependence of the resistance (left) and the inductance (right) at various temperatures for sample STO610. The dotted lines are linear fits to the data. The temperature step between two isotherms is* $0.5K$.

In the crossover region around T_p and over the frequency range explored in our measurements, we observe power law dependencies $R_s \propto \omega^{\alpha_R}$ and $L_s \propto \omega^{\alpha_L}$ where the exponents appear to be temperature dependent. At low temperatures, the exponent α_R for the resistance is close to 1 whereas the inductance is roughly frequency independent ($\alpha_L \sim 0$). At high temperatures, on the other hand, R_s becomes roughly frequency independent. These frequency dependencies give us some evidence for the existence of a glass-like phase of the vortex medium at low temperatures since one expects, neglecting logarithmic corrections, $R_s(\omega) \propto \omega$ and L_s ω independent [11].

5.1.3 Qualitative discussion

From the behavior of the data observed for the different films, we can draw a qualitative picture for the vortex medium behavior. As mentioned above, the resistance in the high temperature regime follows $R_s \propto e^{-U/k_BT}$, where U is a frequency independent activation energy given by the slope of the graph. Here, the dissipation arises due to the thermally activated motion of vortices (TAFF regime) which may occur either by depinning of the vortices and/or the nucleation of edge dislocations or other plastic deformations in the vortex lattice. The energy barrier U depends on the magnetic field as can be noticed in Fig. 5.5, where the slopes of the graphs decrease as the magnetic field increases. Such a behavior is characteristic of a liquid-like vortex medium. As the temperature decreases, the mobility of the vortices (or equivalently, of the dislocations) decreases and we observe a crossover, close to $T_p(\omega)$, to a regime where the resistivity becomes nearly temperature independent. In this low temperature regime, we expect a very viscous vortex liquid with large characteristic time scales for the vortex motion. The question then arises whether the vortex medium undergoes a genuine thermodynamic phase transition into a solid-like phase at low temperatures or not. We shall discuss this point further ahead in this chapter.

At this point, it appears important to better understand the relative strength of the different forces relevant for the vortex dynamics in the sample. Table 5.1 gives the thickness of the films, the transition temperature T_{c0} and the temperature of the peak in $Re(\delta V)$ for a frequency of $1kHz$ at $B = 1.0T$. We then report an estimate for the approximate width G_iT_c of the region where thermal fluctuations become relevant, see Sec. 2.1.1. We use here $\xi_{ab}(0) = 15\text{Å}$ and $\gamma = 5$. The numerical values used for the penetration depth are those found in the next section. It clearly appears here that thermal fluctuations will be relevant over a wide range in temperature. This temperature range increases with decreasing thickness meaning that we expect wider transitions for thinner films, as observed on the data.

We then calculate the elastic restoring force per unit length f_r experienced by a vortex displaced from its equilibrium position by a distance $\delta x = a_0/10$. The estimate is performed using Eq. (2.24) for a magnetic field $B = 1.0T$ and at zero temperature. We shall remember that this calculation holds for a perfect vortex lattice provided $\delta x/a_0 < 1$. In the next lines of the table, we report estimates for the pinning force per unit length experienced by a vortex line in three different cases: for point pinning by oxygen vacancies, for correlated pinning by the core of screw dislocation and finally, for correlated pinning due to the thickness modulation of the film. We use the expressions given in Sec. 2.3 and calculate the estimates for $T = 0$. For samples STO472 and STO269, we make use of the relative surface roughness observed by AFM for sample STO615 (Sec. 3.3.2). For the average distance l_s between two valleys, we take $l_s = 0.2\mu m$ as obtained from the

AFM analysis as well. Following the arguments of Sec. 2.2.3, we finally estimate the entanglement temperature T_{ent} of the flux lattice for two different magnetic fields. This temperature is reached when the lateral wandering of the flux lines in the vortex lattice reaches the lattice spacing a_0 (at $1.0T$, $a_0 \simeq 455$Å). An estimate for the lateral wandering Λ_d at $T = T_p(1kHz, 1.0T)$ is calculated using Eq. (2.28).

Quantity		STO472	STO269	STO610	STO607
Thickness [Å]		1100	400	48	24
$T_{c0}[K]$		91.0	89.1	73.7	48.3
$T_p(1.0T, 1kHz)[K]$		84.92	80.95	57.90	21.65
$G_i T_c$ $[K]$		11	12	19	37
Elastic restoring force $[N/m]$	$T = 0$	$6.6 \cdot 10^{-5}$	$6.1 \cdot 10^{-5}$	$3.6 \cdot 10^{-5}$	$1.4 \cdot 10^{-5}$
Pinning force $[N/m]$ (point pins)	$T = 0$	$2.4 \cdot 10^{-4}$	$2.2 \cdot 10^{-4}$	$1.3 \cdot 10^{-4}$	$0.49 \cdot 10^{-4}$
Pinning force $[N/m]$ (screw dislocation core)	$T = 0$	$6.2 \cdot 10^{-4}$	$5.7 \cdot 10^{-4}$	$3.4 \cdot 10^{-4}$	$1.3 \cdot 10^{-4}$
Pinning force $[N/m]$ (thickness modulation)	$T = 0$	$9.9 \cdot 10^{-5}$	$9.2 \cdot 10^{-5}$	$2.2 \cdot 10^{-5}$	$0.38 \cdot 10^{-5}$
T_{ent} $[K]$	$B = 0.01T$	90.5	88.9	73.67	48.2999
T_{ent} $[K]$	$B = 1.0T$	59.7	74.1	71.3	48.29
Lateral wandering $[\mu m]$	$T = T_p$	4.4	1.9	0.27	0.0044

Table 5.1: *Numerical estimates of different quantities for the samples measured. The first four lines give the values for a few parameters as obtained from the measurements. Unless stated, the calculations are done for a magnetic field of* $1.0T$ *and assuming* $\gamma = 5$ *and* $\xi_{ab}(0) = 15$Å. *See text for details.*

From the comparison of the elastic restoring force and the different pinning forces at zero temperature, we first realize that the vortex lattice will be distorted by the defects present in the structure of the sample. However, the strength of the pinning force is not so large that we may expect independently pinned vortices. The interaction between vortices will have to be taken into account when modeling the response of the vortex system in our films. Since the calculations are done for a magnetic field of $1.0T$, we may wonder about the situation at much lower fields where a *gas* of almost independent vortices might form. However, we are dealing with thin films and, as mentioned in Chapter 2, the effective penetration depth in a thin film is given by $\lambda_{eff} = 2\lambda_{ab}^2/d$, which increases appreciably the range of the interaction between vortices. The values of $\lambda_{eff}(0)$ for our different films are typically larger than $1\mu m$ (see Table 5.2 in the next section). From these values, we observe that the vortices in our films cannot be considered as independent vortices since $a_0/\lambda_{eff} < 0.4$ for all magnetic fields verifying $B \geq 0.01T$. Even the earth magnetic field background will induce a large enough vortex density in the films, so that the interaction between vortices can definitely not be neglected, except for the 1100Å thick sample where the ratio a_0/λ_{eff} is greater than 5.

It is however difficult to clearly establish which force can be expected to play a dominant role in the vortex dynamics since the estimates for all forces per unit length do not appear significantly different from each other. A tentative statement might be to assume a random distribution of about equally efficient pinning centers in the samples. This may result in a collective pinning of the vortex medium if the pinning energy is small as compared to the elastic restoring energy. We can check this by coming back to Eq. (2.37) giving the net energy change per unit volume in the vortex medium due to a collective pinning of the vortices. The energy scales can be compared by calculating the ratio of the three coefficients $c_s = c_{66}/2$ (shear), $c_t = c_{44}/2$ (tilt) and c_p (pinning) of the strains $(\xi_{ab}/R_c)^2$, $(\xi_{ab}/L_c)^2$ and ξ_{ab}/R_c. From Eqs. (2.22) and (2.38), we obtain $c_p/c_s = \xi_{ab}/R_c$, which in our case verifies $\xi_{ab}/R_c \ll 1$, meaning that, at zero temperature, the pinning energy is much smaller than the elastic shear energy (weak pinning). Using the approximation $c_{44} \approx B^2/\mu_0$, the same process for the tilt energy yields[1] $c_pL_c/(R_cc_t) = \xi_{ab}/L_c$ which again verifies $\xi_{ab}/L_c \ll 1$ meaning that the pinning energy is also weak as compared to the elastic tilt energy. It thus appears that a collective pinning picture might be suited in our case. As already mentioned in Sec. 2.2.2, the ratio of the tilt and the shear moduli verifies, at zero temperature, $c_{44}/c_{66} \approx 16\pi B\lambda_{ab}^2/\phi_0 \gg 1$. We may thus ignore tilt (and compression) deformations of the vortex lattice in a first approximation.

Finally, we briefly comment the lateral wandering of the vortex lines induced by thermal fluctuations at non-zero temperature. It is interesting to look at the values obtained for the entanglement temperatures at two different magnetic fields for all the samples. It clearly appears that the flux lines will entangle and reconnect in the thick films STO472 and STO269, at least when the magnetic field is high enough. For the thinnest films, on the other hand, the temperature region between T_{ent} and T_{c0} is not very wide and even almost zero for sample STO607. This appears reasonable since short vortices are more rigid than long ones.

5.2 Extraction of the penetration depth

In the absence of magnetic field, the surface impedance of the film is essentially given by $Z = i\omega L_k$ where L_k is the inductance related to the superfluid density, or kinetic inductance, given by

$$L_k(T) = \frac{\mu_0\lambda^2(T)}{d} \propto \frac{m_s}{n_s} \tag{5.1}$$

where n_s is the density of superconducting electrons, and m_s their mass. We obtain the penetration depth extrapolated at zero temperature $\lambda_{ab}(0)$ by fitting the zero-field inductance. The first problem here is to choose the temperature domain over which the fit has to be executed. We know that close to T_c, the GL approach is not valid any more

---

[1] we have to amplify c_p by a factor L_c/R_c in order to compare the same strains.

due to fluctuations of the order parameter. In our case, we may reasonably think that GL theory can be applied up to the (low temperature) onset of the peak in $Re(\delta V)$ since this onset marks the temperature at which we start measuring significant resistivities. This fixes the upper temperature limit for the fit. The temperature dependence of the penetration depth is the next problem. A quadratic dependence ($\propto 1 - (T/T_c)^{\alpha}$, with $\alpha = 2$) for the inverse square penetration depth $\lambda^{-2}(T)$ is generally well suited for YBCO over a very large temperature range (see e.g. Ref. 7 and Ref. 137), particularly for YBCO films. In our case, extracting a precise temperature dependent penetration depth from the thick films measurements is delicate because the signal measured for these films at low temperatures is very close to the geometrical saturation value V_{ss} (see Sec. 4.2.2). For these films, we will only derive estimates for $\lambda_{ab}(0)$ and T_c assuming $\alpha = 2$. For the thinner films STO610 and STO607, however, the signal is found to saturate a few percent below the geometrical value, which allows addressing the question of the temperature dependence of λ_{ab} when $T \to 0$.

Fig. 5.9 shows $\lambda(T)_{ab}^{-2}$ as a function of temperature. We perform a two parameter fit on the curve using

$$\lambda(T)_{ab}^{-2} = \lambda(T)_{ab}^{-2}(0)\left[1 - \left(\frac{T}{T_c}\right)^{\alpha}\right] \tag{5.2}$$

with different values for the exponent α. The best agreement is obtained for $\alpha = 2$. An exponent $\alpha = 4$ would indicate a two-fluid like behavior whereas if we accept the possible presence of nodes in the superconducting gap (see for instance [138] for a short review of the possible unconventional pairing states in cuprates), the temperature dependence is expected to be linear at low temperatures. A linear temperature dependence has been reported for YBCO single crystals [139, 140] and for YBCO films [141, 142] giving substantial evidence for a non-uniform gap.

A linear fit to our data yields a curve which decreases too quickly as shown in Fig. 5.9 and a quadratic behavior seems more appropriate. Such a behavior has been observed by other groups for YBCO films [137, 143, 144]. The physical origin for the change from linear to quadratic dependence may be attributed to the presence of scattering impurities in the samples leading also to a reduction of the ratio $\lambda_{ab}^2(0)/\lambda_{ab}^2(T)$ [143, 145]. From the experimental point of view, the temperature dependence of the penetration depth is thus probably not a straightforward criterion to prove or not the existence of a non-uniform superconducting gap in HTS.

Sample STO610 has basically two advantadges which render it particularly suited for a detailed analysis of the temperature dependence of the penetration depth. The first one is precisely what was discussed above, i.e. the saturation of the signal a few percent below the geometrical value V_{ss} allowing to look at the temperature dependence of λ_{ab} on a larger temperature interval than for samples STO472 and STO269. Sample STO607 would even be better than STO610 for this reason, but the second advantadge of STO610 is that its transition temperature is still above $70K$, thus offering again a large temperature interval to explore whereas sample STO607 becomes superconducting only below $\approx 48K$. The

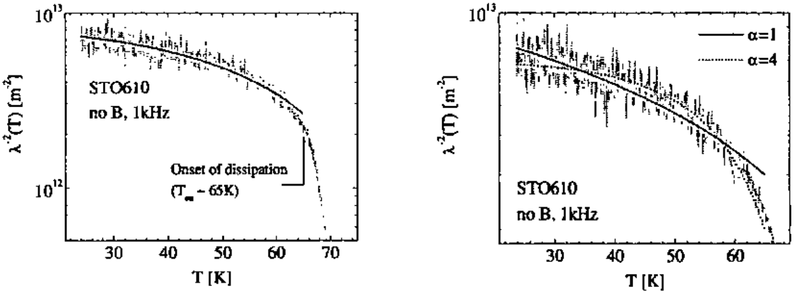

Figure 5.9: *Left: Inverse squared penetration depth as a function of temperature for STO610 in the absence of applied magnetic field. The line is a fit using Eq. (5.2) with* $\alpha = 2$. *We obtain* $\lambda_{ab}(0) \approx 3500Å$ *and* $T_c \approx 79K$. *Right: Zoom on the same data showing the behavior of the fit for* $\alpha = 1$ *and* $\alpha = 4$.

analysis of the other samples, and in particular of sample STO607, confirms a better agreement of the fits for $\alpha = 2$, yielding the values for the penetration depth reported in Table 5.2 below.

Sample	d [Å]	$T_{c0}[K]$	$\rho_N[\mu\Omega cm]$	$\lambda_{ab}(0)$ [Å]	$\lambda_{eff}(0)[\mu m]$
STO472	1100	~ 91	~ 150	2500 ± 400	1.1
STO269	~ 400	89.1	~ 300	2600 ± 400	3.2
STO610	48	73.7	265	3400 ± 250	48
STO607	24	48.3	350	5500 ± 100	250

Table 5.2: *Summary of some physical quantities for the different samples measured. Notation: d, film thickness determined by the deposition rate;* T_{c0}, *superconducting transition temperature;* ρ_N, *normal state resistivity;* $\lambda_{ab}(0)$, *GL penetration depth in zero magnetic field extrapolated to zero temperature;* $\lambda_{eff}(0)$, *effective penetration depth (thin film):* $\lambda_{eff} = 2\lambda_{ab}^2/d$.

We have seen in Sec. 4.2.2 that the saturation level of $Im(\delta V)$ at low temperatures depends on the penetration depth and the thickness of the sample. For a 1100Å thick sample with $\lambda_{ab}(0) = 2500$Å, the saturation level is less than 0.1% away from the geometrical value. From the values for the penetration depth obtained above, we can now estimate the saturation levels for the thinner films. Using $\lambda_{ab}(0) \approx 3400$Å and $\lambda_{ab}(0) \approx 5500$Å, we expect $Im(\delta V)$ to saturate respectively 3.3% and 15.3% below the geometrical value (the percentage is given by $(1 - Im(\delta V)/V_{ss})$. From the $Im(\delta V)$ data, we obtain respectively 2.2% and 15.6% at the same frequency of $1kHz$ for both samples, which is in reasonable agreement with the estimates calculated above.

5.2.1 Estimation of the percolation rate in the samples

A way to understand the relatively high values we obtain for the penetration depth might be percolation. Indeed, if a film is percolative, the conductivity will decrease and the sample will exhibit a larger penetration depth (λ^{-2} is proportional to the superfluid density and thus to the conductivity). If λ^0_{ab} is the value of the penetration depth which is not affected by percolation effects (homogeneous material) and λ^m_{ab} the measured value of the penetration depth, we expect the following behavior (see for example Ref. 146)

$$\left(\frac{\lambda^0_{ab}(T)}{\lambda^m_{ab}(T)}\right)^2 = \left(\frac{p-p_c}{1-p_c}\right)^\mu \tag{5.3}$$

where μ is the conductivity exponent, p_c the percolation threshold and p the percolation rate. To estimate the percolation rates, we consider here our films as two-dimensional for the percolation and assume a square geometry. For site percolation and using $\mu = 1.3$ [146] and $\lambda^0_{ab}(0) = 1500$Å, we obtain the values given in Table 5.3. The percolation threshold in this case is $p_c = 0.59$ [146]. This estimate, however, does not account for the 'natural' increase in $\lambda^0_{ab}(0)$ when T_c decreases as described by the so-called Uemura prediction: $T_c \propto \lambda^{-2}$ [147]. On the second line of the table, we give the percolation rates estimated for a value of $\lambda^0_{ab}(0)$ amplified by a factor $\sqrt{T_c^{bulk}/T_{c0}}$ ($T_c^{bulk} \simeq 92K$) for each film accounting for this correction which results in a slight decrease of the percolation effects for the thinner films.

Sample	STO472	STO269	STO610	STO607
percolation rate p	0.78	0.77	0.71	0.65
'Uemura corrected' p	0.78	0.77	0.73	0.68

Table 5.3: *Estimated percolation rates. The percolation threshold here is* $p_c = 0.59$

We obtain percolation rates which are 10% or more above the percolation threshold. The choice between bond or site percolation is not evident. We know that our samples are not constituted by disordered superconducting grains (which would imply Josephson weak links between the grains) but are well epitaxially grown. We may thus rather expect superconducting domains which are in direct contact with each other. Such a picture favours a description in terms of site percolation. Moreover, we look at these percolation effects in the zero temperature limit ($\lambda_{ab}(T=0)$) where, if the superconductor is granular, the coupling between the superconducting grains is maximum. This means that if bond percolation was essmed at high temperatures, site percolation may be more suited when $T \rightarrow 0$. For these reasons, we would here prefer a site percolation picture. The values we obtain show that such a description may, at least partly, account for the increase in the penetration depth in our films.

The question then arises whether percolation may affect the vortex dynamics in our samples. In fact, we may expect the percolation to induce a frequency dependence in the activation energy for the vortex system in the high temperature regime [148] above a crossover frequency given approximately by $\omega_c \approx 14 R_N k_B T/\phi_0^2$. Since in our case, we have typically $\omega_c \gtrsim 10^{10} Hz$ for all the samples, we do not expect relevant effects.

5.2.2 BKT prediction

Since we are dealing with very thin films, it may appear interesting to look at the Berezinskii-Kosterlitz-Thouless (BKT) prediction [49] applied to superconductors [50] for the thermally induced dissociation of vortex-antivortex pairs in a 2D system. At the melting temperature, we have

$$\frac{1}{L(T_{BKT})} = \frac{8\pi\epsilon_c k_B T_{BKT}}{\phi_0^2} \tag{5.4}$$

where $\epsilon_c = 1$ in the Kosterlitz-Thouless prediction and $1/L(T)$ corresponds in our case to the measured quantity $1/L_p(T)$.

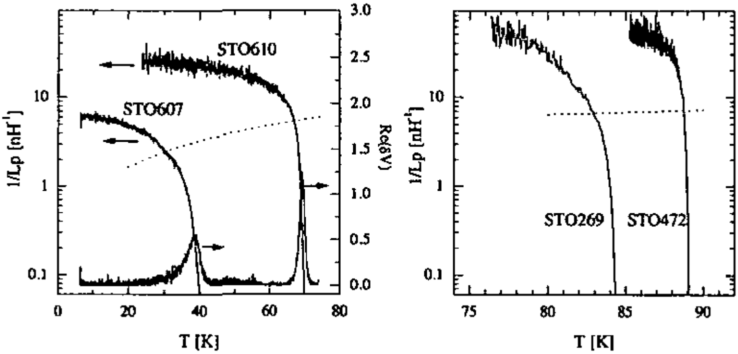

Figure 5.10: *Left: Inverse parallel inductance for the two thinner films, STO607 (24Å) and STO610 (48Å), as a function of temperature at a frequency of* $1.0kHz$. *On the plot is also shown the real (dissipative) part of the measured voltage* $Re(\delta V)$ *for both films in arbitrary units. Right: Inverse parallel inductance for the two thicker films as a function of temperature at the same frequency of* $1.0kHz$. *In both cases, the dotted line is the BKT prediction for* $\epsilon_c = 1$.

There is still a strong questioning about the existence of a true BKT transition in YBCO films, see for example Ref. 149 and references therein. There are some limitations which, a priori, make difficult the observation of such a transition in YBCO films [25]. The

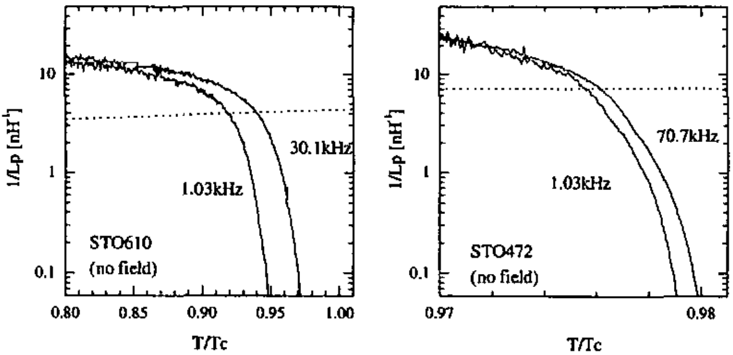

Figure 5.11: *Left: Inverse parallel inductance of sample STO610 as a function of temperature for two frequencies. The BKT prediction calculated for $\epsilon_c = 1$ is the dotted line. Right: Same plot for sample STO472 for two frequencies.*

first difficulty is to obtain an excellent homogeneity of the film, combined with a sheet resistivity of the order of a few $k\Omega$, making it formally possible to distinguish between the BKT transition governed by phase fluctuations of the order parameter and a usual superconducting transition driven by fluctuations of the amplitude of the order parameter [150]. Another problem is that percolation effects in the sample may lead to unwanted one-dimensional effects altering the transition. Finally, the presence of free (unbound) vortices producing dissipation in the sample may smooth the BKT jump and possibly push it to lower temperatures. It is thus clear that before claiming the existence of a true BKT phase transition in YBCO films, one must be very careful. Fig. 5.10 shows the inverse parallel inductance as a function of temperature at $1kHz$ for all samples. The BKT prediction is drawn for $\epsilon_c = 1$ (dotted line). We observe that the agreement of the curves with the BKT prediction is better for the thin films which seems reasonable. The frequency effect is shown for two films in Fig. 5.11.

According to the plots, the BKT scenario appears as a potential candidate, particularly for the thin films. However, it must be pointed out that no true jump is observed and that the curve starts to bend at temperatures lower than T_{BKT}. We interpret this behavior as a consequence of the presence of free (magnetic) vortices in the sample, causing a dissipation background and smoothing the transition. Since a strong magnetic field does not change deeply the shape of the transition, this encourages us to think that the magnetic vortices play a important role and probably give rise to a contribution to the sheet impedance which essentially dominates the overall response of the sample.

5.3 High temperature regime: pinned vortex liquid

The activated behavior of the data in the high temperature regime commends an interpretation of the vortex medium in terms of a pinned vortex liquid where the vortex motion is thermally activated (TAFF regime).

5.3.1 Peak in $Re(\delta V)$ as a function of frequency

As indicated in Fig. 5.5, the temperature T_p of the peak in $Re(\delta V)$ is located roughly at the end of the linear region observed in the Arrhenius plot of the resistance. Since we interpret this linear regime as characteristic of a vortex liquid, we may check that this is still the case down to T_p. At $T = T_p$, we have, in the presence of a magnetic field, $Re(\delta V) \simeq Im(\delta V) \approx 0.25V_{ss}$ as can be observed in Fig. 5.1. From Eq. (4.8), we can write $R_s \approx \omega\mu_0 h/x_m$. Knowing the expression for the resistance in the high temperature thermally activated regime allows to extract a prediction for T_p as a function of frequency. In the framework of the model where vortices execute an overdamped brownian motion in a sinusoidal pinning potential (see Sec. 2.5.2), we expect the resistance to be of the form $R = R_f I_0^{-2}(U(T,B)/k_BT)$, $R_f = R_N B/B_{c2}$ being the sheet flux flow resistance and I_0 the modified Bessel function of order zero which results essentially in an exponential of the form $e^{-U(T,B)/k_BT}$. Following the arguments of Sec. 2.3.3, we assume a linear temperature dependence of the activation energy $U(T,B)$ and we obtain [151]

$$T_p(\omega) = \frac{U_0(B)/k_B}{\frac{U_0}{k_BT_c} - ln(\omega/\omega_0)} \tag{5.5}$$

where $\omega_0 \approx R_f x_m/(\mu_0 h)$ and $U_0(B) = U(T=0,B)$. Fig. 5.12 shows two such plots of T_p versus frequency for samples STO472 at $B = 2.0T$ and for sample STO610 at $B = 0.1T$. The agreement of the data with the theoretical curve (dotted line) is reasonably good. To perform the fits, we fixed the value of T_c according to Table 3.5 and varied the values for $U(0,B)$ and ω_0. The activation energies $U(0,B)$ obtained from the fits, $3.3 \cdot 10^4 K$ and $6.3 \cdot 10^3 K$ for STO472 and STO610 respectively, are in agreement with the values inferred from the slope of the Arrhenius plots which are $2.9 \cdot 10^4 K$ and $5.9 \cdot 10^3 K$ respectively. This confirms our assertion that vortices are in a thermally activated regime at least down to T_p. The values for ω_0 obtained from the fits may be compared to the estimates one can do from Eq. (5.5) above. The fits yield $\omega_0 \approx 7.5 \cdot 10^{18} Hz$ and $\omega_0 \approx 6.5 \cdot 10^9 Hz$ whereas the estimates are $1.1 \cdot 10^8 Hz$ and $2.1 \cdot 10^8 Hz$ for STO472 and STO610 respectively. The huge value for ω_0 obtained from the fit should not be taken too seriously here since it enters in a logarithm in the expression. A decrease of T_c by five kelvins in the fitting expression decreases this frequency by a factor of 10^7.

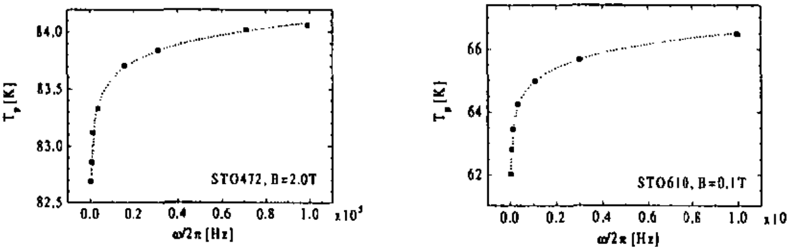

Figure 5.12: *Temperature* T_p *of the peak of* $Re(\delta V)$ *as a function of frequency for sample STO472 at* $B=2.0T$ *(left) and sample STO610 at* $B = 0.1T$ *(right). The dotted line is a fit using Eq. (5.5).*

5.3.2 Activation energy

We obtain the activation energy from the slope of the linear regime observed in the Arrhenius plot of the resistance at high temperatures, for each frequency and magnetic field. An example of such a plot is shown in Fig. 5.3. By varying the fitting region in order to extract the maximum slope in the Arrhenius plot of the resistance for each frequency, we deduce an upper estimate for the uncertainty of the activation energy of 5%.

We first plot, in Fig. 5.13, the values for the activation energies at two different magnetic fields for all the samples as a function of the thickness d and the transition temperature T_{c0}. The values we observe are in agreement with those inferred from other works on multilayers or YBCO films [152–155].

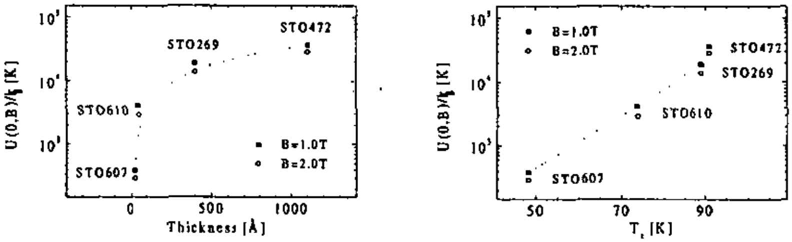

Figure 5.13: *Activation energy for the four films measured plotted as a function of sample thickness (left) and* T_c *(right) for two different magnetic fields. The dotted lines are guides to the eye.*

Fig. 5.14 shows the activation energy as a function of the magnetic field for samples STO472 and STO269 in a log-log plot (left). Linear fits provide a satisfactory description of the behavior of both samples and we obtain slopes of -0.40 (STO472) and -0.47 (STO269), indicating a magnetic field dependence of the activation energy $U(0,B) \propto B^{-0.40}$ and $U(0,B) \propto B^{-0.47}$ for samples STO472 and STO269, respectively. A lin-log plot of the activation energy for sample STO472 shows the poorer agreement of the data with a magnetic field dependence of the form $U(0,B) \propto ln(B)$.

This magnetic field dependence of the activation energy for the thick samples can be considered as compatible with the picture where the energy barriers U_{pl} for the vortex motion are associated with a thermally activated plastic motion of the vortex structure as described in Sec. 2.3.3. Using the penetration depths $\lambda_{ab}^{472}(0) \approx 2500$Å and $\lambda_{ab}^{269}(0) \approx 2600$Å obtained in Sec. 5.2, we can estimate a value for the prefactor $U_{pl}(T=0,B=0)$ in the expression for $U_{pl}(T,B)$. We obtain $U_{pl}(0,0) \approx 2.6 \cdot 10^4 K$ and $U_{pl}(0,0) \approx 2.4 \cdot 10^4 K$ for samples STO472 and STO269 respectively. The fits yield, for STO472 and STO269, $U_{pl}(T=0,B=0) \approx 3.7 \cdot 10^4 K$ and $U_{pl}(T=0,B=0) \approx 1.9 \cdot 10^4 K$ which is in quantitative agreement with the estimates. Forcing a $B^{-0.5}$ dependence for the fits, we obtain the values $U_{pl}(0,0)_{fit} \approx 2.9 \cdot 10^4 K$ and $U_{pl}(0,0)_{fit} \approx 1.8 \cdot 10^4 K$ for samples STO472 and STO269. Equivalently, we can deduce the in-plane penetration depth for both samples and, using the values from the fit forcing a $B^{-0.5}$ dependence, we obtain $\lambda_{ab}^{472}(0)_{fit} \approx 2400$Å and $\lambda_{ab}^{269}(0)_{fit} \approx 3000$Å for samples STO472 and STO269 respectively. The picture adopted to describe the vortex activation process in the thick films at high temperatures appears thus reasonable.

We turn now to the thinner films and start with sample STO610. As can be observed in Fig. 5.15, the activation energy shows a clear crossover in its magnetic field dependence at about $1.0T$. In the high field regime, a power law fit yields a $B^{-0.58}$ dependence, whereas in the low field regime, the dependence is $B^{-0.13}$. The value for the exponent in the high field regime is again relatively close to -0.5 and we assume a plastic motion of the vortices with the activation energy given by Eq. (2.46). A fit of the data to a $B^{-0.5}$ dependence, yields a prefactor value $U_{pl}(0,0)_{fit} \approx 4.6 \cdot 10^3 K$, whereas the numerical value calculated by means of Eq. (2.46) is $U_{pl}(0,0) \approx 1.4 \cdot 10^4 K$. The value $U_{pl}(0,0)_{fit} \approx 4.6 \cdot 10^3 K$ corresponds to a penetration depth $\lambda_{ab}(0)_{fit}^{610} \approx 6000$Å which is somewhat higher than the value of 3400Å obtained previously for sample STO610. The behavior observed in the low field regime does not correspond any more to the same picture and we rather propose to fit the data using Eq. (2.44) which gives the characteristic energy for plastic deformations of a 2D vortex lattice. We thus attribute the crossover observed in the magnetic field dependence of the activation energy to a *dimensional crossover* from a 3D vortex medium at high magnetic fields to a 2D vortex medium at low magnetic fields. We shall justify this assumption below. From Eq. (2.44), we thus expect a $ln(B)$ dependence of the activation energy in the low field regime for sample STO610. Fig. 5.15 (right) shows a lin-log plot of the activation energy where we can observe a good agreement of the data with the expected logarithmic behavior. However, the quality of the power law fit $U(0,B) \propto B^{-0.13}$ is not really worse than the fit $U(0,B) \propto ln(B)$. Therefore, even if the latter dependence appears better suited for physical reasons, a power law dependence cannot be excluded on the basis of the data for sample STO610. This ambiguity is erased once we look at the data for sample STO607 in Fig. 5.16. Indeed, we see that a power law fit provides a poorer agreement with the data than a logarithmic fit, confirming the picture that the vortex medium appears essentially 2D in sample STO610 at low fields and over the whole magnetic field range in sample STO607. From the fits, we obtain $U_{pl}(0,0) \approx 720K$ and $U_{pl}(0,0) \approx 140K$ for samples STO610 (low fields) and STO607 respectively. Numerical estimates using Eq. (2.44) yield, respectively, $U_{pl}(0,0) \approx 65K$ and $U_{pl}(0,0) \approx 12K$.

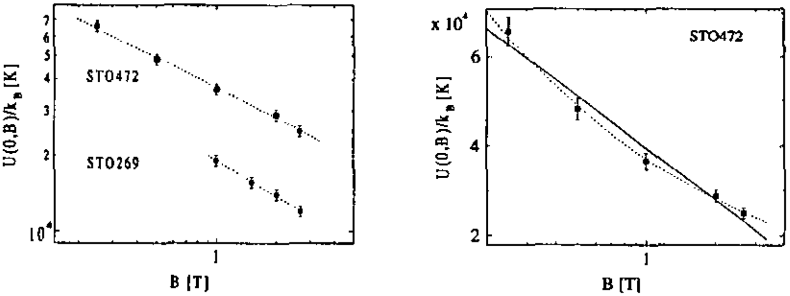

Figure 5.14: *Log-log plot (left) and lin-log plot (right) of the activation energy for samples STO472 and STO269 as a function of magnetic field. The dotted line in the right plot is the curve for a power law dependence of $U(0,B)$ versus B as drawn in the left plot.*

We shall point out that, if we use the same basic energy scale as obtained for the 3D case, i.e. $2\epsilon_0 ln(\lambda_{ab}/\xi_{ab})$ instead of ϵ_0, we would have to amplify the values calculated above by a factor ~ 9.2 which would yield approximately $600K$ and $110K$ for STO610 and STO607 respectively, in better agreement with the observed values. It thus appears that a precise estimate for the value of the activation energy in our films would require a better knowledge of the exact structure of the vortex lattice defects. The important point here is that the activation energy for the 2D case is expected to depend on the thickness and the penetration depth of the sample according to $U(0,B)^{2D}_{pl} \propto d/\lambda^2_{ab}(0)$. This means that the ratio of the slopes obtained in the lin-log plot of the activation energy for samples STO610 (low fields) and STO607 should be equal to the ratio $d^{610}\lambda^2_{ab}(0)^{607}/(d^{607}\lambda^2_{ab}(0)^{610})$ calculated with the appropriate values for d and $\lambda_{ab}(0)$. The ratio of the slopes equals 5.1 whereas the ratio given by the expression right above yields 5.2 which is quite satisfying. We now propose an argument which gives further support to the picture of a dimensional crossover of the vortex medium in our films as discussed above. We have seen in Sec. 2.2.2 that a vortex pulled away from its equilibrium position is distorted over a typical length l_z^{opt} determined by the elastic properties of the flux lattice. Such a distortion is possible as

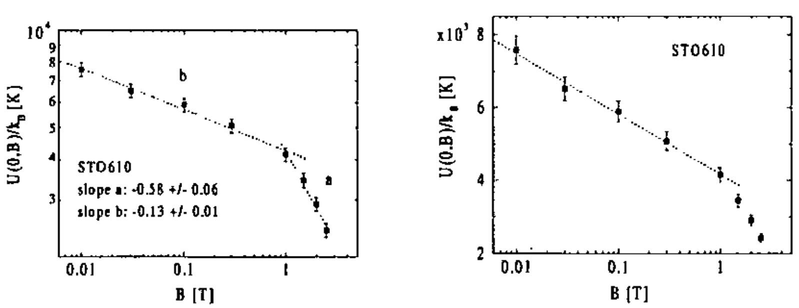

Figure 5.15: *Log-log plot (left) and lin-log plot (right) of the activation energy as a function of magnetic field for sample STO610.*

long as the thickness of the film is larger than l_z^{opt}. Once $d \lesssim l_z^{opt}$, the vortices appear much stiffer and a vortex pulled away from its equilibrium position will not bend since it is not energetically favorable. This means that, as long as $d \gtrsim l_z^{opt}$, we have *soft* vortices which may entangle and reconnect with each other, whereas for $d \lesssim l_z^{opt}$, we have *stiff* vortices appearing essentially as rigid rods. In the former case, the vortex medium appears as 3D whereas it exhibits 2D features in the latter case. Such a crossover will occur for a film thickness somewhat smaller than l_z^{opt}, say $d = l_z^{opt}/2$. Taking $l_z^{opt} \approx a_0/\gamma$, we obtain a crossover field $B_{cr} \approx 0.9T$ for sample STO610 using $\gamma = 5$ in good agreement with what we observe in the activation energy behavior.

It is interesting to come back here to the short discussion of Sec. 5.1.3 about the entanglement temperature estimated for the vortices in our samples. According to the numerical estimates, we can expect that, for the thick films, the flux lines will entangle and reconnect in the high temperature regime ($T \gtrsim T_p$), at least for fields of about $1.0T$. This corresponds pretty well to what we observe in the above plots for the thick films, since the energy barrier used to describe the thermally activated vortex motion is a reconnection barrier. As the thickness of the sample decreases, the entanglement of the flux lines appears at a temperature much closer to T_{c0} and can be larger than T_p, meaning that we have to expect different mechanisms for the vortex motion in the high temperature regime and thus different energy barriers. Again, this corresponds reasonably well to what we measure since we observe different energy barriers in the thin films. It thus appears natural to wonder if the crossover in the behavior of the activation energy does mark the beginning of the entanglement of the flux lines in sample STO610. An estimate of the crossover field above which an entanglement of the flux lines is expected for sample STO610 yields $B_{ent} \approx 8.0T$ at a temperature $T = T_p$ situated in the TAFF regime. We see that this value is somewhat high when we compare it to the observed crossover field

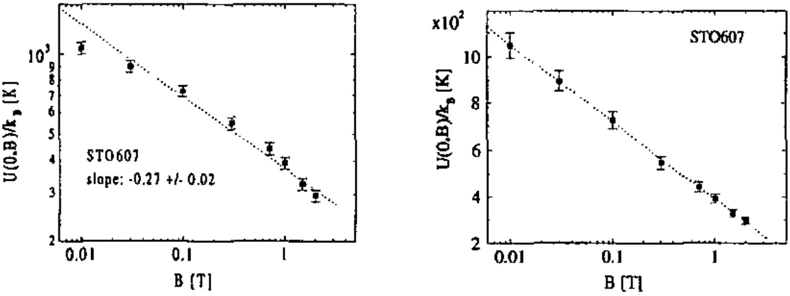

Figure 5.16: *Log-log plot (left) and lin-log plot (right) of the activation energy as a function of magnetic field for sample STO607.*

of $1.0T$.

If one believes in the numerical estimates performed, it appears possible that the vortices in the high field regime are no longer rigid rods, but are not yet entangled as they appear in the thick samples. This means that we are not yet allowed to consider the energy barrier as a reconnection barrier in this high field regime, which may explain the discrepancy between the calculated and observed values for the activation energy. We thus think that a double-kink mechanism is not really suited for explaining the vortex motion in the high field regime for sample STO610 although we do not know what type of lattice defects should be considered in this case.

We shall keep in mind that the numerical values proposed above for the crossover fields and entanglement temperatures remain estimates and are not exact. The expressions used involve prefactors which affect the numerical estimates, depending on the approximations done. Nevertheless, we think that a description for the crossover field, based on the comparison of the thickness d of the sample and the typical length l_z^{opt} for the distortion of a flux line is reasonable. We thus interpret the observed crossover as a smooth borderline marking the difference between stiff vortices (2D) at low fields and soft vortices (3D) at high fields.

5.4 Vortex glass to vortex liquid phase transition

The question of the existence of a true thermodynamic phase transition to a vortex glass phase at low temperatures is addressed here using the predictions of the vortex glass theory proposed by Fisher *et al.* [11]. The sheet impedance follows from the expression given in Sec. 2.4.3 for the conductivity and can be written

$$Z_s(\omega) = R_s + i\omega L_s = Z_0\left(\frac{\xi_{vg0}}{\xi_{vg}}\right)^{z+2-D} \mathcal{S}_{\pm}^{-1}(\omega\tau_{vg}) \tag{5.6}$$

Writing $\tilde{\omega} = \omega\tau_{vg} = \omega\tau_{vg0}|1 - T/T_g|^{-\nu z}$, we can rescale the sheet impedance $Z_s \to \tilde{Z}$ in oder to obtain

$$\tilde{Z}(\tilde{\omega}) = \frac{Z_s}{Z_0}|1 - T/T_g|^{-\nu(z+2-D)} = \mathcal{S}_{\pm}^{-1}(\tilde{\omega}) \tag{5.7}$$

where $\mathcal{S}_{\pm}^{-1}$ is a universal function. This means that the plot of the scaled sheet impedance $\tilde{Z}$ as a function of the scaled frequency $\tilde{\omega}$ for different frequencies, magnetic fields or samples should fall on a universal curve defined by the function $\mathcal{S}_{\pm}^{-1}(\omega\tau_{vg})$ [156–159]. In order to check the existence of such a universal behavior in the data for the complex sheet impedance obtained from our films, we have performed a dynamical scaling analysis of our data for samples STO269 and STO472 for $D = 3$, since we expect the vortex medium to be essentially three-dimensionnal in these samples.

Setting $\tilde{Z} = \tilde{R} + i\tilde{\omega}\tilde{L}$, we can write the scaled resistance and inductance in the form

$$\tilde{R} = R_s|1 - T/T_g|^{-\nu(z+2-D)} \tag{5.8}$$

$$\tilde{L} = L_s|1 - T/T_g|^{-\nu(2-D)} \tag{5.9}$$

and the corresponding relations for the magnitude and phase angle of the impedance

$$\tilde{Z} = |Z_s||1 - T/T_g|^{-\nu(z+2-D)} \tag{5.10}$$

$$\tilde{\Phi} = \Phi = \arctan(\omega L_s/R_s) \tag{5.11}$$

The analysis consists in finding a set of three parameters T_g, ν and z which produce the best collapse of the scaled quantities onto a single universal curve. Fig. 5.17 shows the plots for the scaled resistance (left) and inductance (right) as a function of the scaled frequency for sample STO472 at $B = 0.5T$. The same plot for $B = 2.0T$ is shown in Fig. 5.18. The data for eight frequencies do collapse on the same universal curve for the critical exponents values $\nu = 2.0$ and $z = 6.0$. The same behavior is observed for sample STO269 [158] with similar critical exponents. From the scaling analyses, we estimate uncertainties of ±0.5 and ±1.0 on the exponents ν and z respectively. The values for the critical exponents found here are in agreement with those inferred from other works on thin films [156, 160] but larger than the values found in single crystals [129, 157, 161].

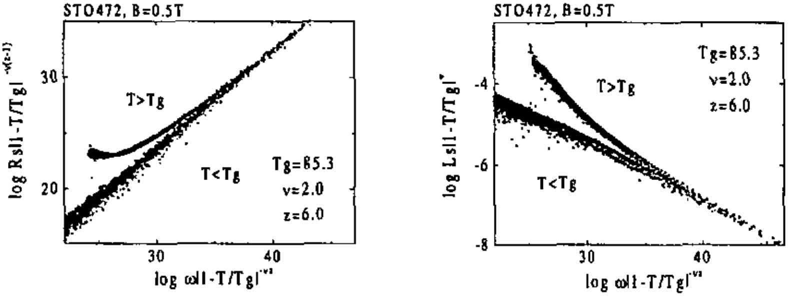

Figure 5.17: *Scaled resitance (left) and inductance (right) for eight different frequencies as a function of the scaled frequency for sample STO472 at* $B = 0.5T$.

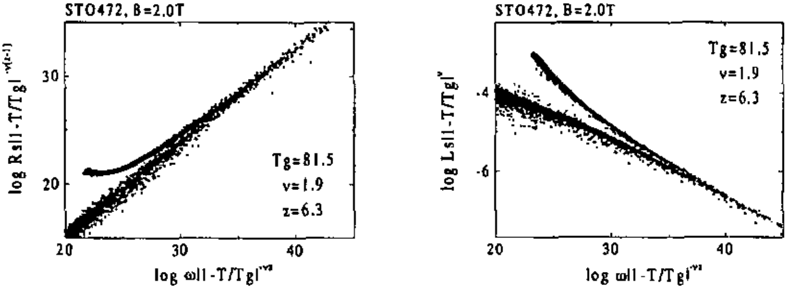

Figure 5.18: *Scaled resitance (left) and inductance (right) for eight different frequcncies as a function of the scaled frequency for sample STO472 at* $B = 2.0T$.

Finding the values for the critical exponents and the temperature T_g implies to test the collapsing of the data by varying systematically the three parameters. One problem in this procedure arises from the difficulty to estimate quantitatively the quality of the collapse with a precise mathematical criterium, since the universal function behavior is only known in the limits $\tilde{\omega} \to 0$ and $\tilde{\omega} \to \infty$.

The predictions of the vortex glass model help to define a lookup domain for each parameter. We may for instance test the specific behavior of the resistance above T_g and of the inductance below T_g as predicted by the model. We have [7, 120]

$$R_s(T) \propto (T-T_g)^{\nu(z-1)} \quad T > T_g \tag{5.12}$$
$$L_s(T) \propto (T_g-T)^{\nu} \quad T < T_g \tag{5.13}$$

It is however difficult to define precisely the range in temperature where these predictions are valid [120] which renders this analysis somewhat uncertain. A solution might consist in plotting the quantity $(\partial lnR/\partial T)^{-1}$ as a function of temperature which should produce a straight line extrapolating to zero at T_g with a slope $(\nu(z-1))^{-1}$ as performed by Gammel *et al.* [162, 163]. However, the necessity to smooth the data and perform a numerical differentiation again affects the reliability of such a plot in our case. The predicted behavior of the different physical quantities of the system in the limit $T \rightarrow T_g$ or, equivalently, $\tilde{\omega} \rightarrow \infty$, will be more helpful for the determination, or for a consistency check, of the values for the three parameters relevant for the scaling analysis.
The behavior of the resistance and the inductance, in particular, follows from the asymptotic behavior of $S_{\pm}^{-1}(\tilde{\omega})$ in the limit $T \rightarrow T_g$ and we obtain, for $D = 3$,

$$R_s(T=T_g) \propto \omega^{(z-1)/z} \tag{5.14}$$
$$L_s(T=T_g) \propto \omega^{(-1)/z} \tag{5.15}$$

By plotting the isotherms of the resistance and the inductance as a function of the frequency as shown in Fig. 5.7, we can extract the slopes s_R and s_L of both quantities and plot them as a function of temperature (Fig. 5.19). It is then straighforward to see from Eqs. (5.14) and (5.15), that the quantities $1/(1-s_R)$ and $-1/s_L$ should provide a value for the dynamic critical exponent at $T = T_g$. Fig. 5.19 (left) shows the slopes of the isothermal lines for the resistance and the inductance for sample STO472 at a magnetic field of $B = 0.5T$. The quantities $1/(1-s_R)$ and $-1/s_L$ are plotted on the right-hand side of the figure. The problem arising here is that both curves for the value of the critical exponent z do not allow to determine univocally one pair $(T_g; z)$ since they do not cross or coincide at a given temperature. What we can deduce is a temperature range for the value of T_g by setting $4 < z < 7$ as predicted in [11]. As can be observed on the plot, a typical value for T_g would be $T_g \approx 85.5K$. From the scaling analysis performed above, we had $T_g = 85.3K$ and $z = 6.0$.
In the limit $T \rightarrow T_g$, the phase angle of the impedance $\Phi(\omega) = \arctan(\omega L_s(\omega)/R_s(\omega)) = \tilde{\Phi}(\tilde{\omega})$ is expected to reach the value [11, 68]

$$\Phi(T=T_g) = \frac{\pi}{2}\frac{z+2-D}{z} \tag{5.16}$$

This has the consequence that the curves for the phase angle as a function of (T/T_g-1) are expected to converge or even cross at $T = T_g$ at a phase value of $\pi(z-1)/2z$ independently of the magnetic field or the frequency. Since T_g does not depend on the frequency, this behavior is also expected directly in a plot of the phase angle as a function of temperature.

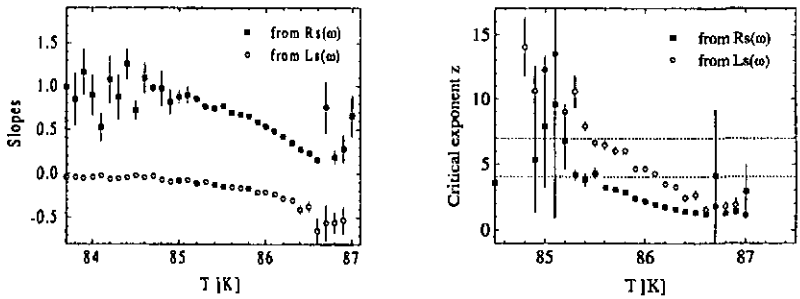

Figure 5.19: *Slopes of the isotherms for $R_s(\omega)$ and $L_s(\omega)$ for sample STO472 at $B = 0.5T$ (left) and dynamic critical exponent obtained from these slopes as a function of temperature (right). The dotted lines indicate the theoretical limits for the value of z.*

Plots of the phase angle are shown in Fig. 5.20 where we draw Φ for different magnetic fields (left) and frequencies (right) for sample STO472. The curves do converge as one approaches T_g but do not exhibit a clear crossing at $T = T_g$. Nevertheless, we can extract a value for z from these plots which can be compared to the value obtained in the scaling analysis or, assuming again, as a first approximation, a value for z verifying $4 \lesssim z \lesssim 7$, we can deduce a temperature range for T_g from the plot of the phase angle for different frequencies (Fig. 5.20, right). We obtain in this particular case $85.5K \lesssim T_g \lesssim 86.0K$, which is a bit higher than the value $T_g \approx 85.3K$ obtained in the scaling analysis. Using this value for T_g in the plot for the phase at various magnetic fields, we obtain $z \approx 13$, which is too large. We see here that this type of analyis requires some compromise for the scaling parameters since, satisfying all the predictions for the behavior of the data with exactly the same scaling parameters appears somewhat non-trivial.

An interesting prediction of the vortex-glass theory concerns the frequency behavior of the irreversibility temperature. The frequency-dependent onset of the irreversible effects is marked in our system by the deviation of the data from the high-temperature linear part in the Arrhenius plot of the resistance. As shown in Fig. 5.5, the temperature $T_p(\omega)$ of the peak in $Re(\delta V)$ is located at the end of the TAFF regime and thus provides a reasonable approximation for the irreversisbility temperature of the the vortex medium in our films. In a system presenting some glassiness, we expect the irreversibility temperature to coincide with T_g in the limit $\omega \to 0$. For $D = 3$, the prediction of the scaling model reads

$$(T_{irr}(\omega) - T_g) \propto \omega^{1/(\nu(z-1))} \tag{5.17}$$

We report the curves for $(T_p(\omega) - T_g)$ as a function of frequency in Fig. 5.21 and indicate

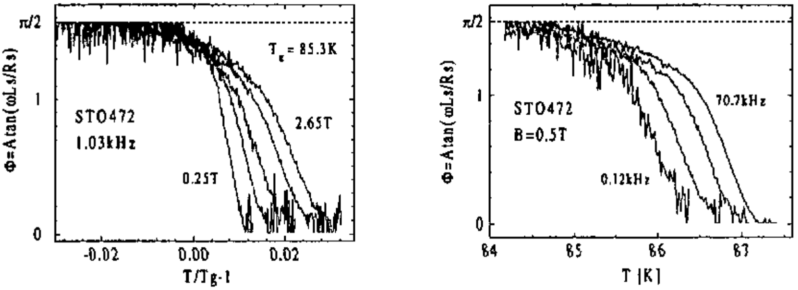

Figure 5.20: *Left: Phase angle of the impedance as a function of the normalized temperature* $(T/T_g - 1)$ *for sample STO472 at five different magnetic fields:* $0.25T, 0.5T, 1.0T, 2.0T$ *and* $2.65T$*. Right: Phase angle as a function of temperature for sample STO472 at four frequencies:* $0.12kHz, 1.03kHz, 10.7kHz$ *and* $70.7kHz$.

the values for the product $\nu(z-1)$ obtained from the inverse slope of the data. This allows another consistency check of the critical exponents values once the transition temperature is known. We obtain $\nu(z-1) \simeq 9.1$ at $B = 0.5T$ and $\nu(z-1) \simeq 8.8$ at $B = 2.0T$ whereas we find $\nu(z-1) \simeq 10.0$ at $B = 0.5T$ and $\nu(z-1) \simeq 10.1$ at $B = 2.0T$ from the scaling plots.

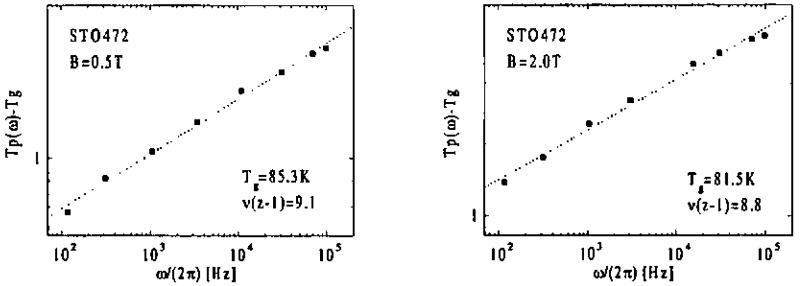

Figure 5.21: *Frequency dependence of the difference* $(T_p(\omega) - T_g)$ *for sample STO472 at magnetic fields values* $B = 0.5T$ *(left) and* $B = 2.0T$ *(right). The inverse slope of the linear fit (dotted line) provides a value for the quantity* $\nu(z-1)$.

Table 5.4 below summarizes the values for the critical exponents and transition temperatures T_g obtained from the analysis described in this section for samples STO472 and STO269.

The case of a 2D vortex medium

We have seen in Sec. 2.4.1 that a 2D vortex medium will not form a vortex-glass phase as long as $T > 0$, meaning that $T_g^{2D} = 0$ once dislocations are present in the vortex system. The absence of a vortex-glass phase at non-zero temperatures in very thin films was claimed by different groups [164,165]. It appears thus interesting to perform a scaling analysis of the data for sample ST610 in order to check whether we observe a collapse of the data or not. On the basis of the analysis done in the high temperature regime, we would, a priori, expect a difference between the behavior of the data at *high fields* ($B \gtrsim 1.0T$) and at *low fields*. What should in particular appear is a difficulty to produce a scaling with the low fields data. Astonishingly, we observe in Fig. 5.22 that, for the set of parameters $T_g = 64K$, $\nu = 2$ and $z = 6$, the data for sample STO610 at $0.01T$ tend to collapse as observed for the thick samples. This appears surprising since dislocations in the vortex lattice are certainly present, meaning that we would expect $T_g = 0$ if the vortex medium is 2D. And on the basis of the analysis of the data done in the high temperature regime, the vortex medium appears 2D in sample STO610 at $B = 0.01T$. We shall discuss this point in the next section.

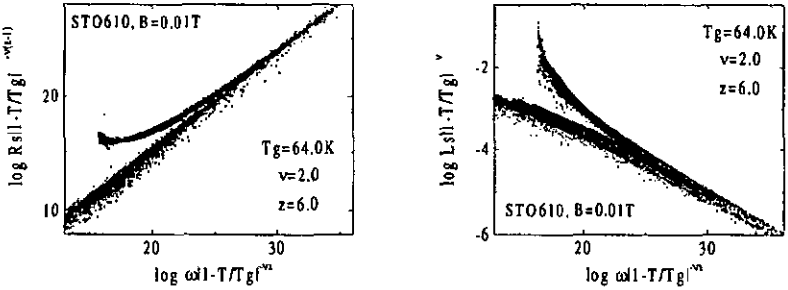

Figure 5.22: *Scaled resitance (left) and inductance (right) for six different frequencies as a function of the scaled frequency for sample STO610 at* $B = 0.01T$.

Summary

The scaling analysis performed in this section provides good evidence for the existence of a vortex glass to vortex liquid phase transition in our thick films STO269 and STO472.

The values for the critical exponents found above are in reasonable agreement with the values found in the literature for thin films [161, 166–169]. We have seen, however, that the analysis is complex and allows several checks for the values of the scaling parameters. Fullfilling all the predictions represents the main difficulty of the analysis and some discrepancy appears between the results from the resistance and the inductance, see Table 5.4.

A scaling analysis performed with the data for sample STO610 shows that we can achieve a collapse of the data with similar critical exponents like for the thick samples, although we would expect it impossible, at least at low magnetic fields since the vortex medium appears there essentially 2D. This raises the question of the interpretation of such a scaling analysis.

	B [T]	Scaling Analysis			R_s and L_s at T_g	
		$T_g[K]$	ν	z	z	z
STO269	1.00	77.6	2.0	6.2	5.1	8.1
	1.50	76.4	2.0	5.5	3.8	6.6
	2.00	74.3	2.1	5.8	4.5	7.1
	2.65	73.4	2.0	5.5	3.6	5.4
STO472	0.25	86.6	1.8	6.6	3.8	7.2
	0.50	85.3	2.0	6.0	4.2	9.5
	1.00	83.7	1.8	6.7	3.4	7.4
	2.00	81.5	1.9	6.3	3.9	6.2
	2.65	80.2	2.0	6.0	3.1	7.1

Table 5.4: *Phase transition temperature T_g and critical exponents ν and z as obtained from the scaling analysis. The dynamic critical exponent z obtained from the slopes of the isotherms of R_s and L_s is also reported.*

5.5 Phase diagram and discussion

On the basis of the analyses performed in the previous sections, we can sketch a $B-T$ phase diagram for our films as shown in Fig. 5.23 and Fig. 5.24 for samples STO472 and STO610. In Fig. 5.23, we plot, for two frequencies, the temperature T_p of the peak in $Re(\delta V)$, which can be essentially identified as the frequency dependent irreversibility temperature of the vortex medium. This is justified since $T_p(\omega)$ marks approximately the beginning of the deviation from the linear behavior in the Arrhenius plot of the resistance thus defining the onset of the irreversible effects in the vortex system. The frequencies are $98.8kHz$ (circles) and $1.03kHz$ (triangles). We can observe that, as the frequency decreases, the onset temperature for the irreversible effects in the vortex medium decreases also, which is reasonable. If a vortex-glass phase builds up at low temperatures, we expect this irreversibility line to turn into a melting line in the limit $\omega \to 0$ as expressed by Eq. (5.17). Since we could deduce numerical values for $T_g(B)$ from the scaling analysis, we plot here these values (squares) which form a line seperating the vortex-liquid phase from the vortex-glass phase. It is interesting to perform a fit to this line using an expression for the melting line based on the Lindemann criterion as described in Sec. 2.2.4. Using Eq. (2.32) where we assume $\gamma = 5$, $\lambda_{ab}/\xi_{ab} = 100$ and impose $\lambda_{ab}(0) = 2500\text{Å}$ as found previously in Sec. 5.2, we obtain $c_L \approx 0.08$ and $c_L \approx 0.07$ for samples STO472 and STO269, respectively, which is not far away from the expected value, typically between 0.1 to 0.2.

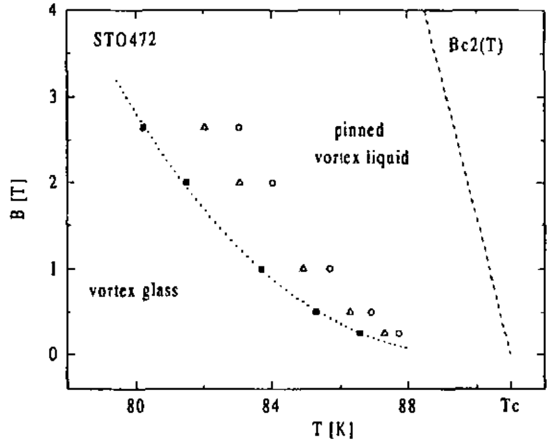

Figure 5.23: *Phase diagram for sample STO472. We plot $T_p(\omega, B)$ for $\omega/2\pi = 98.8kHz$ (circles) and $\omega/2\pi = 1.03kHz$ (triangles). These lines mark essentially the frequency dependent onset of the irreversible behavior of the vortices in the film. The squares are the values for $T_g(B)$ as obtained from the scaling analysis and represent the melting line of the vortex medium. The dotted line is a fit to this melting line using Eq. (2.32).*

The phase diagram for sample STO610 is shown in Fig. 5.24. We plot $T_p(\omega)$ for $\omega/2\pi = 30.1kHz$ and $\omega/2\pi = 1.03kHz$ which, again, mark the borderline between the reversible and irreversible behavior of the vortex medium for a given frequency. The horizontal dotted line indicates the dimensional crossover of the vortex medium as determined from the behavior of the activation energy as a function of the magnetic field. We do not plot here a melting line since we do not know whether a melting temperature does exist or not. We may extract a melting temperature from a scaling analysis as done for the thick samples where the vortex medium is clearly 3D. However, that would not make much sense since we expect $T_g = 0$ for a 2D vortex medium. What does a non-zero value for T_g mean when it is extracted from a scaling analysis of the low fields data from sample STO610 where the vortex structure is precisely expected to be 2D? We have to understand what happens here.

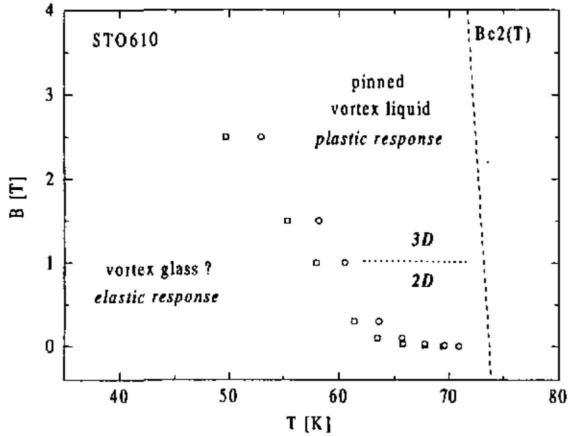

Figure 5.24: *Phase diagram for sample STO610. As in the phase diagram for sample STO472, we plot $T_p(\omega, B)$ for $\omega/2\pi = 30.1kHz$ (circles) and $\omega/2\pi = 1.03kHz$ (squares). The dotted line indicates the dimensional crossover of the vortex structure observed in the high temperature regime.*

It is certainly important at this point to emphasize the fact that we are looking at the dynamic properties of the vortex system. The probing frequency at which the response of the system is measured determines a time window for the processes that may be observed, depending on their characteristic time scales. Let us estimate the time scale τ_t for short-scale elastic deformations of the vortex lattice. This time scale is given by $\tau_t = \eta/(c_{66}q^2)$ [21] where q is the typical wavevector for the deformation, c_{66} is the elastic shear modulus and $\eta = \phi_0^2/(2\pi\xi^2\rho_N)$, the viscosity of the vortex medium. Calculating τ_t $q = \pi/a_0$, we obtain $\tau_t = 8\mu_0\lambda_{ab}^2 a_0^2/(\pi^2\rho_n\xi_{ab}^2) \approx 10^{-11}s$ at $B = 1.0T$, using $\rho_n = 150\mu\Omega cm$ and $\lambda_{ab}/\xi_{ab} = 100$. In this case, the response time of the vortex system is much shorter than our experimental probing frequencies ($10^2Hz - 10^5Hz$). This estimate holds essentially for a vortex solid but is not true any more in the case of a very viscous liquid, which

is characterized by two time scales, τ_t and τ_{pl}, where τ_{pl} is the charactcrisitc time scale for plastic deformations in the medium. Associating an energy barrier U_{pl} for the plastic deformations of the vortex structure, the time τ_{pl} can be written $\tau_{pl} = \tau_t e^{U_{pl}/k_B T}$ [21]. Due to the exponential factor entering its expression, this characteristic time can become much larger than our probing frequencies for energy barriers of a few thousand Kelvins as we observe them. This means that, depending on the time scale at which the vortex structure is investigated, we may ($\omega^{-1} > \tau_{pl}$) or may not ($\omega^{-1} < \tau_{pl}$) observe the plastic deformations of the vortex system. We may thus be convinced to observe a vortex solid whereas we in fact do observe a viscous liquid which appears frozen at our experimental time scales. Since we do observe a slowing down of the dynamics in the low temperature phase, where the frequency dependence of the sheet impedance is very similar to what is expected for a vortex-glass phase, this may explain why a scaling analysis does provide some evidence for the existence of a phase transition between a vortex-liquid phase and a vortex-glass phase, even in the absence of a true vortex-glass phase.
It may thus appear interesting to describe the flux-line lattice in our films as a viscoelastic medium where the frequency effects described above appear naturally. This is what we try to do in section 5.7. However, before doing this, we suggest in the section below to interpret the observed slowing down of the vortex dynamics as a consequence of the collective pinning of the vortices at low temperatures.

5.6 The ‘frozen’ vortex liquid

In this section we propose an interpretation of the low temperature behavior of the vortex medium in our films in terms of the collective pinning picture. We stress again the importance of remembering that the vortex system is not only investigated at certain temperatures and vortex densities but also at certain time scales determined by the probing frequency ω.

5.6.1 Usual crystal and 2D vortex medium

A perfect crystal made up of atoms or molecules is a solid. A real crystal however is never perfect and, in the rigorous sense of the word, is no longer a solid. At any non-zero temperature, a real crystal will embody a finite density of point-like defects (vacancies, interstitials) with non-zero mobility thus providing the possibility for mass flow in the crystal. From a practical point of view, it is clear that most crystals behave as solids because the time scales.at which the plastic flow mediated by point-like defects takes place are by far much larger than the life time of the real crystal itself.

The situation in a two-dimensional vortex system is in some sense quite similar. We have seen in Sec. 2.4.1 that the existence of a vortex-glass phase in a two-dimensional superconductor is in the rigorous sense impossible ($T_g = 0$). The random pinning potential can indeed quench the motion of a 2D vortex medium as a whole, as it does in the 3D case. But flux transport in a 2D case can be provided by the motion of thermally nucleated dislocation pairs (topologically equivalent to point defects for the smallest pairs of extension $\sim a_0$) which are present as soon as $T > 0$ thus making a two-dimensional vortex-glass phase impossible at any non-zero temperature. The question is then: what is the characteristic timescale τ_m for such defects to move in the vortex medium and how does it compare to the time scale at which the system is probed ? Quite clearly, the use of a large probing time scale ($\omega^{-1} \gg \tau_m$) will lead the experimentalist to deduce that the vortex medium behaves as a liquid of vortices since moving dislocations will produce flux transport. However at much smaller time scales ($\omega^{-1} \ll \tau_m$), the quenching of vortex motion due to disorder will be the dominant feature governing the response of the vortex system. The system may then exhibit a glassy behavior if the vortices are collectively pinned, as we shall see in the next section.

5.6.2 Dynamic response

One important consequence of the divergence of the energy barriers for vortex motion in a vortex-glass phase is the fact that vortices become immobile so that the linear resistance can go to zero. It is thus important to know how the position of a vortex changes as a function of time. The temporal vortex autocorrelation function can be written

$$C_v(t) \equiv \langle\langle\vec{r}_i(t)\cdot\vec{r}_i(0)\rangle_t - \langle\vec{r}_i(t)\rangle_t^2\rangle_d = \langle\langle\vec{u}_i(t)\cdot\vec{u}_i(0)\rangle_t\rangle_d$$

where $\vec{r}_i(t) = \vec{R}_i + \vec{u}_i(t)$, $< \ldots >_t$ denotes an average over time and $< \ldots >_d$ denotes an average over disorder. $\vec{R}_i$ is the position of the *ith* vortex in an ideal Abrikosov lattice and $\vec{u}_i(t)$ is the displacement of the same vortex from its ideal position due to thermal fluctuations and disorder (pinning).

If we adopt the classical creep description for the vortex motion (see Sec. 2.4.1), we expect $C_v(t)$ to be logarithmically time-dependent and, in analogy with a spin-glass system [21,170], we can write [171]

$$\langle\langle\vec{u}_i(t)\cdot\vec{u}_i(0)\rangle_t\rangle_d \propto \frac{1}{\left[\frac{k_BT}{U_0} ln(\frac{t}{t_0})\right]^{\alpha}}$$

for $t \gg t_0$ where t_0 is a characteristic time in the system and $\alpha \leq 1$. Going now to Fourier space and since $C_v(t)$ varies logarithmically with t, we can use the $\pi/2$-rule [170,172]

$$|u^2(\omega)| \approx -\frac{\pi}{\omega}\frac{\partial C_v(t)}{\partial ln(t/t_0)}\Bigg|_{t=1/\omega}$$

which yields

$$|u^2(\omega)| \propto \frac{\pi\alpha}{\omega}\frac{1}{\left[\frac{k_BT}{U_0} ln(\frac{1}{\omega t_0})\right]^{(1+\alpha)}} \tag{5.18}$$

where $|u^2(\omega)|$ is the spectral density of the mean squared vortex displacement.
Quite generally, the time dependence of a physical quantity in a system submitted to a small external perturbation (linear response) can be written in terms of a generalized susceptibility χ and a generalized perturbation force F whose time dependence is assumed known [17]. This translates in our case to the relation $u_\omega = \chi(\omega)F_\omega$ between the Fourier components of the vortex displacement and the periodical perturbation force of period $2\pi/\omega$. Quite generally again, there exists a relation between the fluctuations of the physical quantities and the dissipation properties of a system experiencing a small external perturbation (fluctuation-dissipation theorem). In our particular case, the fluctuations of the vortex positions can be related to a dissipation process in the superconductor as follows (see e.g. [17])

$$|u^2(\omega)| = 2\frac{k_BT}{\omega} Im(\chi)(\omega) \tag{5.19}$$

This expression is valid in the classical limit, i.e. as long as $T \gg \hbar\omega$. Using Eqs. (5.18) and (5.19), we can deduce the expression for $Im(\chi)(\omega)$

$$Im(\chi)(\omega) \propto \frac{\pi\alpha}{2k_BT} \frac{1}{\left[\frac{k_BT}{U_0} ln(\frac{1}{\omega t_0})\right]^{(1+\alpha)}} \tag{5.20}$$

The real part of $\chi(\omega)$ can be obtained from $Im(\chi)(\omega)$ using the Kramers-Kronig relations. Since we are dealing with functions varying logarithmically with t, we can again use a $\pi/2$-rule [170, 172] and write

$$Im(\chi) = \frac{\pi}{2} \frac{\partial Re(\chi)}{(\partial ln(1/\omega t_0))}$$

yielding

$$Re(\chi)(\omega) \sim Re(\chi)(0) - C\frac{U_0}{(k_BT)^2} \frac{1}{\left[\frac{k_BT}{U_0} ln(\frac{1}{\omega t_0})\right]^{\alpha}} \tag{5.21}$$

with C a constant.
Let us come back for a while to the sheet impedance of the superconductor. If we assume a time dependence of the form $|\vec{u}(t)| = u(t) \propto e^{i\omega t}$ for the vortex displacement field, we have $v_\omega = i\omega u_\omega = i\omega\chi(\omega)F_\omega$. Since $v_\omega = E_\omega/B$ where E_ω is the electric field and $F_\omega = \phi_0 K_\omega$ where K_ω is the sheet current density, we have

$$Z(\omega) = i\omega B\phi_0\chi(\omega) \tag{5.22}$$

using $E_\omega = Z(\omega)K_\omega$. The above expression allows to write the final equations for the inverse sheet inductance and the sheet resistance in the low temperature regime [171]

$$\frac{1}{L_p(\omega)} \sim \frac{1}{L_p(0)}\left(1 + \frac{CU_0}{(k_BT)^2 Re(\chi(0))}\frac{1}{\left(\frac{k_BT}{U_0} ln(1/\omega t_0)\right)^{1/\mu}}\right) \tag{5.23}$$

$$R_s(\omega) \propto \frac{\pi}{2}\frac{B\phi_0\alpha}{2k_BTt_0}\frac{\omega t_0}{\left(\frac{k_BT}{U_0} ln(1/\omega t_0)\right)^{(1+\alpha)}} \tag{5.24}$$

where $L_p(0) = B\phi_0 Re(\chi)(0)$.

The important aspect to realize from the above expressions is that the frequency dependence of the resistance ($R_s(\omega) \propto \omega$, neglecting the logarithmic corrections) and of the inverse inductance ($L_p^{-1}(\omega) \propto \omega^0$, i.e. ω independent, neglecting again logarithmic corrections) is very close to what we observe in our experimental curves at low temperatures (see Figs. 5.7 and 5.8 on page 76 and Fig. 5.19 (left) on page 94). As mentioned in Sec. 5.1.3, such dependences are expected from the vortex-glass model as well [11]. A glassy dynamics can thus be observed although the system has not undergone a phase transition to a true vortex-glass phase. Such an observation may explain why a scaling analysis can still work in our case, at least partially, although the system does in fact not undergo a phase transition to a vortex-glass phase.

We can try here to make an analogy between a 2D vortex medium at very low temperature and a window glass at room temperature. Remember that we may compare an ordinary (3D) body composed of atoms to a 2D vortex medium due to the one-dimensional nature of vortices. There is a widespread belief that window glasses can flow at ambient temperature. This is due to the 'old-wives tale' that cathedral glasses seem to be thicker in their lower part, suggesting a gravity-induced mass flow of the glass at room temperature. As shown by E. Zanotto [173], this is not really true since the time scale required for such a window glass to flow at ambient temperature exceeds the age of Universe. In fact, the thickness variations observed in cathedral glasses like in Saint-Gatien (Tours, France) are due to the hand fabrication processes and not to a flow of the glass [174]. However what remains true is that, if the time scales at which such a flow may take place is very large, it is not infinitely large since the viscosity of the medium remains finite. This means that if such a window glass is not a solid in the thermodynamic sense like a pure crystal, it may be considered such at human time scales. The situation in a disordered 2D vortex medium is similar in the sense that if the 2D system cannot undergo a phase transition to a vortex-glass phase, it may still exhibit a very slow dynamics at low temperatures. As a consequence, the time scale at which the system is probed determines the type of behavior that will be observed, glassy or not.

We thus argue that the crossover we observe in the resistance and the inverse inductance at the frequency-dependent temperature $T_p(\omega)$ can be described as a crossover between a pinned vortex liquid (TAFF) and a collectively pinned, frozen vortex liquid (glassy dynamics). Since such a description is valid for a two-dimensional vortex system as well as for a three-dimensional vortex system, it is not surprising that, from a dynamical point of view, a 2D and a 3D vortex medium appear quite similar although they are not from a thermodynamic point of view.

5.7 Phenomenological approach for the dynamic response of the vortex system

In this section, we present a tentative description of the vortex medium mainly based on the idea that vortices form a viscoelastic medium. We start with the equation of motion for a vortex. The brownian model described in Sec. 2.5.2 provides a good description of the vortex dynamics as long as the interaction between vortices is not relevant. We have seen that the effective magnetic penetration depth is generally larger than the lattice constant in our films, meaning that the interaction between vortices will certainly play a role in the dynamic response of the system. We are thus interested in knowing the linear response of a system of interacting vortices subject to disorder and write therefore the following equation of motion for the *ith* vortex

$$\eta\frac{\partial u_{i_\alpha}(t)}{\partial t}+\nabla_\alpha U(\vec{R}_i+\vec{u}_i(t))+\sum_{j,\beta}\Phi_{(i,j)_{\alpha\beta}}u_{j_\beta}=\vec{F}_D(t) \tag{5.25}$$

where the elastic tensor $\Phi_{\alpha\beta}$ reads $\Phi_{\alpha\beta}=(c_{11}-c_{66})\nabla_\alpha\nabla_\beta+\delta_{\alpha\beta}[c_{66}\nabla^2+c_{44}\partial_z^2)]$, see Sec. 2.2.2. This equation is similar to Eq. (2.61) and we find again a viscosity term, a pinning term and the term accounting for the driving force. The main differences are the apparition of the elastic term and the disappearance of the term accounting for thermal fluctuations. We thus investigate here the elastic response (small displacements) of a pinned vortex lattice at low temperatures. We shall add by hand the effect of temperature later on.

The above equation of motion was solved by H. Beck and P. Martinoli [175] for the case of an incompressible ($c_{11}\gg c_{66}$) vortex medium where the vortices can be considered as rigid rods. The pinning barriers are assumed to be of two types, i.e. either strong (s) or weak (w) and distributed randomly with different probabilities p_s and p_w, where $p_s=1-p_w\ll p_w$. The density of weak pinning centers is thus assumed much larger than the density of strong pinning centers and the pinning wells are assumed to be parabolic for both pinning types. The effect of the disorder created by the weak random pins consists essentially in breaking the translational invariance of the vortex lattice and we adopt a picture where the vortices arrange themselves in domains separated by dislocations in the vortex system. The structure of the vortex lattice is thus essentially characterized by the typical extension l_s of such a domain in the *ab* plane, which corresponds to the typical distance between two strong pinning centers. Considering only transverse modes in the vortex system and using an effective medium approximation, the sheet impedance of the vortex medium can essentially be written [175]

$$Z_s(\omega, T, B) = R_{ff} \frac{i\omega\eta(T)}{i\omega\eta(T) + c_{66}(T, B)k_s^2} \tag{5.26}$$

where $k_s = 2\pi/l_s$. Eq. (5.26) is a simplified expression for the sheet impedance. In particular, it may appear surprising to have an expression involving only one single wave vector k_s for the response of the vortex system. This can be justified as follows. Let us consider a vortex chain for simplicity. If the vortices are not pinned, an excitation of the vortex medium with a length scale l_q will cause the vortices to respond with a typical wavelength l_q as shown in Fig. 5.25 (left). If we now pin a few vortices and assume a characteristic length scale l_s for the distance between two pinning centers, the typical wavelength for the response of the vortex system will not be l_q any more but l_s as illustrated in Fig. 5.25 (right). This argument was discussed by J. Clem a few years ago (in unpublished notes) and justifies the presence of a single dominant wavevector in the response of the vortex medium. In particular, the relevant wavevector q selected by our measuring technique corresponds to a typical wavelength of a few millimeters as described in Sec. 4.2.2. Since we expect l_s to be of the order of a few thousand Angströms, we have $q^2 \ll k_s^2$ and we can ignore the term $c_{66}q^2$ in the expression for the sheet impedance. On the basis of numerical estimates performed by H. Beck using the effective medium approximation, it turns out that we can also neglect the term accounting for the contribution from the weak pinning centers in the final expression for the sheet impedance.

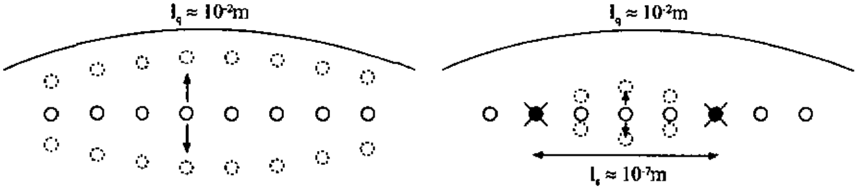

Figure 5.25: *Left: chain of unpinned vortices. Right: the pinning of two vortices forces the vortex chain to oscillate at a typical wavelength defined by l_s.*

Shear modulus

We can now turn to the problem of the shear modulus c_{66} of the vortex medium. The presence of disorder-induced dislocations in the vortex lattice is expected to affect the dynamical shear properties of the vortex medium [176, 177]. This effect can be accounted for by renormalizing the shear modulus with a frequency-dependent, complex factor $\epsilon(\omega) = \epsilon'(\omega) + \epsilon''(\omega)$

$$c_{66} \rightarrow c_{66}/\epsilon(\omega) \tag{5.27}$$

In the particular case of an unpinned 2D vortex medium undergoing a dislocation-mediated melting (bringing the shear modulus to zero), the renormalization factor accounts for the effect of bound pairs of dislocations-antidislocations and is expected to vary weakly (logarithmically) with the frequency as described by Halperin and Nelson [50]. Since we do not have an expression for $\epsilon(\omega)$ suited to our case, we will use as a first trial the renormalization factor proposed by Halperin and Nelson

$$\epsilon'(\omega) = \frac{\epsilon_c(1 + l_w(\epsilon_c - 1))}{\epsilon_c + l_w(\epsilon_c - 1)} \tag{5.28}$$

$$\epsilon''(\omega) = \frac{\pi}{2}\epsilon_c\left(\frac{\epsilon_c - 1}{\epsilon_c + l_w(\epsilon_c - 1)}\right)^2 \tag{5.29}$$

where ϵ_c is a constant close to 1 and $l_w = ln(1/\omega\tau_D)$ with $\tau_D(T) = \phi_0^2 d/(\rho_N k_B T)$.

We want now to account for the effect of temperature on the vortex system and assume that the vortex medium will gradually change its response from elastic to plastic as the temperature increases. In other words, we expect that dislocations in the vortex structure will start moving. Such a crossover between elastic and plastic response occurs in a viscoelastic medium (or very viscous liquid). The behavior of such a system can be described using an interpolation formula for the shear modulus [178]

$$c_{66} \rightarrow \frac{c_{66}}{1 + i/\omega\tau_{pl}} \tag{5.30}$$

where τ_{pl} is the characteristic time for the thermally activated plastic motion of the vortex structure. In the limit of high frequencies ($\omega\tau_{pl} \gg 1$), when we explore the system at time scales smaller than τ_{pl}, plastic deformations do not have time to develop and the interpolation formula reduces to the ordinary shear modulus for the vortex lattice where the system exhibits an elastic behavior. In the opposite limit of frequencies ($\omega\tau_{pl} \ll 1$), plastic deformations will take place and the vortex medium behaves as a viscous liquid with a viscosity proportional to $\tau_{pl}c_{66}$ [21].

Sheet impedance

Coming back to Eq. (5.26), we assume that we can account for the effect of temperature on the sheet impedance via the interpolated shear modulus. This results in the following expression for Z_s

$$Z_s = R_{ff} \frac{i\omega\tau_s}{i\omega\tau_s + \frac{1}{\epsilon(\omega)+1/i\omega\tau_{pl}}} \tag{5.31}$$

where

$$\tau_s = \frac{\eta}{c_{66}} \frac{l_s^2}{4\pi^2}, \quad \tau_{pl} = \tau_t e^{U_{pl}/k_B T}, \quad \tau_t = \frac{\eta}{c_{66}} \frac{a_0^2}{4\pi}$$

and U_{pl} is a typical energy barrier for plastic deformations.
Although this model is rather phenomenological, it reproduces quite well some aspects of the vortex dynamics. Starting at high temperatures where $(\omega\tau_{pl})^{-1} \gg |\epsilon(\omega)|$, we obtain two regimes defined by the relative values of τ_s and τ_{pl} which correspond to the flux flow (FF) and TAFF regimes. The expression for the sheet impedance reads

$$Z_s \approx R_{ff}(1 + i\omega\epsilon'\tau_s) \qquad (\tau_s \gg \tau_{pl}, FF) \tag{5.32}$$

and

$$R_s \approx R_{ff} \frac{\tau_s}{\tau_t} e^{-U_{pl}/k_B T} \qquad (\tau_s \ll \tau_{pl}, TAFF) \tag{5.33}$$

$$L_s \approx R_{ff} \epsilon' \frac{\tau_t^2}{\tau_s} e^{2U_{pl}/k_B T} \tag{5.34}$$

In the low temperature regime ($(\omega\tau_{pl})^{-1} \ll |\epsilon(\omega)|$) where the response is elastic, the system behaves as a vortex solid. A numerical estimate for τ_s using $l_s = 2 \cdot 10^{-7} m$ yields $\tau_s = 2\mu_0\lambda_{ab}^2 l_s^2/(\pi^2\xi_{ab}^2\rho_n) \approx 10^{-10}s$. We are thus in the limit of low frequencies $\omega\tau_s \ll 1$ and we can write

$$R_s \approx R_{ff}\omega\tau_s\epsilon''(\omega) \tag{5.35}$$

$$L_s \approx R_{ff}\tau_s\epsilon'(\omega) \tag{5.36}$$

The frequency dependence predicted by this model for the resistance and the inductance in the low temperature regime is very close to the observed behavior of the data at low temperatures. We refer the reader to Fig. 5.19 (left) on page 94 where we plotted the slopes of the isothermal lines for the resistance and the inductance as a function of ω for sample STO472. Indeed, if we assume that both $\epsilon'(\omega)$ and $\epsilon''(\omega)$ depend only weakly on the frequency, we have essentially that $R_s \propto \omega$ whereas L_s appears roughly independent of the frequency, which is in good agreement with what is observed at low temperatures.

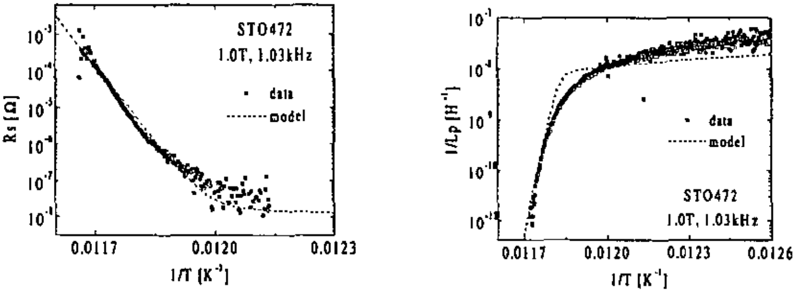

Figure 5.26: *Comparison between the measured and calculated behavior of the resistance and the inverse inductance as a function of the inverse temperature. The parameters for the model curves are* $T_{c0} = 88.5K$, $B = 1.0T$, $f = 1.03kHz$, $\xi_{ab}(0) = 15Å$, $\lambda_{ab}(0) = 2500Å$, $\rho_N = 150\mu\Omega cm$, $\gamma = 5$, $d = 1100Å$ *and* $\epsilon_c = 1.5$. *We used* $l_s = 2000Å$ *for the plot of the resistance and* $l_s = 1000Å$ *for the plot of the inverse inductance.*

If we want to go further with the model, we have to make more assumptions. The first one concerns the renormalization constant $\epsilon(\omega)$, which we do not know[2]. As a first attempt, we will use the expression of Halperin and Nelson written above. The second point concerns the dimensionality of the vortex medium. Basically, Eq. (5.31) is expected to work for a 2D vortex system (stiff vortices). We assume here that such an expression still holds for a 3D vortex system and, taking U_{pl}^{3D} for the energy barrier, we calculate the curves for the resistance and the inverse inductance as a function of the inverse temperature. The curves are shown in Fig. 5.26 together with the data for sample STO472 at $B = 1.0T$ and for $f = 1.03kHz$. We can see that, using reasonable parameters, the general trend of the data is well reproduced.

It is interesting to notice that we can easily deduce a crossover temperature (or frequency) between the low and high temperature regimes by setting $(\omega\tau_{pl})^{-1} = |\epsilon(\omega)| \approx 1$. We obtain

$$T_x(\omega) = \frac{U_{pl}(0,B)/k_B}{U_{pl}(0,B)/(k_B T_{c0}) - ln(\omega/\omega_0)} \tag{5.37}$$

where $\omega_0 = \pi\rho_N\xi_{ab}^2(0)B/(2\mu_0\lambda_{ab}^2(0)\phi_0)$. This expression is similar to the expression which was deduced in Sec. 5.3.1.

---

[2] In a recent preprint [177], D. Feinberg proposes a self-consistent expression for the renormalization constant of the shear modulus.

6 Conclusions

The richness of vortex behavior in HTS renders the study of such materials very challenging. A correct interpretation of the different regimes or phases observed is complex and requires a good knowledge of the properties of the samples under test, hence the XRD and AFM analysis performed on our layers (Chapter 3). The sheet impedance measurements, performed with an ac inductive technique (Chapter 4), allowed to investigate the dynamical response of the vortex system in our layers. We let temperature, magnetic field and sample thickness vary in order to explore a substantial region of the vortex medium phase diagram. By inducing only small driving currents in the layers, we tried not to perturbate the system too much, hoping to measure its response close to equilibrium. The measurements revealed essentially two temperature regimes, independently of the thickness of the layers.

In the high-temperature regime, we observe a thermally activated response of the vortex system which manifests itself as a linear regime in an Arrhenius plot of the resistance or of the inverse inductance (Sec. 5.3). This regime extends down roughly to the temperature $T_p(\omega)$. From these plots, we can extract the characteristic energy barrier $U(T,B)$ for vortex motion in this regime. This activation energy is temperature and magnetic field dependent but does not depend on the probing frequency ω. We observe an interesting crossover in the magnetic field dependence of the activation energy in sample STO610 (48Å thick) at a magnetic field of about $1T$. We argue that this crossover can be explained in terms of a dimensional crossover of the vortex medium and depends on the vortex density and the thickness of the sample. This interpretation is based on the fact that a long vortex is softer than a short one, the typical bending length scale $l_z^{opt} \approx a_0/\gamma$ being essentially determined by the magnetic field strength. By comparing the sample thickness with l_z^{opt}, we can determine a crossover magnetic field separating a high-field regime where the vortices are soft (3D) from a low-field regime where the vortices are stiff (2D).

At temperatures below $T_p(\omega)$, both the resistance and the inductance start to exhibit a weaker temperature dependence as the system changes its dynamical behavior. Well below T_p, the frequency dependences of the resistance and the inductance are found to be compatible with the predictions for a vortex-glass phase. By performing an analysis of our data in the framework of the vortex-glass model, we are able to scale our data and extract a glass temperature T_g and the critical exponents ν and z characterizing the phase transition

(Sec. 5.4). The values obtained for the critical exponents are in good agreement with those reported in the literature for thin films but somewhat larger than the values found in single crystals. However, when extending this scaling analysis to a much thinner film, at a vortex density where the vortex medium is 2D, as deduced from the magnetic field dependence of the activation energy, we noticed that we could also achieve a reasonable scaling of the data. Since we know from the theory that T_g is strictly zero in a 2D disordered vortex medium with dislocations, we have to wonder whether our interpretation in terms of a phase transition is correct or not. In fact the frequency dependence of the data at low temperatures is compatible with the more general assumption that the vortex medium is collectively pinned and exhibits a slow (glassy) dynamics as in the collective creep picture (Sec. 5.6). This leads us to claim that we observe a dynamical crossover from a pinned vortex liquid to a collectively pinned, (dynamically) frozen vortex liquid rather than a thermodynamic phase transition from a vortex-liquid phase to a vortex-glass phase.
At this point, the behavior of the vortex medium in our films appears very similar to the behavior of a viscous liquid probed in different viscosity regimes. Remembering that a very viscous liquid can appear as solid or as liquid depending on the time scale at which it is studied, we were tempted to apply such a description to the vortex system (Sec. 5.7). The phenomenological approach proposed is probably not totally correct, one of the more serious problems being that the renormalization constant $\epsilon(\omega)$, accounting for the effect of disorder on the shear modulus, is unknown. Nevertheless, the model reproduces with a certain accuracy the behavior of the data, leading us to think that an interpretation of the crossover observed in our data as a frequency-dependent crossover between a plastic and an elastic response of the vortex system is not totally out of place.

It may be interesting to come back to the phase transition which is expected to occur at T_g in a 3D disordered vortex system. Although we can deduce a glass temperature T_g from a scaling analysis, we do not observe in our data a striking feature (kink or jump for instance) allowing to determine the glass temperature T_g straightforwardly. Since we perform dynamic measurements, the question arises about the possibility to approach the dc limit by further decreasing the probing frequency ω. From the behavior of the Arrhenius plot of the resistance (see Fig. 5.3 for instance), we may speculate on the shape of these curves at lower frequencies and in particular wonder whether a kink in the resistivity may appear at $T = T_g$. We can estimate the temperature dependent frequency ω_x at which the vortex system crosses from a TAFF regime to a collectively pinned regime by assuming that the crossover occurs when the energy barriers in both regimes are comparable. From Eq. (2.47) and (2.48), the collective pinning energy can be written $U = k_B T ln(1/(\omega t_0))$ in the case of single-vortex creep in the collective creep picture. Using $U = U_0(B)(1 - T/T_c)$ for the activation energy in the TAFF regime, where $U_0(B)$ is obtained from the slope of the Arrhenius plot of the resistance (see Sec. 5.3.2), we obtain

$$\omega_x t_0 = e^{-\frac{U_0(B)}{k_B}\left(\frac{1}{T}-\frac{1}{T_c}\right)} \tag{6.1}$$

It it interesting to observe that the above relation can equivalently be written in terms of a crossover temperature T_x

$$T_x(\omega) = \frac{U_0(B)/k_B}{\frac{U_0}{k_B T_c} + ln(\frac{1}{\omega t_0})} \tag{6.2}$$

which has the same form as Eq. (5.5).
We can calculate the crossover frequency ω_x at the particular temperature $T = T_g$ for a given magnetic field and compare it with our measurement frequencies. Since T_g is not far from the lowest T_p observed (at $\omega/2\pi = 100Hz$), the crossover frequency should not be too far below $100Hz$. For sample STO472 at a magnetic field of $2.0T$, we get $f_x = \omega_x/(2\pi) \approx 20Hz$ using $T_g = 81.5K$ obtained from the scaling analysis and the value for t_0 extracted from a fit to Eq. (6.2) above. This estimate leads to a few comments. First, we performed measurements below $100Hz$ and should have observed something in the response of the layers if there was anything to observe, although the signal to noise ratio was becoming poor. The second comment to the above discussion is that the crossover frequency determined remains very approximate: the estimate is performed in the single vortex limit and furthermore, if we take a T_g two Kelvins below the value used above, we obtain $f_x \approx 2.3mHz$, four orders of magnitude below $20Hz$. It is therefore not clear whether we might be able or not to observe experimentally some kink in the Arrhenius plot of the resistance, if such a kink does occur. The problem presents, however, some interest and it might interesting to further think about this question.

Finally, we would like to come back to the fact that we have measured the linear response of the vortex medium and carefully avoided non-linear effects by limiting the amplitude of the drive current. It may be, however, very interesting to look at the non-linear response of the vortex system. The problem in this case is to find an inversion scheme for the data in order to extract the sheet impedance of the sample. The issue is not simple but the interest is certainly very strong since we might be able to investigate, for instance, the dependence of the activation energy on the current density induced in the layer. Since the current density determines the Lorentz force experienced by the vortices, such studies may more generally help to improve the understanding of dynamical phenomena in the vortex medium and to build a dynamical phase diagram which, besides temperature and magnetic field, would include the force acting on the vortices [2]. Let us consider a vortex medium subject to weak random pinning where plastic vortex motion does occur at low driving forces. This is what we observe in our films at high temperatures. Plastic vortex motion implies the existence of velocity gradients between vortices in different parts of the sample [179,180]. It was predicted [44] that by increasing the driving force sufficiently, the pinning force, responsible for non-uniform vortex motion at low driving forces, may be made negligible leading to a uniform ('elastic') vortex motion in the superconductor (same average velocity for all vortices). In other words, the existence of a dynamic phase transition between an incoherent fluidlike motion (plastic flow, amorphous vortex configuration) at low driving forces and a moving crystal (elastic flow, the vortex system having recovered a crystalline order) at higher driving forces is claimed. Our inductive technique exploited at different driving currents may be a very powerful tool for the investigation of such effects.

Acknowledgements

It a great pleasure to thank Prof. P. Martinoli for giving me the opportunity to work in the field of superconductivity. I could appreciate his permanent enthusiasm and openness for discussion during the time spent in his group. His knowledge and advice were of great help during this work.
I would like to warmly thank Dr. Chris Leemann for passing on his experience on cryogeny and measuring techniques and for his critical reading of the manuscript and support, Dr. Daniel Ariosa for transmitting with great humor and enthusiasm his passion for physics and, particularly, his deep knowledge on XRD techniques and for his help on the laser ablation technique, Dr. Sergey Korshunov for the enlightening discussions we had on the theoretical aspects of the vortex dynamics, Dr. L. Baselgia Stahel, for the work she did on the subject as a postdoc during two years, Dr. A. Daridon for his help on the AFM analysis and Professors H. Beck, W. Benoît and J.-M. Triscone for having accepted to be part of the board of examiners for this PhD thesis.
My thanks go as well to B. Schmied and S. Blaser for the work accomplished during their diploma stage. Let me also warmly thank J. Perret, J. Affolter, P. Scheuzger, Y. Jaccard, A. Eichenberger and H. Pastoriza, all current or previous members of the group who all contributed to some extent to this work and to the very nice moments spent together. Special thanks to Dr. R. Meyer and Dr. Ph. Flückiger for their 'learned' and wise advice during the work and the writing.
The help from the technical staff of the electronics and mechanics workshops was greatly appreciated and I thank them all for their realizations and invaluable advice.

Finally, I would like to thank my parents and Jeanne-Marie for their unfailing support and patience during these years devoted to the vortices.

This work was supported by the Swiss National Science Foundation.

Bibliography

[1] J. G. Bednorz and K. A. Müller, Z. Phys. B **64**, 189 (1986).

[2] G. W. Crabtree and D. R. Nelson, Physics Today **Apr.**, 38 (1997).

[3] T. M. Rice, Physica C **282–287**, *xix* (1997).

[4] N. M. Plakida, *High-Temperature Superconductivity*, Springer, Berlin, 1995.

[5] J. R. Waldram, *Superconductivity of Metals and Cuprates*, IOP, Bristol, 1996.

[6] B. Batlogg, Physica C **282–287**, *xxiv* (1997).

[7] M. Tinkham, *Introduction to Superconductivity*, Mc Graw-Hill, New York, 2nd edition, 1996.

[8] E. Zeldov et al., Nature **375**, 373 (1995).

[9] A. Schilling et al., Nature **382**, 791 (1996).

[10] Y. B. Kim and M. J. Stephen, Flux flow and irreversible effects, in *Superconductivity*, edited by R. D. Parks, volume **2**, page 1107, Dekker, New York, 1969.

[11] D. S. Fisher, M. P. A. Fisher, and D. A. Huse, Phys. Rev. B **43**, 130 (1991).

[12] C. J. Gorter and H. Casimir, Physik. Z. **35**, 963 (1934).

[13] F. London and H. London, Proc. Roy. Soc. **149**, 71 (1935).

[14] W. Meissner and R. Ochsenfeld, Naturwissenschaften **21**, 787 (1933).

[15] J. Bardeen, L. N. Cooper, and J. R. Schrieffer, Phys. Rev. **108**, 1175 (1957).

[16] V. L. Ginzburg and L. D. Landau, Zh. Eksp. Teor. Fiz. **20**, 1064 (1950).

[17] L. Landau and E. Lifchitz, *Physique statistique*, MIR, Moscou, 4ème edition, 1994.

[18] A. A. Abrikosov, Soviet Phys. JETP **5**, 1174 (1957).

[19] L. P. Gor'kov, Soviet Phys. JETP **9**, 1364 (1959).

[20] C. J. Lobb, Phys. Rev. B **36**, 3930 (1987).

[21] G. Blatter, M. V. Feigel'man, V. B. Geshkenbein, A. I. Larkin, and V. M. Vinokur, Rev. Mod. Phys. **66**, 1125 (1994).

[22] W. E. Lawrence and S. Doniach, Theory of Layer Structure Superconductors, in *Proceedings of the 12th International Conference on Low Temperature Physics*, edited by E. Kanda, page 361, Keigaku, Tokyo, 1971.

[23] L. N. Bulaevskii, Soviet Phys. JETP **37**, 1133 (1973).

[24] E. H. Brandt, Rep. Prog. Phys. **58**, 1465 (1995).

[25] J. R. Clem, Anisotropic Superconductors: Fundamentals of Vortices in Layered Superconductors, in *Proceedings of the NATO Advanced Study Institute on Vortices in Superfluids*, edited by N. Bontemps, Y. Bruynseraede, G. Deutscher, and A. Kapitulnik, page 25, Cargèse, Corsica, France, 1993.

[26] G. Blatter, V. B. Geshkenbein, and A. I. Larkin, Phys. Rev. Lett. **68**, 875 (1992).

[27] A. M. Campbell and J. E. Evetts, Adv. Phys. **21**, 199 (1972).

[28] C. P. Poole Jr., H. A. Farach, and R. J. Creswick, *Superconductivity*, Academic Press, 1995.

[29] B. D. Josephson, Phys. Lett. **16**, 242 (1965).

[30] M. Tinkham, Phys. Rev. Lett. **13**, 804 (1964).

[31] L. Glazman and A. Koshelev, Phys. Rev. B **43**, 2835 (1991).

[32] J. Pearl, *PhD Thesis*, Polytechnic Institute of Brooklyn, New-York, unpublished, 1965.

[33] S. N. Artemenko and A. N. Kruglov, Phys. Lett. A **143**, 485 (1990).

[34] M. V. Feigel'man, V. B. Geshkenbein, and A. I. Larkin, Physica C **167**, 177 (1990).

[35] J. R. Clem, Phys. Rev. B **43**, 7837 (1991).

[36] V. M. Vinokur, P. H. Kes, and A. E. Koshelev, Physica C **168**, 29 (1990).

[37] D. R. Nelson and H. S. Seung, Phys. Rev. B **39**, 9153 (1989).

[38] A. Houghton, R. A. Pelcovits, and A. Sudbø, Phys. Rev. B **40**, 6763 (1989).

[39] E. H. Brandt, Phys. Rev. Lett. **63**, 1106 (1989).

[40] D. R. Nelson, Phys. Rev. Lett. **60**, 1973 (1988).

[41] D. E. Farrell, Transformations of the Vortex Solid, in *Physical Properties of High-Temperature Superconductors IV*, edited by D. M. Ginsberg, page 7, World Scientific, Singapore, 1994.

[42] H. Nordborg and G. Blatter, cond-mat/9803041, march 1998 (preprint).

[43] S. Ryu, S. Doniach, G. Deutscher, and A. Kapitulnik, Phys. Rev. Lett. **68**, 710 (1992).

[44] A. E. Koshelev and V. M. Vinokur, Phys. Rev. Lett. **73**, 3580 (1994).

[45] A. E. Koshelev, Phys. Rev. B **56**, 11201 (1997).

[46] F. Lindemann, Phys. Z. **10**, 69 (1910).

[47] G. Blatter, V. B. Geshkenbein, A. I. Larkin, and H. Nordborg, Phys. Rev. B **54**, 72 (1996).

[48] G. Blatter and B. I. Ivlev, Phys. Rev. B **50**, 10272 (1994).

[49] J. M. Kosterlitz and D. J. Thouless, J. Phys. C **6**, 1181 (1973).

[50] B. I. Halperin and D. R. Nelson, J. Low Temp. Phys. **36**, 599 (1979).

[51] B. A. Hubermann and S. Doniach, Phys. Rev. Lett. **43**, 950 (1979).

[52] P. G. de Gennes, *Superconductivity of Metals and Alloys*, Benjamin, New York, 1966.

[53] P. H. Kes, Flux Pinning and the Summation of Pinning Forces, in *Concise Encyclopedia of Magnetic and Superconducting Materials*, edited by J. Evetts, page 163, Pergamon Press, 1992.

[54] H. R. A. Douwes, *PhD Thesis*, Rijksuniversiteit Leiden, The Netherlands, 1994.

[55] L. N. Bulaevski, Soviet Phys. JETP **37**, 1133 (1991).

[56] E. V. Thuneberg, J. Kurkijarvi, and D. Rainer, Phys. Rev. B **29**, 3913 (1984).

[57] P. H. Kes, Vortex pining and creep experiments, in *Phenomenology and Applications of High-Temperature Superconductors*, edited by K. Bedell, page 390, Addison-Wesley, New York, 1992.

[58] C. J. van der Beek and P. H. Kes, Phys. Rev. B **43**, 13032 (1991).

[59] A. I. Larkin and Y. N. Ovchinnikov, J. Low Temp. Phys. **34**, 409 (1979).

[60] Y. Zhu and M. Suenaga, The Twin-Boundary Structure in $YBa_2Cu_3O_7$ Superconductors, in *Interfaces in High-T_c Superconducting Systems*, edited by S. L. Shinde and D. A. Rudman, page 140, Springer, Berlin, 1994.

[61] V. Geshkenbein, A. Larkin, M. Feigel'man, and V. Vinokur, Physica C **162–164**, 239 (1989).

[62] P. W. Anderson and Y. B. Kim, Rev. Mod. Phys. **30**, 39 (1964).

[63] S. E. Korshunov, Phys. Rev. B **48**, 3969 (1993).

[64] D. Carpentier and P. L. Doussal, Phys. Rev. B **55**, 12128 (1997).

[65] V. M. Vinokur, M. V. Feigel'man, V. B. Geshkenbein, and A. I. Larkin, Phys. Rev. Lett. **65**, 259 (1990).

[66] V. M. Vinokur, V. B. Geshkenbein, A. I. Larkin, and M. V. Feigel'man, Soviet Phys. JETP **73**, 610 (1991).

[67] J. Bardeen and M. J. Stephen, Phys. Rev. **140**, 1197 (1965).

[68] A. T. Dorsey, Phys. Rev. B **43**, 7575 (1991).

[69] P. H. Kes, J. Aarts, J. van den Berg, C. J. van der Beek, and J. A. Mydosh, Supercond. Sci. Technol. **1**, 242 (1989).

[70] V. B. Geshkenbein, V. M. Vinokur, and R. Fehrenbacher, Phys. Rev. B **43**, 3748 (1991).

[71] L. Landau and E. Lifchitz, *Electrodynamique des milieux continus*, MIR, Moscou, 2ème edition, 1990.

[72] J. I. Gittleman and B. Rosenblum, Phys. Rev. Lett. **16**, 734 (1966).

[73] J. R. Clem and M. W. Coffey, Phys. Rev. B **46**, 14662 (1992).

[74] P. Martinoli et al., Physica B **165–166**, 1163 (1990).

[75] M. W. Coffey and J. R. Clem, Phys. Rev. Lett. **67**, 386 (1991).

[76] P. Flückiger, *PhD Thesis*, Université de Neuchâtel, unpublished, 1992.

[77] M. K. Wu et al., Phys. Rev. Lett. **58**, 908 (1987).

[78] J. Rossat-Mignod et al., Physica B **186**, 1 (1993).

[79] B. Bucher, J. Karpinski, E. Kaldis, and P. Wachter, Journal of the Less-Common Metals **164**, 20 (1990).

[80] T. Datta, Oxide superconductors: Physical properties, in *Concise Encyclopedia of Magnetic and Superconducting Materials*, edited by J. Evetts, page 408, Pergamon Press, 1992.

[81] J. M. Tarascon, W. R. McKinnon, L. H. Greene, and G. W. Hull, Phys. Rev. B **36**, 226 (1987).

[82] Z. Zou, K. Oka, T. Ito, and Y. Nishihara, Jpn. J. Appl. Phys. Lett. **36**, 18 (1997).

[83] T. R. Lemberger, Films of high-temperature oxide superconductors, in *Physical Properties of High-Temperature Superconductors III*, edited by D. M. Ginsberg, page 471, World Scientific, Singapore, 1992.

[84] R. J. Cava et al., Physica C **165**, 419 (1990).

[85] D. R. Lide, editor, *Handbook of Chemistry and Physics*, CRC Press, 74th edition, 1993.

[86] T. Terashima et al., Phys. Rev. Lett. **67**, 1362 (1991).

[87] A. T. Fiory, A. F. Hebard, P. M. Mankievich, and R. E. Howard, Appl. Phys. Lett. **52**, 2165 (1988).

[88] D. B. Chrisey and G. K. Hubler, *Pulsed Laser Deposition of Thin Films*, Wiley and Sons, 1994.

[89] C. Gerber, D. Anselmetti, J. G. Berdnorz, J. Mannhart, and D. G. Schlom, Nature **350**, 279 (1991).

[90] M. Hawley, I. D. Raistrick, J. G. Beery, and R. J. Houlton, Science **251**, 1587 (1991).

[91] S. Proyer, E. Stangl, M. Borz, B. Hellebrand, and D. Bauerle, Physica C **257**, 1 (1996).

[92] J. Mannhart, J. G. Bednorz, A. Catana, G. Gerber, and D. G. Schlom. High-T_c thin films. growth modes - structure - applications, in *Proceedings of the NATO Advanced Study Institute on Materials and Crystallographic Aspect of HT_c-Superconductors*, edited by E. Kaldis, page 453, Kluwer, The Netherlands, 1994.

[93] H. J. Scheel, M. Berowski, and B. Chabot, Physica C **185**, 2095 (1991).

[94] J. P. Contour, J. Phys. III **11**, 2159 (1994).

[95] J. P. Carini et al., Phys. Rev. B **37**, 9726 (1988).

[96] P. Lerch et al., Physica C **242**, 30 (1995).

[97] U. Welp et al., Phys. Rev. Lett. **69**, 2130 (1992).

[98] M. G. Norton and C. B. Carter, Observation on the growth of $Y_1Ba_2Cu_3O_7$ thin films by transmission electron microscopy, in *Interfaces in High-T_c Superconducting Systems*, edited by S. L. Shinde and D. A. Rudman, page 1, Springer, Berlin, 1994.

[99] C. C. Shen, G. Lehane, J. P. Zheng, and H. S. Kwok, Appl. Phys. Lett. **64**, 3175 (1994).

[100] E. Olsson and S. L. Shinde, Interfacial Interaction Between High-T_c $YBa_2Cu_3O_7$ Thin Films and Substrates, in *Interfaces in High-T_c Superconducting Systems*, edited by S. L. Shinde and D. A. Rudman, page 116, Springer, Berlin, 1994.

[101] B. Brunner, *PhD thesis*, University of Regensburg, 1995.

[102] N. Savvides and A. Katsaros, Physica C **226**, 23 (1994).

[103] R. H. Hammond and R. Bormann, Physica C **162–164**, 703 (1989).

[104] R. Feenstra, T. B. Lindemer, J. D. Budai, and M. D. Galloway, J. Appl. Phys. **69**, 6569 (1991).

[105] J. P. Locquet and E. J. Williams, Acta Phys. Polonica A **92**, 69 (1997).

[106] S. J. Rothman, J. L. Routbort, U. Welp, and J. E. Baker, Phys. Rev. B **44**, 2326 (1991).

[107] H. P. Klug and L. E. Alexander, *X-Ray Diffraction Procedures*, Wiley, New York, 2nd edition, 1974.

[108] D. Ariosa, private communication, 1998.

[109] V. Holy, J. Kubena, E. A. K. Lischka, A. Pesek, and E. Koppensteiner, J. Appl. Phys. **74**, 1736 (1993).

[110] A. Ganzi, *PhD thesis*, Ecole Polytechnique Fédérale de Lausanne, 1993.

[111] D. G. Schlom et al., Z. Phys. B **86**, 163 (1992).

[112] J. F. Jorgensen, *The Scanning Probe Image Processor User's Guide*, Danish Institute of Fundamental Metrology (unpublished), 1996.

[113] K. Fukushima, Int. J. Mod. Phys. B **9**, 3625 (1995).

[114] L. J. van der Pauw, Philips Res. Repts **13**, 1 (1958).

[115] C. Kwon et al., Appl. Phys. Lett. **62**, 1289 (1993).

[116] J.-M. Triscone and Ø. Fisher, Rep. Prog. Phys. **60**, 1673 (1997).

[117] B. Batlogg et al., Physica C **235–240**, 130 (1994).

[118] A. T. Fiory, A. F. Hebard, P. M. Mankievich, and R. E. Howard, Phys. Rev. Lett. **61**, 1419 (1988).

[119] P. Luginbühl, *Travail de diplôme*, Université de Neuchâtel, unpublished, 1992.

[120] M. Calame, *Travail de diplôme*, Université de Neuchâtel, unpublished, 1993.

[121] B. Schmied, *Travail de diplôme*, Université de Neuchâtel, unpublished, 1993.

[122] S. Blaser. *Travail de diplôme*, Université de Neuchâtel, unpublished, 1997.

[123] B. Jeanneret, J. L. Gavilano, G. A. Racine, C. Leemann, and P. Martinoli, Appl. Phys. Lett. **55**, 2336 (1989).

[124] A. T. Fiory and A. F. Hebard, AIP Conf. Proc. **58**, 293 (1980).

[125] B. D. Josephson, Phys. Rev. **152**, 211 (1966).

[126] E. H. Brandt, Z. Phys. B **80**, 167 (1990).

[127] C. J. van der Beek, V. B. Geshkenbein, and V. M. Vinokur, Phys. Rev. B **48**, 3393 (1993).

[128] Y. Ando, H. Kubota, Y. Sato, and I. Terasaki, Phys. Rev. B **50**, 9680 (1994).

[129] J. Kötzler, M. Kaufmann, G. Nakielski, and R. Behr, Phys. Rev. Lett. **72**, 2081 (1994).

[130] C. Ren et al., Physica C **279**, 258 (1997).

[131] R. Besson, *Aide-mémoire d'électronique*, Dunod, Paris, 1992.

[132] S. J. Turneaure, E. R. Ulm, and T. R. Lemberger, J. Appl. Phys. **79**, 4221 (1996).

[133] J. Perret, *PhD Thesis (to appear soon)*, Université de Neuchâtel.

[134] A. F. Hebard and A. T. Fiory, Recent experimental results on vortex processing in thin-film superconductors, in *Ordering in two dimensions*, edited by S. K. Sinha, page 181, Elsevier North-Holland, 1980.

[135] A. Schmid, Phys. Kond. Materie **5**, 302 (1966).

[136] H. W. Ott, *Noise Reduction Techniques in Electronic Systems*, Wiley, New-York, 1976.

[137] J. Y. Lee, K. M. Paget, T. R. Lemberger, S. R. Foltyn, and X. Wu, Phys. Rev. B **50**, 3337 (1994).

[138] D. L. Cox and B. M. Maple, Physics Today **Feb.**, 32 (1995).

[139] W. N. Hardy, D. A. Bonn, D. C. Morgan, R. Liang, and K. Zhang, Phys. Rev. Lett. **70**, 3999 (1993).

[140] J. E. Sonier et al., Phys. Rev. Lett. **72**, 744 (1994).

[141] L. A. de Vaulchier et al., Europhys. Lett. **33**, 153 (1996).

[142] S. Hensen, G. Mueller, C. T. Rieck, and K. Scharnberg, Phys. Rev. B **56**, 6237 (1997).

[143] J. Annett, N. Goldenfeld, and S. R. Renn, Phys. Rev. B **43**, 2778 (1991).

[144] Z. Ma et al., Phys. Rev. Lett. **71**, 781 (1993).

[145] P. J. Hirschfeld and N. Goldenfeld, Phys. Rev. B **48**, 4219 (1993).

[146] D. Stauffer and A. Aharony, *Introduction to Percolation Theory*, Taylor and Francis, 2nd edition, 1991.

[147] Y. J. Uemura et al., Physica C **162–164**, 857 (1989).

[148] M. Willemin, *Travail de diplôme*, Université de Neuchâtel, unpublished, 1995.

[149] J. M. Repaci et al., Phys. Rev. B **54**, 9674 (1996).

[150] M. Calame, C. Leemann, L. Baselgia Stahel, and P. Martinoli, Effect of pinning and thermal fluctuations on the superconducting phase transition of thin films, in *Superconducting and Related Oxides: Physics and Nanoengineering III (to be published)*, edited by D. Pavuna and I. Bozovic, SPIE Proc. 3481 (SPIE, Bellingham,1998).

[151] M. Calame, L. Baselgia Stahel, C. Leemann, and P. Martinoli, Czech. J. Phys. **46**, 1619 (1996).

[152] O. Brunner, L. Antognazza, J.-M. Triscone, L. Miéville, and Ø. Fischer, Phys. Rev. Lett. **67**, 1354 (1991).

[153] X. G. Qiu, B. Wuyts, M. Maenhoudt, V. V. Moshalkov, and Y. Bruynseraede, Phys. Rev. B **52**, 559 (1995).

[154] J. J. Sun et al., Physica C **270**, 343 (1996).

[155] M. Ye et al., Physica C **258**, 95 (1996).

[156] R. H. Koch et al., Phys. Rev. Lett. **63**, 1511 (1989).

[157] N.-C. Yeh, W. Jiang, D. S. Reed, U. Kriplani, and F. Holtzberg, Phys. Rev. B **47**, 6146 (1993).

[158] L. Baselgia Stahel et al., Physica C **235–240**, 2665 (1994).

[159] M. Calame, L. Baselgia Stahel, D. Ariosa, C. Leemann, and P. Martinoli, Linear dynamic response of vortices in the mixed state of $YBa_2Cu_3O_7$ thin films, in *Proceedings of the first International Summer School on High Temperature Superconductivity*, edited by J. Bankuti, I. Vajda, and A. Szalay, page 24, Eger, Hungary, 1995.

[160] J. M. Roberts, B. Brown, B. A. Hermann, and J. Tate, Phys. Rev. B **49**, 6890 (1994).

[161] D. S. Reed et al., Phys. Rev. B 49, 4334 (1994).

[162] P. L. Gammel, L. F. Schneemeyer, and D. J. Bishop, Phys. Rev. Lett. **66**, 953 (1991).

[163] H. Safar, P. L. Gammel, D. J. Bishop, D. B. Mitzi, and A. Kapitulnik, Phys. Rev. Lett. **08**, 2672 (1992).

[164] C. Dekker, P. J. M. Wöltgens, R. H. Koch, B. W. Hussey, and A. Gupta, Phys. Rev. Lett. **09**. 2717 (1992).

[165] P. J. M. Wöltgens, C. Dekker, R. H. Koch, B. W. Hussey, and A. Gupta, Phys. Rev. B **52**, 4536 (1995).

[166] J. Deak, M. McElfresh, R. Muenchausen, S. Foltyn, and R. Dye, Phys. Rev. B **48**, 1337 (1993).

[167] P. J. M. Wöltgens. *PhD Thesis.* Universiteit Utrecht, The Netherlands, 1993.

[168] J. Kötzler et al., Phys. Rev. B **50**, 3384 (1994).

[169] G. Nakielski et al., Phys. Rev. B **5**, 1 (1997).

[170] D. S. Fisher and D. A. Huse, Phys. Rev. B **38**, 386 (1988).

[171] P. Martinoli, unpublished, 1998.

[172] E. Pytte and Y. Imry, Phys. Rev. B **35**, 1465 (1987).

[173] E. D. Zanotto, Am. J. Phys. **66**, 392 (1998).

[174] Perspectives scientifiques, Pour la Science **252**, 23 (1998).

[175] H. Beck and P. Martinoli, unpublished, 1985.

[176] M. C. Marchetti and D. R. Nelson, Phys. Rev. B **41**, 1910 (1990).

[177] D. Feinberg, cond-mat/9805080, may 1998 (preprint).

[178] L. Landau and E. Lifchitz, *Théorie de l'élasticité*, MIR, Moscou, 2ème edition, 1990.

[179] F. Nori, Science **271**, 1373 (1996).

[180] M. J. Higgins and S. Battacharya, Physica C **257**, 232 (1996).

Appendix A Experimental details

This Appendix gathers some details about the cryogenic system used. A general view of the cryostat is shown in Fig. A.1.

A.1 Inner vacuum tube and Hall probe

The inner thin-wall tube (diameter $22mm$, length $101mm$) is ended with a copper block where the impedance is soldered. The impedance is a stainless-steel tube of external diameter $1mm$ and internal diameter $0.6mm$. A heater ($0.2mm\ NM-36$ copper wire, Lakeshore) is winded at the top of the copper block and permanently anchored with Stycast 2850FT. The temperature can be monitored by means of a diode sensor (DT-470-SD-12A, Lakeshore, serial #D10110) fixed at the bottom of the copper block, also with Stycast 2850FT.

The transverse Hall probe (LHP-NP #268, Labertec Scientific) is mounted on a non-magnetic (Arcap AP1, composed mainly by 25 % Ni, 63 % Cu and 10 % Zn) support. The center of the probe is $18mm$ away from the geometrical center of the superconducting coil. The control current we use is $100mA$ at all temperatures. The sensitivity given by the manufacturer is $24.1mV/T$ at $300K$. Table A.1 summarizes the observed sensitivities for a control current of $100.0mA$. The magnetic field value is obtained from the current forced into the coil using the field to current ratio given by the manufacturer (see below).

B [T]	0.01	0.10	1.00	2.50
Sensitivity [mV/T]	21.1	23.2	23.7	23.8

Table A.1: *Observed sensitivity of the Hall probe.*

A.2 Superconducting coil

Our coil was built by Oxford Instruments. Its inductance is about $0.55H$ and the maximum magnetic field is $3T$ for a current of approximately $68A$. The precise field to current ratio is $0.04417T/A$. Fig. A.2 (left) shows the equivalent circuit for the magnet.

The superconducting switch has a typical resistance of 100Ω. A current of about $40mA$ is used to open the switch. An Allen-Bradley sensor (nominally 270Ω at room temperature) is mounted close to the coil allowing to monitor its temperature.

A plot of the magnetic field as a function of lateral displacement (see Fig. A.2, right) is provided. The Hall probe is not mounted at the center of the coil and the magnetic field value at the Hall probe location is estimated to be decreased by 0.8% at $3T$.

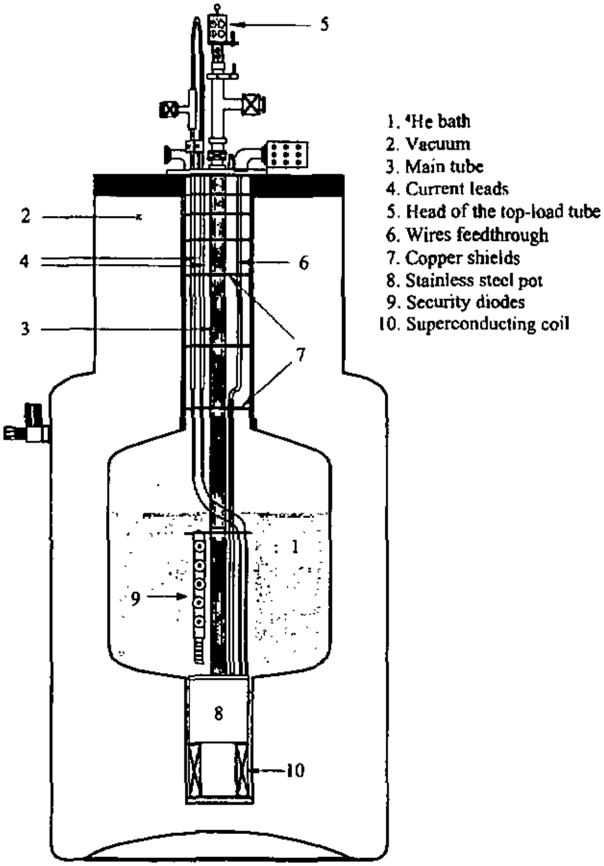

Figure A.1: *General view of the cryostat.*

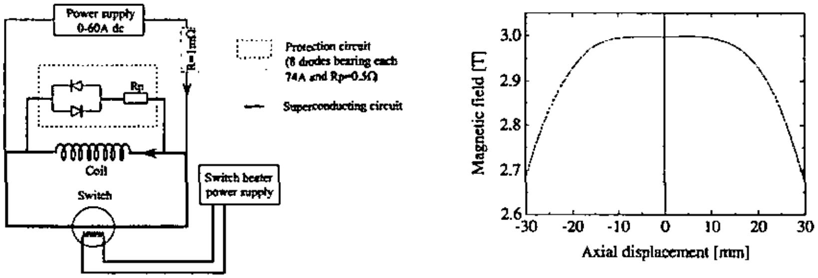

Figure A.2: *Left: Superconducting coil circuit. Right: Axial plot of the magnetic field for* $B = 3.0T$

A.2.1 Calibration curve for the carbon-glass sensor

The carbon-glass (CGR) temperature sensor (CCR-1-2000, Lakeshore, serial #15267) mounted in the sample holder has been calibrated in september 1995 from a reference sensor (CCR #15235) calibrated by the manufacturer. The resistance measurement was done from $4.2K$ up to $120K$ and an interpolation table was calculated. In order to insert a calibration curve in the temperature controller, the temperature interval was divided into four regions (I: $4.2K$ to $10K$, step $0.5K$, 13 points; II: $11K$ to $40K$ step $1.0K$, 30 points; III: $41.5K$ to $100K$ step $1.5K$, 40 points; IV: $102K$ to $120K$, step $2.0K$, 10 points).

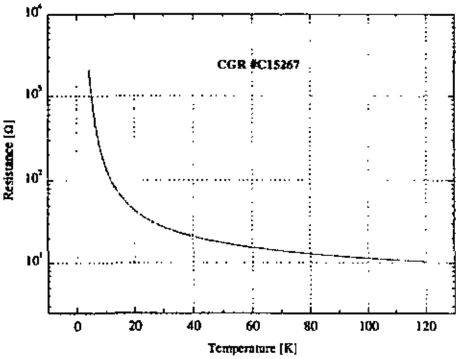

Figure A.3: *Resistance versus temperature curve for the temperature sensor CGR #15267.*

The 93 pairs of points obtained were inserted in the temperature controller in the form $(log(R), T)$ where R is here the resistance of the CGR in ohms and T the temperature in kelvins. The interpolated curve is shown in Fig. A.3 and Table A.2 gives the calibration curve used for the temperature controller (Lakeshore DRC-91CA). The first line to be entered is given at the top of the table. The points should be entered with the same numerical format as in the table.

Table A.2: *Calibration curve for sensor GGR #15267. Resistance R is in ohms and temperature T in kelvins.*

First line: 06,L0CGR1200C15267 ,N,95,									
log(R)	T	log(R)	T	log(R)	T	log(R)	T	log(R)	T
0.00000	499.9	1.08671	088.0	1.19119	059.5	1.38574	034.0	1.82378	015.0
1.01675	120.0	1.09084	086.5	1.19908	058.0	1.39748	033.0	1.87361	014.0
1.02038	118.0	1.09499	085.0	1.20697	056.5	1.41021	032.0	1.93021	013.0
1.02401	116.0	1.09951	083.5	1.21492	055.0	1.42295	031.0	1.99483	012.0
1.02764	114.0	1.10404	082.0	1.22396	053.5	1.43741	030.0	2.06970	011.0
1.03127	112.0	1.10856	080.5	1.23299	052.0	1.45219	029.0	2.15747	010.0
1.03491	110.0	1.11340	079.0	1.24203	050.5	1.46826	028.0	2.20816	009.5
1.03921	108.0	1.11838	077.5	1.25179	049.0	1.4850¡4	027.0	2.26149	009.0
1.04351	106.0	1.12336	076.0	1.26214	047.5	1.50269	026.0	2.32356	008.5
1.04782	104.0	1.12852	074.5	1.27298	046.0	1.52265	025.0	2.38853	008.0
1.05212	102.0	1.13403	073.0	1.28428	044.5	1.54329	024.0	2.46632	007.5
1.05642	100.0	1.13954	071.5	1.29640	043.0	1.56481	023.0	2.54659	007.0
1.06000	098.5	1.14505	070.0	1.30909	041.5	1.58855	022.0	2.64427	006.5
1.06359	097.0	1.15121	068.5	1.32267	040.0	1.61351	021.0	2.75399	006.0
1.06717	095.5	1.15737	067.0	1.33178	039.0	1.64092	020.0	2.87746	005.5
1.07092	094.0	1.16353	065.5	1.34194	038.0	1.67090	019.0	3.02550	005.0
1.07477	092.5	1.17020	064.0	1.35209	037.0	1.70344	018.0	3.20588	004.5
1.07862	091.0	1.17707	062.5	1.36235	036.0	1.73948	017.0	3.33681	004.2
1.08257	089.5	1.18394	061.0	1.37405	035.0	1.7794 5	016.0	6.55360	000.0

Appendix B Activation energies

In the table below, we gather the values for the activation energies extracted in the high temperature (TAFF) regime for the four films at different magnetic fields. The values are given in Kelvins.

Sample	B [T]	U(0,B) [K]	Sample	B [T]	U(0,B) [K]
STO 472 (1100Å)	0.25	65800	STO 269 (400Å)		
	0.50	48100			
	1.00	36600		1.00	19010
				1.50	15660
	2.00	28750		2.00	13960
	2.65	24900		2.50	11960
STO 610 (48Å)	0.01	7576.5	STO 607 (24Å)	0.01	1048.2
	0.03	6504.9		0.03	894.83
	0.10	5883.2		0.10	726.01
	0.30	5073.8		0.30	547.44
				0.70	442.74
	1.00	4135.2		1.00	391.46
	1.50	3442.6		1.50	326.71
	2.00	2905.0		2.00	296.07
	2.50	2413.3			

Table B.1: *Activation energies as a function of the magnetic field for the four samples investigated. The uncertainty on U(0,B) is about 5%.*